



저작자표시-비영리-변경금지 2.0 대한민국

이용자는 아래의 조건을 따르는 경우에 한하여 자유롭게

- 이 저작물을 복제, 배포, 전송, 전시, 공연 및 방송할 수 있습니다.

다음과 같은 조건을 따라야 합니다:



저작자표시. 귀하는 원저작자를 표시하여야 합니다.



비영리. 귀하는 이 저작물을 영리 목적으로 이용할 수 없습니다.



변경금지. 귀하는 이 저작물을 개작, 변형 또는 가공할 수 없습니다.

- 귀하는, 이 저작물의 재이용이나 배포의 경우, 이 저작물에 적용된 이용허락조건을 명확하게 나타내어야 합니다.
- 저작권자로부터 별도의 허가를 받으면 이러한 조건들은 적용되지 않습니다.

저작권법에 따른 이용자의 권리는 위의 내용에 의하여 영향을 받지 않습니다.

이것은 [이용허락규약\(Legal Code\)](#)을 이해하기 쉽게 요약한 것입니다.

[Disclaimer](#)

공학박사 학위논문

**Photophysical properties and  
dynamics of donor-acceptor  
based BODIPY photosensitizers:  
Molecular design for efficient  
triplet photosensitizers**

도너 - 억셉터 기반 보디피 광감응제의 광물리  
적 특성 및 동역학 연구: 고효율 삼중항 광감  
응제를 위한 분자 디자인

2021년 8월

서울대학교 대학원

재료공학부

이 재 문



## Abstract

# Photophysical properties and dynamics of donor-acceptor based BODIPY photosensitizers: Molecular design for efficient triplet photosensitizers

Jaemoon Lee

Department of Material Science and Engineering

The Graduate School

Seoul National University

Organic donor-acceptor based photosensitizers have received a lot of attention in various fields such as dye sensitizers solar cells (DSSC), OLED using thermally activated delayed fluorescence (TADF), photodynamic therapy (PDT), and triplet-triplet annihilation upconversion (TTA-UC). The electron donor and the electron acceptor of donor-acceptor photosensitizers pushes and pulls the electrons, respectively, during photoexcitation, resulting in charge separation state. This charge separation states, due to its high dipole moment, are

sensitively affected by the surrounding environment, which can cause the drastic change of the fluorescence properties. The donor-acceptor photosensitizers can thus be used for a variety of sensors such as a temperature sensor and a polarity sensor. In addition, the one-directional charge transfer property from donor to acceptor enables application as a dye, a component of dye-sensitized solar cells (DSSC). The dye in DSSC absorbs light and transfers electrons from the donor to the acceptor, and this one-directional energy allows electrons to move from the dye to  $\text{TiO}_2$ . Moreover, the donor and acceptor moieties are commonly connected with single bond, which allows various rotational change between the donor and acceptor. Because the degree of conformation between donor and acceptor varies depending on the surrounding pressure, donor-acceptor photosensitizers can be used as a pressure sensor, applicable to the fingerprint sensors. In addition, it can be implemented to the thermally activated delayed fluorescence (TADF) in the research field of OLED. The orthogonal coordination of donor and acceptor increases the charge separation between donor and acceptor, which reduces in the energy gap between the singlet and triplet excited states. The completely separated charge of donor-acceptor induces the degeneration of the both energy states, resulting in the intersystemcrossing (ISC) between singlet and triplet states. Thus, D-A photosensitizers may populate electrons in the triplet state through

ISC during the photoexcitation process. Since the electrons of the triplet state have the potential to convert triplet oxygen into singlet oxygen, D-A photosensitizers can be applied to photodynamic therapy (PDT) using singlet oxygen. Although D-A photosensitizers have potential in various fields, their photophysical kinetics are still not fully revealed. Recently, a number of researches were performed that applying the D-A photosensitizers as a triplet sensitizer, and D-A-based triplet sensitizers that even exceed the characteristics of conventional triplet sensitizers have been continuously reported.

In this study, we designed and developed D-A photosensitizers based on boron dipyrromethane (BODIPY), and studied the correlation between the molecular structure and photophysical properties such as fluorescence and triplet characteristics. First, we examined the applicability of D-A photosensitizers to the field of fluorescent materials, especially mechanofluorochromism (MFC), where the fluorescent color changes according to pressure, and the mechanism for the MFC systematically investigated based on the theory of the twisted intramolecular charge transfer (TICT) and the aggregation induced emission enhancement (AIEE). Second, we developed BODIPY-based D-A photosensitizers with different accepting power by controlling the number of chlorines, studied the effect of accepting power on triplet characteristics. And the ISC kinetics were analyzed through the theory

of fermi's golden rule. Third, we suggested the donor-acceptor-heavy atom (D-A-H) triplet photosensitizers where heavy atoms were introduced into the D-A photosensitizers to enhance the triplet characteristics. D-A-H photosensitizers showed higher triplet quantum yield and shorter triplet lifetime compared to donor-acceptor and pure heavy atom-based photosensitizers. Fourth, to further increase the triplet lifetime, methyl moieties suppressing rotation between D and A were introduced to the D-A-H-based triplet photosensitizers. As a result, a rotational restricted triplet photosensitizer showed an ultra-long triplet lifetime (1,503 $\mu$ s), which is more than 5 times higher than that of a rotational free photosensitizer. As far as we know, this is the longest triplet lifetime among the reported BODIPY based triplet photosensitizers, and is even considerably higher than that of conventional triplet photosensitizers. Ultra-long triplet lifetime caused an increase in TTA-UC properties such as TTA-UC quantum yield and threshold intensity. Therefore, we proved that the triplet characteristics can be improved considerably by rotational restriction strategy to D-A-H photosensitizers, and this result may contribute to various industrial fields using triplet photosensitizers.

**Keywords:** Triplet photosensitizers, Spin-orbit charge transfer intersystemcrossing (SOCT-ISC), Photodynamic therapy (PDT), Donor-

acceptor (DA), Triplet-triplet annihilation – upconversion (TTA-UC),  
Singlet oxygen.

**Student Number:** 2014-21469

# Contents

## Chapter 1 Introduction

|     |  |    |
|-----|--|----|
| 1.1 | Aggregation induced emission (AIE) .....                               | 1  |
| 1.2 | The basic principle of photoinduced electron transfer (PET) .....      | 3  |
| 1.3 | Marcus theory of photoinduced electron transfer.....                   | 6  |
| 1.4 | Intersystemcrossing mechanism of donor-acceptor photosensitizers ..... | 9  |
| 1.5 | Triplet-triplet annihilation upconversion (TTA-UC) .....               | 10 |
| 1.6 | References .....   | 12 |

## Chapter 2 Mechanofluorochromism of Triphenylamine-BODIPY: Effect of twisted intramolecular charge transfer and restriction in rotation on fluorescence

|     |                             |    |
|-----|-----------------------------|----|
| 2.1 | Introduction.....           | 17 |
| 2.2 | Experimentals.....          | 19 |
| 2.3 | Results and discussion..... | 24 |
| 2.4 | Conclusions .....           | 44 |
| 2.5 | References .....            | 46 |

**Chapter 3 A study on photophysical and photodynamic properties of donor–acceptor BODIPY complexes: correlation between singlet oxygen quantum yield and singlet-triplet energy gap**  
**Theoretical Formulation**

|     |                             |    |
|-----|-----------------------------|----|
| 3.1 | Introduction.....           | 56 |
| 3.2 | Experimentals.....          | 59 |
| 3.3 | Results and discussion..... | 72 |
| 3.4 | Conclusions.....            | 94 |
| 3.5 | References.....             | 95 |

**Chapter 4 Synergistic effects of photoinduced electron transfer and heavy atom effect based on BODIPY for efficient triplet photosensitizers**

|     |                             |     |
|-----|-----------------------------|-----|
| 4.1 | Introduction.....           | 102 |
| 4.2 | Experimentals.....          | 104 |
| 4.3 | Results and discussion..... | 111 |
| 4.4 | Conclusions.....            | 146 |
| 4.5 | References.....             | 147 |

**Chapter 5 Enhanced triplet-triplet annihilation upconversion luminescence through the**

## **conformational restriction based on donor - acceptor - heavy atom molecules**

|     |                                   |            |
|-----|-----------------------------------|------------|
| 5.1 | Introduction.....                 | 155        |
| 5.2 | Experimentals.....                | 158        |
| 5.3 | Results and discussion.....       | 165        |
| 5.4 | Conclusions.....                  | 191        |
| 5.5 | References.....                   | 192        |
|     | <b>Summary .....</b>              | <b>199</b> |
|     | <b>Korean Abstract.....</b>       | <b>201</b> |
|     | <b>List of Publications .....</b> | <b>204</b> |

## List of Schemes

- Scheme 2.1** Synthetic scheme of AM2 compound
- Scheme 2.2** Excitation dynamics of the evaporated and ground sample
- Scheme 3.1** Synthesis of the photosensitizers (AM1-AM4)
- Scheme 3.2** Molecular structures of BODIPY photosensitizers (AM1–AM4) and frontier molecular orbitals including the transition type.
- Scheme 3.3** SOCT-ISC between  $^1\text{CT}$  and  $^3\text{LE}$  and schematic mechanisms of the ISC process in AM2, AM3, and AM4 photosensitizers.
- Scheme 4.1** Synthesis of the photosensitizers (AM2-AM8). A triphenylamine (TPA), a BODIPY (BDP) and a perylene moiety for measuring cyclic voltammetry and TTA-UC properties
- Scheme 4.2** Schematic representation of photoinduced electron transfer in toluene (TOL) and dichloromethane (MC)
- Scheme 5.1** Synthesis of AM9 and AM10. Synthetic conditions
- Scheme 5.2** Optimized molecular structures and potential energy curve (PES) of AM9 and AM10 (ground state) along the dihedral angle between donor and acceptor.
- Scheme 5.3** Energy level diagram and photophysical process of (a) AM9 and (b) AM10 in toluene. Energy levels of the excited states are obtained with the vertical TD-DFT calculation.
- Scheme 5.4** Energy level diagram and photophysical process of (a) AM9 and (b) AM10 in ethanol. Energy levels of the excited states are obtained with the TD-DFT calculation.

## List of Tables

**Table 3.1** Parameters for determination of onsager cavity radius for molecules

**Table 3.2** Absorption and emission maximum wavelength, photophysical properties of photosensitizers in five different solvents.

**Table 3.3** Reorganization energies, singlet- triplet energy gaps and FCWDs, and SOQYs of AM1-4 photosensitizers

**Table 4.1** Absorption and emission maximum wavelength, absorption coefficients, stokes shift and photoluminescence quantum yield of photosensitizers in different solvents.

**Table 4.2** Ground state and excited state dipole moment of photosensitizers

**Table 4.3** Oxidation ( $E_{OX}$ ) and reduction ( $E_{RED}$ ) potential, charge separation driving force ( $\Delta G_{CS}$ ), reorganization energy ( $\lambda$ ), and Franck–Condon weighted density of states (FCWD)

**Table 4.4** Spin orbit coupling matrix element (SOCME) and the energy gap between the excited singlet ( $S_n$ ) and triplet ( $T_m$ ) states.

**Table 4.5** Overlap integral ( $S_r$ ), electron exchange energy ( $J$ ), singlet oxygen quantum yield ( $\Phi_{\Delta}$ ), and triplet lifetime ( $\tau_T$ ), upconversion emission efficiency ( $\eta_{UC}$ ), and threshold intensity ( $I_{th}$ ) of AM2–9 photosensitizers under excitation at 532nm

**Table 5.1** Photophysical properties of AM9 and AM10. All data was measured in toluene ( $10^{-5}M$ )

**Table 5.2** Absorption and emission maximum wavelength, photophysical properties of photosensitizers in different solvents

**Table 5.3** Redox potentials and charge separation gibbs free energy of AM9 and AM10

**Table 5.4** Upconversion emission efficiency ( $\eta_{UC}$ ) and upconversion capability ( $\phi_{UC}$ ), and threshold intensity ( $I_{th}$ ) for AM9 and AM10 in toluene

## List of Figures

**Figure 1.1** Schematic representation of aggregation caused quenching (ACQ) by H-aggregation and aggregation induced emission (AIE) by restriction in rotation (RIR) and J-aggregation.

**Figure 1.2** Schematic representation of PET process

**Figure 1.3** Potential energy curves describing photoinduced electron transfer given by the Marcus theory.  $\Delta G_{CS}^\ddagger$  is the Gibbs free energy of activation,  $\Delta G_{CS}$  is the charge separation gibbs free energy,  $\lambda$  is the reorganization energy

**Figure 1.4** Four different potential energy curves with different charge separation gibbs free energy.

**Figure 1.5** The mechanisms of spin-orbit charge transfer induced intersystemcrossing (SOCT-ISC) and hyperfine coupling induced intersystemcrossing (HFC-ISC).

**Figure 1.6** The mechanisms of triplet-triplet annihilation upconversion (TTA-UC).

**Figure 2.1** (a) Molecular structure and fluorescence spectra of the AM2 compound. (b) Reversible multi-stimuli fluorescence switching of AM2, as a function of grinding-evaporating cycle numbers. (c) Photographs of AM2 in the ground, evaporated, and crystallized states

**Figure 2.2** (a) Differential scanning calorimetry (DSC) curves of the ground and crystallized sample. (b) X-ray diffraction (XRD) curves of the crystallized, ground and evaporated sample

**Figure 2.3** (a) Aggregation-induced emission of AM2 (10 $\mu$ M) in THF/H<sub>2</sub>O mixture with different water fractions. Inset: change in intensity with respect to the water fraction. (b) Cross Polarization Magic-Angle Spinning (CP-MAS) solid-state <sup>1</sup>H NMR spectrum of AM2 in

crystallized and ground state.

**Figure 2.4** (a) A single crystal structure of AM2 and its dihedral angle between various planes. (b) The packing structure of AM2 on the plane (100), (010) and (001)

**Figure 2.5** Emission spectra of AM2 in different solvents

**Figure 2.6** (a) Schematic representation of Excitation dynamics and optimized geometry( $S_0$ ,  $S_1$ ). (b) Electron density distribution in HOMO and LUMO (corresponding to  $S_0 - S_1$  transition)

**Figure 2.7** (a) Potential energy surface (PES) of  $S_0$  and  $S_1$  electronic states, maximum absorption wavelength ( $\lambda_{abs}$ ) converted from vertical excitation energy. (b) The solid-state absorption spectrum of AM2 in crystallized and ground states.

**Figure 2.8** (a) Assigned molecular structure and (b) CP-MAS  $^{13}C$  NMR spectrum of AM2. The inset graph (b) shows the extended CP-MAS  $^{13}C$  NMR spectrum of AM2. (c) Assigned chemical shift ( $^{13}C$  NMR) of AM2.

**Figure 2.9** A  $^{13}C$  chemical shift of AM2 obtained from  $^{13}C$  NMR spectrum using GIAO-DFT method with 6-31G+(2d,p) as the function of the torsional angle.

**Figure 2.10** (a) electron density distribution of HOMO and LUMO at different torsional angles. (b) Overlap of the integral (black) and charge transfer length (red) of AM2 with increasing torsional angle

**Figure 3.1** (a) Normalized UV-VIS absorption and (b) Normalized emission spectra of the photosensitizers in hexane solution.

**Figure 3.2** Normalized UV-VIS absorption and emission spectra of the photosensitizers ( $10^{-5}$  M)

**Figure 3.3** (a) Lippert–Mataga plot in different solvents, (b) Excited state dipole moment table and graph of AM2, AM3 and AM4 calculated by using Lippert-Mataga, Bakshiev and Chamma & Viallet correlation method

**Figure 3.4** Normalized fluorescence spectra of photosensitizers ( $10^{-5}$ M) in toluene and normalized phosphorescence spectra of photosensitizers ( $10^{-5}$ M) in methylcyclohexane at 77K.

**Figure 3.5** Highest occupied and lowest unoccupied natural transition orbitals (HONTO and LUNTO) of AM1–AM4 photosensitizers

**Figure 3.6** Singlet oxygen quantum yield (SOQY) of AM1-AM4 photosensitizers of photosensitizers

**Figure 3.7** Femtosecond transient absorption spectra of AM2 (a), AM3(b) and AM4(c) in deaerated toluene at different delay times ( $\lambda_{ex}=510$  nm)

**Figure 3.8** Femtosecond transient absorption spectra of AM2 (a), AM3 (b), and AM4 (c) in deaerated TOL at different delay times ( $\lambda_{ex}=510$  nm), and their corresponding local EAS species from a global analysis of AM2 (d), AM4 (e), and AM4 (f).

**Figure 3.9** Nanosecond transient absorption spectra (left) and its decay profile (right) of (a) AM2, (b) AM3, and (c) AM4 at 430nm in deaerated toluene

**Figure 4.1** Optimized geometry, the highest occupied molecular orbital (HOMO) and lowest unoccupied molecular orbital (LUMO) of AM2-AM8 photosensitizers

**Figure 4.2** (a) UV-VIS absorption, emission spectra, and (b) Lippert-Mataga plots of AM2–AM8 photosensitizers in hexane (HX), toluene (TOL), chloroform (CF), ethyl acetate (EA), dichloromethane (MC), and acetonitrile (ACN) solutions.

**Figure 4.3** Time dependence of  $\ln([DPBF]_t/[DPBF]_0)$  in mixtures with Photosensitizers and DPBF under toluene (505nm laser excitation).

**Figure 4.4** Determination of singlet oxygen quantum yield of AM2 (a), AM5 (b), AM6 (c), AM7 (d), and AM8 (e) photosensitizers in toluene (absorbance at 505nm = 0.3)

**Figure 4.5** Determination of singlet oxygen quantum yield of AM2 (a), AM5 (b), AM6 (c), AM7 (d), and AM8 (e) photosensitizers in dichloromethane (absorbance at 505nm = 0.3)

**Figure 4.6** Cyclic voltammograms of AM2–AM8 (0.1 mM) in dichloromethane containing 0.10 M Bu<sub>4</sub>N[PF<sub>6</sub>] as the supporting electrolyte, and Ag/AgCl as the reference electrode. Scan rates: 50 mV/s. Ferrocene (Fc) was used as the external reference [ $E_{1/2} = +0.38$  V (Fc<sup>+</sup>/Fc)].

**Figure 4.7** Cyclic voltammogram of AM2, triphenylamine (TPA), BODIPY (BDP) moiety.

**Figure 4.8** Phosphorescence decay curve of AM2-AM8 photosensitizers in deaerated toluene (10<sup>-5</sup>M)

**Figure 4.9** Phosphorescence decay curve of AM2, AM6 and AM8 photosensitizers in aerated and deaerated toluene (10<sup>-5</sup>M)

**Figure 4.10** Overlap integrals (S<sub>r</sub>) of AM2-9 photosensitizers. (S<sub>1</sub>)

**Figure 4.11** Spin density of AM2, AM6, and AM8 photosensitizers (optimized T<sub>1</sub> state)

**Figure 4.12** Highest occupied natural transition orbital (HONTO) and lowest unoccupied natural transition orbital (LUNTO) of AM2-AM8 photosensitizers (S<sub>1</sub>, S<sub>2</sub>, T<sub>1</sub>, and T<sub>2</sub> states)

**Figure 4.13** Schematic of the mechanism of intersystem crossing between the excited singlet and triplet states.  $^1\text{LE}$  and  $^1\text{CT}$  states were determined by spectroscopic and cyclic voltammetric analyses. The triplet excited states were calculated by TDDFT/B3LYP/6-31+G(d,p). Natural transition orbitals (NTO) and their transition probabilities corresponding to the excited states are included.

**Figure 4.14** Spin-orbit coupling matrix element (SOCME) and energy gap ( $\Delta E_{S_1-T_1}$ ) between the  $S_1$  and  $T_1$  states of AM2–AM8

**Figure 4.15** (a) TTA-UC photoluminescence spectra of AM2–9 (inset) photographs of emission in upconversion system. (b) Upconversion intensity (log scale) and (c) upconversion emission efficiencies of AM2–9 (sensitizers:  $20\mu\text{M}$ , annihilator:  $32\mu\text{M}$ ) as a function of incident laser power density ( $\text{mW}/\text{cm}^2$ )

**Figure 4.16** Upconversion emission spectra in different concentration of AM7(photosensitizer) and perylene (annihilator) for obtaining optimized condition. The concentrations of sensitizer and perylene were selected as 10, 20,  $30\mu\text{M}$  and 8, 16, 32,  $48\mu\text{M}$  respectively.

**Figure 5.1** UV-VIS absorption and emission spectra of the photosensitizers in toluene.

**Figure 5.2** UV-VIS absorption of photosensitizers in toluene obtained by TDDFT calculation with B3LYP functional and the 6-31G+(d,p) basis set.

**Figure 5.3** UV-VIS absorption and emission spectra of photosensitizers

**Figure 5.4** Time dependence of  $\ln([\text{DPBF}]_t/[\text{DPBF}]_0)$  of mixtures with photosensitizers and DPBF in toluene (a) and ethanol (b) under irradiation (505nm green laser).

**Figure 5.5** Determination of singlet oxygen quantum yield of AM9 (a), AM10 (b), BEN-MBD-BR (c) photosensitizers in toluene (absorbance at

505nm = 0.3).

**Figure 5.6** Determination of singlet oxygen quantum yield of AM9 (a), AM10 (b) photosensitizers in ethanol.

**Figure 5.7** Time resolved photoluminescence (TRPL) decay curves of AM9 and AM10 in toluene and ethanol

**Figure 5.8** Cyclic voltammogram of Photosensitizers measured in acetonitrile. (All voltammograms were shifted based on the oxidation potential of the ferrocenium / ferrocene couple. ( $\text{Fc}^+/\text{Fc} = 0.38\text{V}$ ).

**Figure 5.9** Potential energy curve at  $T_1$  state of AM9 and AM10.

**Figure 5.10** Upconversion emission spectra with and without perylene ( $8\mu\text{M}$ ) of (a) AM9 ( $10\mu\text{M}$ ) (b) AM9

**Figure 5.11** (a) TTA-UC photoluminescence spectra of AM9 and AM10 as triplet photosensitizers ( $10\mu\text{M}$ ) and perylene as triplet annihilator ( $8\mu\text{M}$ ) using 532nm green laser (b) photograph of TTA-UC emission including triplet photosensitizers without (left) and with (right) 530nm short pass filter. (c) upconversion emission efficiencies and (d) upconversion intensity (log scale) as a function of incident laser power density ( $\text{mW}/\text{cm}^2$ ).

**Figure 5.12** Photoluminescence spectra of AM9 and AM10 with different incident laser power density

# Chapter 1

## Introduction

### 1.1 Aggregation induced emission (AIE)

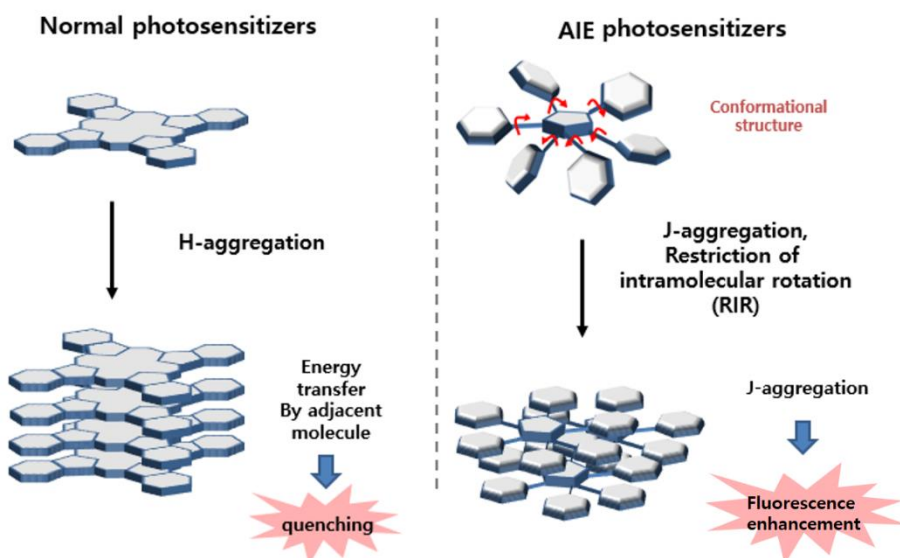


Figure 1.1 Schematic representation of aggregation caused quenching (ACQ) by H-aggregation and aggregation induced emission (AIE) by restriction in rotation (RIR) and J-aggregation.

Organic fluorophores are attracting considerable interest due to their

various applications such as bioimaging, OLED, sensor, and agricultural photoconversion film. In order to apply organic fluorophores to the industrial fields, additional processes are required. The most common processing method is to inject dispersed fluorophores into a film or to manufacture core-shell type nanoparticles by using a block copolymer. [1-7] Fluorophores in the film or nanoparticles commonly form aggregates, the aggregated molecules commonly stack face to face, which is referred to H-aggregation, resulting in the decreased fluorescence quantum yield due to the intermolecular pi-pi interaction. [8, 9] Thus the aggregated fluorophores usually show lower fluorescence quantum yield than that dissolved in dilute solutions. The aggregation induced emission (AIE) refers to the photophysical phenomenon that fluorophores show the high fluorescence properties even in the aggregated state. The most common method to induce AIE is that moieties such as tetraphenyl ethene (TPE) or triphenyl amine (TPA) are introduced into a specific fluorophore. [10, 11] These moieties are composed of rotatable components connected by single bonds, which decreases fluorescence intensity of fluorophores in dilute solution due to their rotatable components. Conversely, fluorescence of aggregated fluorophores is enhanced because of the restricted

intramolecular rotation between moieties. And these rotatable components may induce the fluorophores to exhibit highly twisted geometry, which consequently prevent face-to-face alignment of adjacent fluorophores in the aggregates. Therefore, aggregates using the AIE strategy can lead to higher fluorescence properties than conventional fluorescent materials.

## **1.2 The basic principle of photoinduced electron transfer (PET)**

Photoinduced electron transfer (PET) refers to a process in which electrons move from the electron donor to the electron acceptor in electronically excited donor acceptor (D-A) photosensitizers as light is irradiated, resulting in charge separation (charge transfer) state. [12]

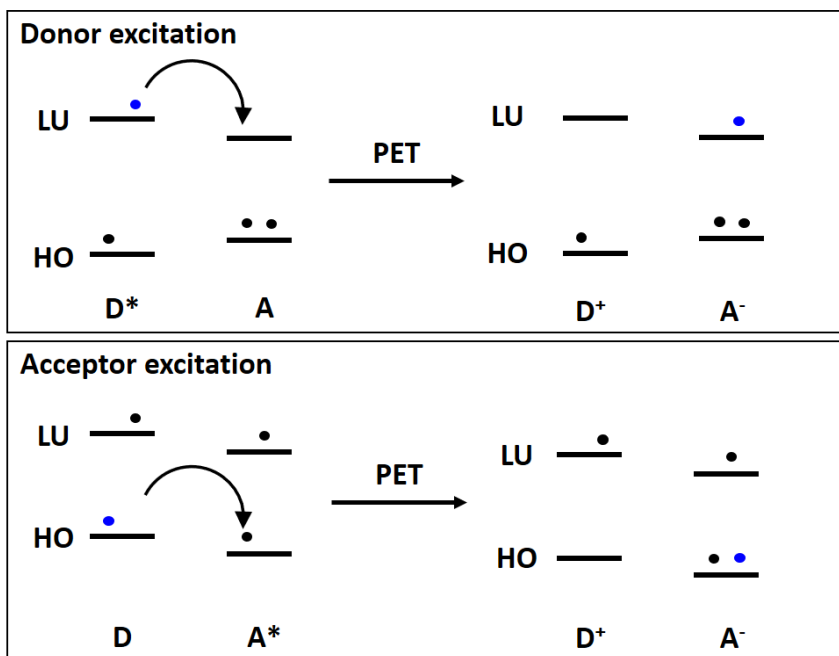


Figure 1.2 Schematic representation of PET process

Figure 1.2 is a schematic diagram showing the mechanism of PET. The mechanism of PET process is determined by the energy level alignment of an electron donor and an electron acceptor. For the electron donor excitation, electrons can move from the LUMO state of the electron donor to the LUMO state of the electron acceptor, as the LUMO of the electron donor is higher than that of the electron acceptor. On the other hand, for the electron acceptor excitation, electrons can move from the HOMO state of the electron donor to the HOMO state of the electron acceptor, as the HOMO of the electron donor is higher than

that of the electron acceptor.

The generated CT state consists of a half-filled LUMO of the electron acceptor and a half-filled HOMO of the electron donor, establishing a biradical ion pair. The CT state shows higher dipole moment compared to the D-A molecule, due to its biradical character. Therefore, the CT emission band originated from the CT state is bathochromically shifted in the high polar solvent, because the high polar solvent can stabilize the CT state.

Since this charge separation state can be sensitively changed in the surrounding environment, it can be applied to various sensors such as a temperature sensor and a polarity sensor. [13-15] In addition, the PET characteristics of D-A photosensitizers can be used as the triplet photosensitizers, because this charge separation process can provide the driving force for the electron transition from singlet to triplet excited states.

### 1.3 Marcus theory of photoinduced electron transfer

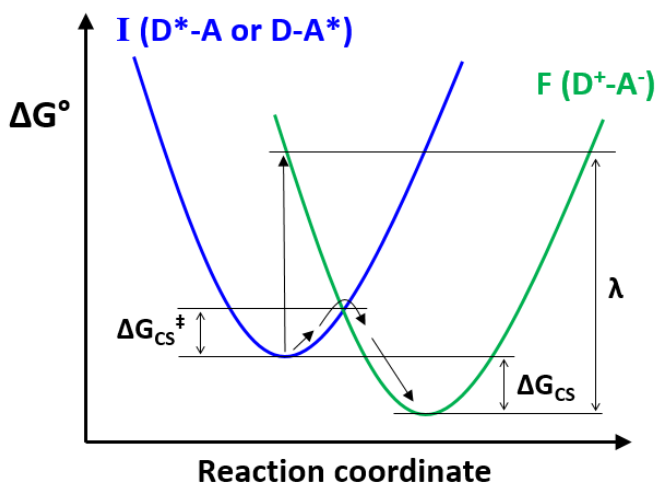


Figure 1.3 Potential energy curves describing photoinduced electron transfer given by the Marcus theory.  $\Delta G_{CS}^\ddagger$  is the Gibbs free energy of activation,  $\Delta G_{CS}$  is the charge separation Gibbs free energy,  $\lambda$  is the reorganization energy.

The PET dynamics from an initial state ( $D^*-A$  or  $D-A^*$ ) to a final state ( $D^+-A^-$ ) can be described through the classical Marcus energy transfer theory. In order to transfer energy from the initial state to the final state, the transition state corresponding to the energy barrier,  $\Delta G_{CS}^\ddagger$ , at the crossing point of initial and final potential energy curve must be overcome. Therefore, the energy transfer process can occur more

efficiently with decreasing the  $\Delta G_{CS}^\ddagger$ . And the magnitude of energy transfer can be evaluated with the charge separation rate constant, which is described by the Arrhenius expression combined with the quantum mechanical model. (eqn.1.1)

$$k_{CS} \propto A \exp(-\Delta G_{CS}^\ddagger/RT) \quad \text{eqn. 1.1}$$

The pre-exponential factor (A) correlates with the probability that electrons jump from initial curve to the final curve, and the  $\exp(-\Delta G_{CS}^\ddagger/RT)$  is the Frank-Condon factor. Assuming that the curve curvature of the potential energy curve of the initial state and the final state is the same, the mathematical relationship of  $\Delta G_{CS}^\ddagger$  with  $\Delta G_{CS}$  and  $\lambda$  is as following equation.

$$\Delta G_{CS}^\ddagger = (\Delta G_{CS} + \lambda)^2/4\lambda \quad \text{eqn.1.2}$$

where  $\Delta G_{CS}$  is the thermodynamic free energy of reaction, exhibiting the energy difference between initial and final state,  $\lambda$  is the reorganization energy, representing the energy difference between vertical single point energy of the final state at the initial geometry and optimized energy at the final state. (Figure 1.3)

According to the eqn.1.2, the magnitude of the energy transfer rate constant is determined through the relative magnitudes of  $\Delta G_{CS}$  and  $\lambda$ .

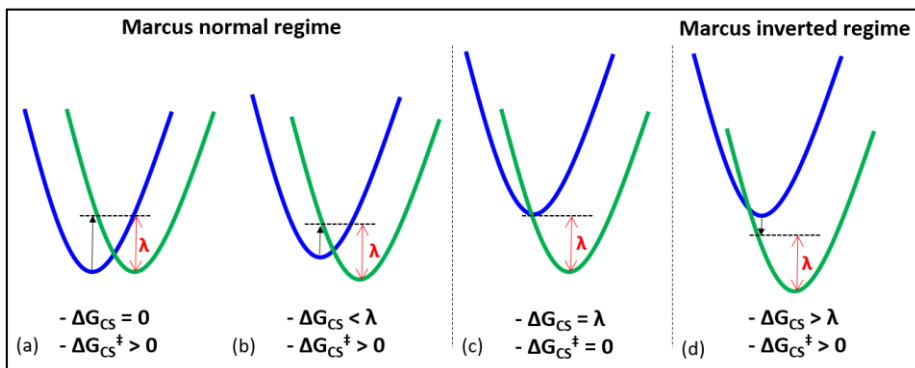


Figure 1.4 Four different potential energy curves with different charge separation gibbs free energy.

In the Marcus normal region ( $-\Delta G_{CS} < \lambda$ ), as the  $\lambda$  is constant and the  $\Delta G_{CS}$  increases,  $\Delta G_{CS}^{\ddagger}$  gradually decreases, and consequently the rate of energy transfer increases. If the magnitudes of  $-\Delta G_{CS}$  and  $\lambda$  are the same, then  $\Delta G_{CS}^{\ddagger}$  becomes 0, resulting in the largest energy transfer rate. On the other hand, in the Marcus inverted region ( $-\Delta G_{CS} > \lambda$ ), as the  $\lambda$  is constant and the  $\Delta G_{CS}$  increases,  $\Delta G_{CS}^{\ddagger}$  gradually increases, and consequently the rate of energy transfer decreases. Therefore, these two factors should be importantly considered for controlling PET characteristics.

## 1.4 Intersystemcrossing mechanism of donor-acceptor photosensitizers

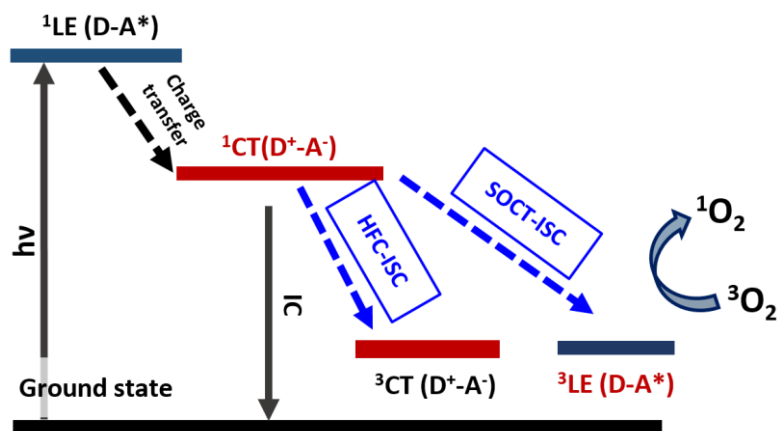


Figure 1.5. The mechanisms of spin-orbit charge transfer induced intersystemcrossing (SOCT-ISC) and hyperfine coupling induced intersystemcrossing (HFC-ISC).

According to Kasha's rule, the emission occurs in the lowest excited state, we have assumed that the photochemical reaction including intersystemcrossing of photosensitizers occurs in the lowest singlet state. The lowest singlet excited state of the D-A photosensitizer typically exhibits the  $^1\text{CT}$  state, except for conditions surrounded by a nonpolar medium.

Thus, the ISC of the D-A photosensitizer will occur from the  $^1\text{CT}$  state

to a triplet excited state adjacent to  $^1\text{CT}$  state. [16-18] As the triplet state shows the charge transfer character, that is, the  $^3\text{CT}$  state, hyperfine coupling induced intersystemcrossing (HFC-ISC) is effective for the transition from the  $^1\text{CT}$  to the  $^3\text{CT}$  states. [19] However, since it is required of extremely small  $\Delta E_{\text{ST}}$  ( $20\mu\text{eV}$ ) values for HFC-ISC to occur, the contribution of the HFC-ISC in total ISC might not be significant. [20] In contrast, as the triplet state shows the local excited character, that is, the  $^3\text{LE}$  state, spin-orbit coupling induced intersystemcrossing (SOCT-ISC) is effective for the transition from the  $^1\text{CT}$  to the  $^3\text{LE}$  states. [19] An orthogonal arrangement of the electron donor and the electron acceptor is required for the SOCT-ISC to occur. As the light is irradiated on the orthogonal molecule, the charge is transferred vertically from a hole to a particle, which compensates the spin angular momentum. And this induces the spin flip, resulting in the ISC. In this study, it is assumed that the SOCT-ISC is mainly contribute to the total ISC. [21]

## **1.5 Triplet-triplet annihilation upconversion (TTA-UC)**

Upconversion (UC) emission is a phenomenon in which photons of low energy are absorbed and converted into high energy photons,

thereby generating shorter wavelength photons compared to the incident photons. This is the opposite of down conversion emission, in which common fluorescent materials absorb photons of higher energy and generate photons of lower energy. UC has been considered as a promising technology that improves the performance of solar cells and bio-imaging.

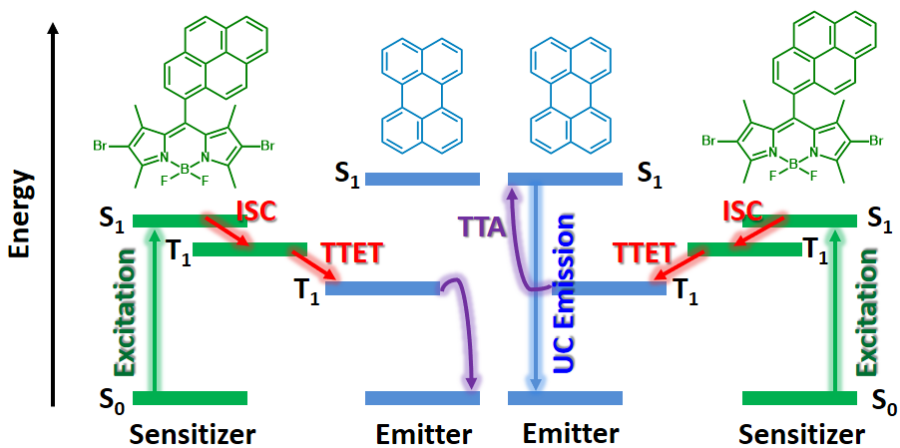


Figure 1.5. The mechanisms of triplet-triplet annihilation upconversion (TTA-UC).

In particular, triplet-triplet annihilation upconversion (TTA-UC) has received considerable attention because UC can be operated by non-coherent light source at low power densities (<100 mW/cm<sup>2</sup>). [22-24] To implement TTA-UC, two components, a triplet sensitizer and an

annihilator, are required. As the light is irradiated to the TTA-UC system, triplet sensitizers absorb low energy photons and populate triplet electrons at triplet excited states (Figure 1.5). And the triplet electrons (or energies) are transferred to the annihilator, termed by triplet-triplet energy transfer (TTET). When two triplet annihilators encounter each other, one of two annihilators may become a singlet excited state ( $S_1$ ) electron, and the other may convert ground singlet state ( $S_0$ ). In the TTA-UC system, the  $S_1$  state of the annihilator has a higher energy level than that of the triplet sensitizers, so the emission energy of annihilator is higher than the absorption energy of triplet sensitizers, resulting in UC.

## 1.6 References

- [1] Wolfbeis OS. An overview of nanoparticles commonly used in fluorescent bioimaging. *Chemical Society Reviews*. 2015;44(14):4743-68.
- [2] Burns A, Ow H, Wiesner U. Fluorescent core-shell silica nanoparticles: towards "Lab on a Particle" architectures for nanobiotechnology. *Chemical Society Reviews*. 2006;35(11):1028-42.
- [3] Klymchenko AS. Emerging field of self-assembled fluorescent

organic dye nanoparticles. *J Nanosci Lett.* 2013;3:21.

[4] Demchenko AP. Nanoparticles and nanocomposites for fluorescence sensing and imaging. *Methods and applications in fluorescence.* 2013;1(2):022001.

[5] Liu M, Gao P, Wan Q, Deng F, Wei Y, Zhang X. Recent Advances and Future Prospects of Aggregation-induced Emission Carbohydrate Polymers. *Macromolecular rapid communications.* 2017;38(10):1600575.

[6] Elsabahy M, Heo GS, Lim S-M, Sun G, Wooley KL. Polymeric nanostructures for imaging and therapy. *Chemical reviews.* 2015;115(19):10967-1011.

[7] Reisch A, Klymchenko AS. Fluorescent polymer nanoparticles based on dyes: seeking brighter tools for bioimaging. *Small.* 2016;12(15):1968-92.

[8] Geng J, Li K, Ding D, Zhang X, Qin W, Liu J, et al. Lipid-PEG-Folate Encapsulated Nanoparticles with Aggregation Induced Emission Characteristics: Cellular Uptake Mechanism and Two-Photon Fluorescence Imaging. *Small.* 2012;8(23):3655-63.

[9] Zheng Q, Ohulchansky TY, Sahoo Y, Prasad PN. Water-dispersible polymeric structure co-encapsulating a novel hexa-peri-

hexabenzocoronene core containing chromophore with enhanced two-photon absorption and magnetic nanoparticles for magnetically guided two-photon cellular imaging. *The Journal of Physical Chemistry C*. 2007;111(45):16846-51.

[10] Yang M, Xu D, Xi W, Wang L, Zheng J, Huang J, et al. Aggregation-induced fluorescence behavior of triphenylamine-based schiff bases: the combined effect of multiple forces. *The Journal of organic chemistry*. 2013;78(20):10344-59.

[11] Gomez-Duran CFA, Hu R, Feng G, Li T, Bu F, Arseneault M, et al. Effect of AIE substituents on the fluorescence of tetraphenylethene-containing BODIPY derivatives. *ACS applied materials & interfaces*. 2015;7(28):15168-76.

[12] Kavarnos GJ. *Fundamentals of photoinduced electron transfer*: VCH New York, 1993.

[13] Xing Y, Lin H, Wang F, Lu P. An efficient D–A dyad for solvent polarity sensor. *Sensors and Actuators B: Chemical*. 2006;114(1):28-31.

[14] Wang X-d, Wolfbeis OS, Meier RJ. Luminescent probes and sensors for temperature. *Chemical Society Reviews*. 2013;42(19):7834-69.

[15] Fujitsuka M, Tsuboya N, Hamasaki R, Ito M, Onodera S, Ito O, et al.

Solvent Polarity Dependence of Photoinduced Charge Separation and Recombination Processes of Ferrocene– C60 Dyads. *The Journal of Physical Chemistry A*. 2003;107(10):1452-8.

[16] Dance ZE, Mickley SM, Wilson TM, Ricks AB, Scott AM, Ratner MA, et al. Intersystem crossing mediated by photoinduced intramolecular charge transfer: julolidine– anthracene molecules with perpendicular  $\pi$  Systems. *The Journal of Physical Chemistry A*. 2008;112(18):4194-201.

[17] Zhao Y, Duan R, Zhao J, Li C. Spin–orbit charge transfer intersystem crossing in perylenemonoimide–phenothiazine compact electron donor–acceptor dyads. *Chemical Communications*. 2018;54(87):12329-32.

[18] Wang Z, Ivanov M, Gao Y, Bussotti L, Foggi P, Zhang H, et al. Spin–Orbit Charge-Transfer Intersystem Crossing (ISC) in Compact Electron Donor–Acceptor Dyads: ISC Mechanism and Application as Novel and Potent Photodynamic Therapy Reagents. *Chemistry–A European Journal*. 2020;26(5):1091-102.

[19] Gibbons DJ, Farawar A, Mazzella P, Leroy-Lhez S, Williams RM. Making triplets from photo-generated charges: observations, mechanisms and theory. *Photochemical & Photobiological Sciences*. 2020;19(2):136-58.

- [20] Dias FB, Santos J, Graves DR, Data P, Nobuyasu RS, Fox MA, et al. The role of local triplet excited states and D-A relative orientation in thermally activated delayed fluorescence: photophysics and devices. *Advanced Science*. 2016;3(12):1600080.
- [21] Dance ZE, Mickley SM, Wilson TM, Ricks AB, Scott AM, Ratner MA, et al. Intersystem crossing mediated by photoinduced intramolecular charge transfer: julolidine– anthracene molecules with perpendicular  $\pi$  Systems. *The Journal of Physical Chemistry A*. 2008;112(18):4194-201.
- [22] Simon YC, Weder C. Low-power photon upconversion through triplet–triplet annihilation in polymers. *Journal of Materials Chemistry*. 2012;22(39):20817-30.
- [23] Penconi M, Ortica F, Elisei F, Gentili PL. New molecular pairs for low power non-coherent triplet–triplet annihilation based upconversion: dependence on the triplet energies of sensitizer and emitter. *Journal of luminescence*. 2013;135:265-70.
- [24] Lyu L, Cheong H, Ai X, Zhang W, Li J, Yang H, et al. Near-infrared light-mediated rare-earth nanocrystals: recent advances in improving photon conversion and alleviating the thermal effect. *NPG Asia Materials*. 2018;10(8):685-702.

## **Chapter 2**

# **Mechanofluorochromism of Triphenylamine-BODIPY: Effect of twisted intramolecular charge transfer and restriction in rotation on fluorescence**

### **2.1 Introduction**

Mechanofluorochromism (MFC) refers to the phenomenon wherein the color of the luminogens change according to the external stimuli. A considerable amount of literature has been published on MFCs due to their potential use in various applications, such as security paper and optical storage. The causes of MFC phenomena can be divided into two types: (1) changes in the arrangement of molecules and (2) variations in the conformation of molecules caused by external stimuli. Due to changes in temperature or pressure, the molecular arrangement can be modified to ensure that the crystalline phase is destroyed or transforms to the amorphous phase. Such molecular rearrangements have been

observed to affect the magnitude of the intermolecular  $\pi$ - $\pi$  interactions, and may even modify the aggregation type (such as J-type and H-type), resulting in altered fluorescence properties. [1-3] Conversely, in the case of a donor (D)-acceptor (A) complex consisting of one or more rotatable components, the emission spectra and intensity can be affected by the modified conformation. [4-7] The mechanical stress induces conformational planarization, modulating the strength of intramolecular charge transfer (ICT). A number of studies on MFC have asserted that the emission spectrum shift caused by the conformational change in D-A luminogens, was related to twisted intramolecular charge transfer (TICT) or planar intramolecular charge transfer (PICT). However, the theories relating to TICT and PICT contradict each other. [5, 8-21] Although numerous studies have suggested a mechanism, it has not been determined if the reaction is caused by TICT, PICT, or other factors related to ICT. The mechanism has not been confirmed, due to a lack of results, as the absorption and emission spectra were presented as the only evidence for T or PICT without structural identification of conformation. In addition, previous studies have reported that MFC luminogens commonly exhibit aggregation-induced emission (AIE) characteristics, which draw a reasonable inference that the MFC

phenomenon is deeply related to restriction in rotation (RIR), which is a key factor of AIE. [5, 10, 12-14, 16, 18, 19, 22-26] Despite this, research has not been sufficiently conducted to prove it yet. Hence, our study has been aimed to systematically examine the mechanisms of MFCs related to AIE and ICT characteristics. In particular, the correlation between the torsional angle of molecules and ICT strength was analyzed by conformational analysis through quantum chemical calculations. The relevance of the fluorescence intensity under mechanical stress with the restriction in rotation (RIR) was examined by <sup>1</sup>H magic angle spinning (MAS) solid-state NMR.

## **2.2 Experimentals**

### **2.2.1 Materials**

All of the commercial reagents were purchased from Sigma-Aldrich, Tokyo Chemical Industry (TCI) and Alfa aesar, which used without further purification. Anhydrous solvents used in the reactions were purchased from Sigma-Aldrich and Alfa aesar.

### **2.2.2 Instruments**

Instruments  $^1\text{H}$ ,  $^{13}\text{C}$  and 2D HSQC NMR spectra were recorded on a Bruker Avance 500 spectrometer (National Center for Inter-University Research Facilities at Seoul National University) at 500 MHz. High resolution mass experiments were operated on a Q-TOF 5600 mass spectrometer equipped with an ESI source (National Instrumentation Center for Environmental Management). Solid state UV–vis absorption spectra were measured using a UV-Vis spectrophotometer (Varian Cary 5G, Agilent Co.). Solvatochromic absorption and fluorescence solutions were measured by an UV–vis spectrophotometer (LAMBDA 25, Perkin Elmer Co.) and a fluorescence spectrometer (LS-55, Perkin Elmer Co.), respectively. Photoluminescence (PLQY) of 10  $\mu\text{M}$  photosensitizers solutions were estimated using an integrating sphere (QE-1100, Otsuka electronics Co.).

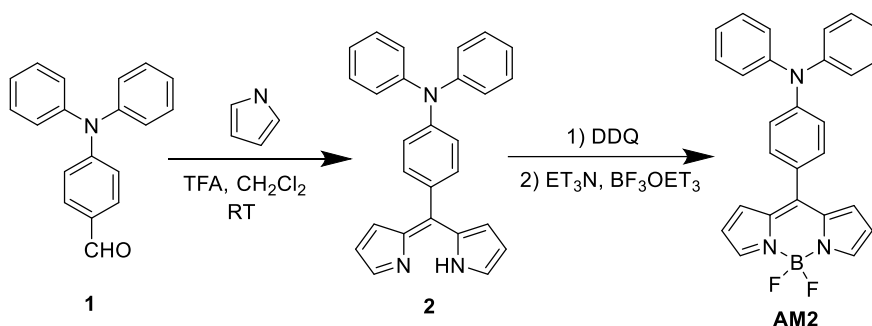
### **2.2.3 General methods**

The crystal structures of the crystals were determined by single-crystal diffraction methods at the Korea Basic Science Institute (KBSI, Western Seoul Center, Korea). Brown rod crystal ( $0.27 \times 0.13 \times 0.10$

mm<sup>3</sup>) was picked up with paratone oil and mounted on a Bruker D8 Venture PHOTON 100 CMOS diffractometer equipped with a graphite-monochromated Mo K $\alpha$  ( $\lambda = 0.71073 \text{ \AA}$ ) radiation source and a nitrogen cold stream ( $-50^\circ\text{C}$ ). Data collection and integration were performed with SMART APEX2 (Bruker, 2012) and SAINT (Bruker, 2012) [47]. Absorption correction was performed by multi-scan method implemented in SADABS. [48] The structure was solved by direct methods and refined by full-matrix least-squares on F<sup>2</sup> using SHELXTL. [49] All the non-hydrogen atoms were refined anisotropically, and hydrogen atoms were added to their geometrically ideal positions. The ground-state geometry was optimized with Gaussian 09 software using the B3LYP hybrid functional and the 6-31G (d, p) basis set. A <sup>1</sup>H cross-polarization/magic angle spinning (CP/MAS) NMR spectrum of the AM2 was recorded with spinning rate of 5kHz and <sup>13</sup>C cross-polarization/magic angle spinning (CP/MAS) NMR spectrum was obtained at a spinning rate of 5 kHz, with a 5 s delay time, 2ms contact time and 1k scans. NMR data were obtained from a 500 MHz Avance III HD Bruker Solid-state NMR at the National Center for Inter-University Research Facilities (NCIRF) at Seoul National University. The overlap integral and charge transfer length of AM2 were obtained using Multiwfn

software. [50] DSC curve of AM2 was measured from 30 °C to 250 °C at heating rate of 10°C/min.

## 2.2.4 Synthesis



Scheme 2.1. synthetic scheme of AM2 compound

**4-(di(1H-pyrrol-2-yl)methyl)-N,N-diphenylaniline (2)** In three neck round bottom flask, 4-(Diphenylamino)benzaldehyde(1.05g, 3.85 mmol) and pyrrole (1.033g, 15.4 mmol, 4eqn) were dissolved into dry dichloromethane (250 mL), then a solution of trifluoroacetic acid (0.5 mmol, 0.13eqn) in dry dichloromethane (2.5 mL) were slowly added to the mixture at room temperature under N<sub>2</sub> atmosphere. Then the reaction mixture was quenched by 2 mL, trimethylamine and evaporated. The brown, oily residue is simply purified by column chromatography on silica with CH<sub>2</sub>Cl<sub>2</sub>: n-hexane = 1:1 to produce **2** as brown solid (1.47g).

**AM2** 2,3-Dichloro-5,6-dicyano-1,4-benzoquinone (DDQ) (0.87 g, 3.85

mmol) was added to the crude mixture of **2**(700mg) under ice bath cooling and stirred for 10 min. The solution is stirred for an additional 1 h at room temperature. Triethylamine (55.44 mmol, 14.5eqn) is added, followed by slow addition of BF<sub>3</sub> Et<sub>2</sub>O (62.37 mmol, 16.2eqn). After 2 h, the reaction mixture was washed at room temperature with saturated aqueous Na<sub>2</sub>CO<sub>3</sub> solution (3 x 100 mL), dried over MgSO<sub>4</sub>, and concentrated on a rotary evaporator. The brown, oily residue is purified by column chromatography on silica with CH<sub>2</sub>Cl<sub>2</sub>: n-hexane = 2:1 to produce AM2 as red-brown solid. (250 mg, 13% yield). <sup>1</sup>H NMR (500 MHz, CDCl<sub>3</sub>) δ 7.90 (s, 2H), 7.49-7.44 (d, J=8.7Hz, 2H), 7.39-7.32 (t, J=7.5Hz, 4H), 7.25-7.00 (d, J=7.5Hz, 4H), 7.19-7.13 (t, J=7.4Hz, 2H), 7.13-7.08 (d, J=8.6Hz, 2H), 7.08-7.04 (d, J=4.0Hz, 2H), 6.5 (m, 2H) <sup>13</sup>C NMR (500 MHz, CDCl<sub>3</sub>) δ 151.1, 147.7, 146.6, 142.9, 134.8, 132.5, 131.3, 129.9, 126.4, 126.1, 124.9, 120.2, 118.2; HRMS-ESI (M+H<sup>+</sup>) Calcd for C<sub>27</sub>H<sub>21</sub>BF<sub>2</sub>N<sub>3</sub>: 436.1796. Found: 436.1772

## Results and discussion

### 2.3.1 Molecular designs

BODIPY is widely used as a fluorescent luminogen because of its excellent absorption coefficient, fluorescence quantum yield, and photostability. [27-30] Despite their outstanding optical properties, very few studies have investigated the MFC of BODIPY. [31-33]

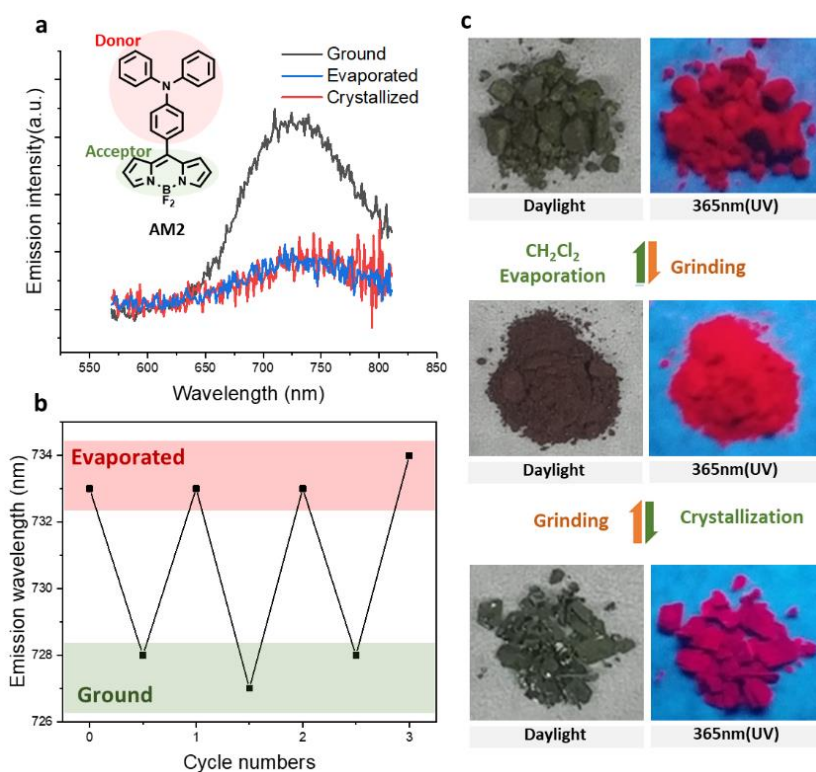


Figure 2.1. (a) Molecular structure and fluorescence spectra of the AM2 compound. (b) Reversible multi-stimuli fluorescence switching of AM2,

as a function of grinding-evaporating cycle numbers. (c) Photographs of AM2 in the ground, evaporated, and crystallized states

And results of previous studies with BODIPY showed good performance of MFC and piezochromism. Thus we designed and synthesized a donor-acceptor (D-A) complex based on boron dipyrromethane (BODIPY). The triphenylamine (TPA) moiety was attached to the meso position of BODIPY for three reasons. [34-39] First, the TPA functional group is suitable as a donor because of its excellent donating power. Second, it is one of the most widely used groups for AIE owing to its freely rotatable propeller structure (Figure 2.1a inset). Third, it is well known that the meso position is highly sensitive to the substituent effect.

The MFC properties of the AM2 are shown in Figure 2.1. Pristine (evaporated) samples were dark green in daylight and showed a weak red emission under UV light. However, the color changed to reddish-brown under daylight and showed strong red emission in UV light after grinding with a mortar and pestle (Figure 2.1c). The annealing procedure did not change the color of AM2 even at 200 °C for 1 h, which indicates that thermal stimuli cannot affect the molecular structure. The crystallization procedure, however,

changed the color of AM2 under UV light, only to have a weak red emission.

These results were consistent with the fluorescence spectra obtained. The emission spectra of the ground, evaporated, and (re)crystallized samples are shown in Figure 2.1a. The emission maximum of AM2 was hypsochromically shifted by 5 nm, and its intensity increased with grinding. The color characteristics were recovered to the original state with DCM treatment and evaporation (wetted with dichloromethane and evaporated at 50 °C), demonstrating evident MFC characteristics.

In addition, AM2 showed superior color reversibility with three cycles of grinding and evaporation without any fatigue, indicating that AM2 is a good candidate as an MFC luminogen (Figure 2.1b).

### **2.3.2. Powder x-ray diffraction (PXRD) and differential scanning calorimetry (DSC)**

Powder X-ray diffraction (XRD) and differential scanning calorimetry (DSC) were applied to determine whether the MFC was caused by changes due to molecular rearrangement (Figure 2.2).

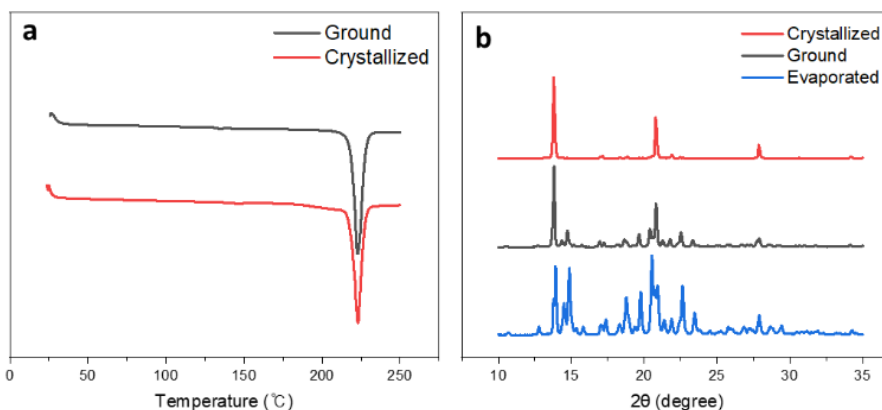


Figure 2.2. (a) Differential scanning calorimetry (DSC) curves of the ground and crystallized sample. (b) X-ray diffraction (XRD) curves of the crystallized, ground and evaporated sample

The DSC and XRD data is commonly used to show that MFC is caused by different crystallinities or by distinctions between the crystalline and amorphous phases. In the DSC thermogram, both samples showed approximately identical peaks; a single endothermic peak at 223 °C, corresponding to the melting point, was present; and no cold crystallization peaks were detected. The crystallinity of the ground sample was 99.77%, when that of the crystallized sample was assumed to be 100%. This indicates that both samples appear to have a pure crystalline form, which can explain why the fluorescence character of the ground sample was maintained even after the annealing process.

In the XRD spectrum, the evaporated, crystallized, and ground samples showed various sharp peaks without diffuse halo patterns. It can thus be considered that all the samples consisted of only the crystalline phase. The XRD pattern of the crystallized sample showed three apparent peaks in the range of 10-30 degrees ( $2\theta$ ); this indicates that the crystallized sample is single crystal with no other crystal phases.

Conversely, except for the three major peaks, there were additional sharp miscellaneous peaks present in the XRD pattern of the evaporated and ground samples. These results indicate that both samples are polymorphs, with numerous crystal phases. Thus it can be considered the degree of polymorphism were increased in the order of the evaporated>ground>crystallized samples.

Despite the evaporated and crystallized samples having the highest and the lowest degree of polymorphism, they showed nearly the same emission properties. The ground sample with an intermediate degree of polymorphism showed distinct fluorescence characteristics from the other samples. This means that the degree of polymorphism was not a key factor in determining MFC properties.

Overall, these results of DSC and XRD indicate that the origin of MFC is not from the intermolecular structural changes of AM2, which might induce weak fluorescence enhancement and slight wavelength change upon grinding.

### **2.3.3 Correlation between MFC and Restriction in rotation (RIR)**

The investigation of ICT and AIE properties is required as the MFC properties of D-A complex are closely associated with them. In particular, it can be presumed that the RIR causes a significant increase in the emission spectra after grinding. Under external pressure, the intermolecular distance decreases and the movement of the molecules is hindered by the other molecules. As a result, rotational movement is decreased, and fluorescence quenching of sensitizers was eventually suppressed.

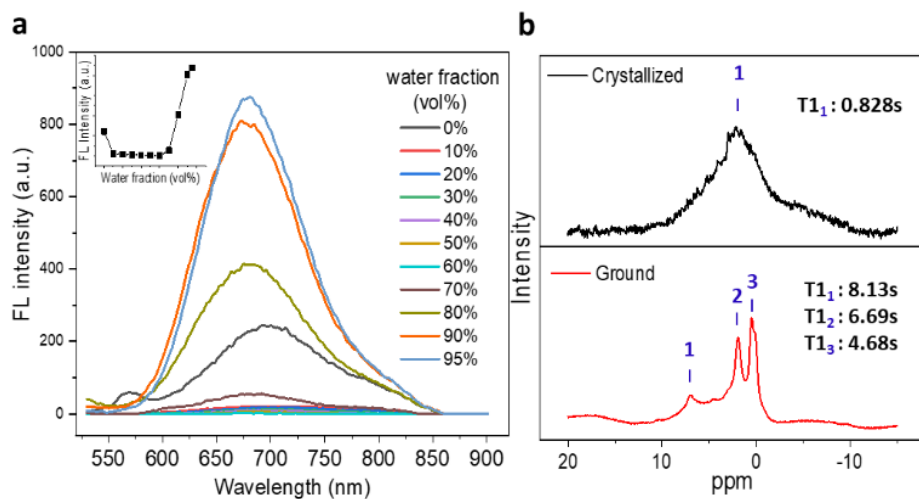


Figure 2.3 (a) Aggregation-induced emission of AM2 (10 $\mu$ M) in THF/H<sub>2</sub>O mixture with different water fractions. Inset: change in intensity with respect to the water fraction. (b) Cross Polarization Magic-Angle Spinning (CP-MAS) solid-state <sup>1</sup>H NMR spectrum of AM2 in crystallized and ground state.

To demonstrate this relationship between MFC and RIR, the emission spectrum of AM2 was measured in a mixed solvent system with different ratios of THF/H<sub>2</sub>O (Figure 2.3a). When the water fraction ( $f_w$ ) is between 10% and 60%, the emission intensity of AM2 is minimal; such fluorescence quenching is a common property of D-A molecules, caused by ICT due to the increased polarity of the solvent. [40] In contrast, from 70%  $f_w$ , the emission

intensity gradually increased, and at 95%  $f_w$ , the intensity of fluorescence was about 3.7-fold stronger than that of 0%  $f_w$ . These results exhibit the AIE property of the D-A complex, which indicates that the RIR property of AM2 can potentially be modulated for its emission intensity by external stimuli variation.

$^1\text{H}$  solid-state NMR (ssNMR) spectra were measured to compare the magnitude of RIR between crystallized and ground samples, since the spin-lattice relaxation time ( $T_1$ ) is normally used to probe the local or global mobility of molecules (Figure 2.3b). [41-45] Unlike the ground sample, which showed three relatively sharp peaks, the crystallized sample showed broad spectra over the range of 0-10 ppm. The  $T_{12}$  of the ground sample and  $T_{11}$  of the crystallized sample can be assigned to the same proton as they are observed at 1.92 and 2.02ppm, respectively. The  $T_{12}$  of the ground sample was about eight times longer than the  $T_{11}$  of the crystallized sample, indicating that the molecular motions of the ground sample are not sufficient to transfer energy to the surrounding lattice.

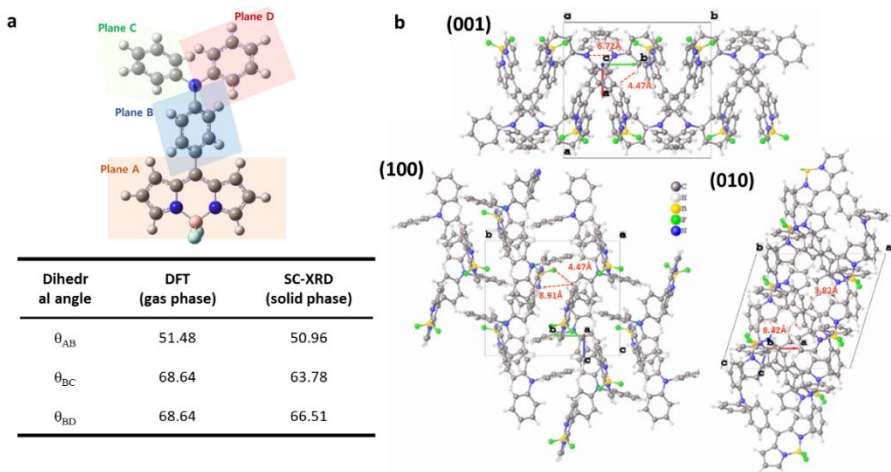


Figure 2.4 (a) A single crystal structure of AM2 and its dihedral angle between various planes. (b) The packing structure of AM2 on the plane (100), (010) and (001)

The evaporated samples, instead, exhibited a short relaxation time, as the molecular structure consists of freely rotating components. Thus, the mobile regions act as a relaxation sink for the whole molecule, allowing the molecules to relax quickly via proton spin diffusion. The crystal structure of the sample determined by single crystal X-ray diffraction (sc-XRD) analysis supported these results. The intermolecular distance was greater than 3.82 Å, which is far enough that molecules cannot affect each other (Figure. 2.4b). Figure 2.4a shows three dihedral angles ( $\theta_{AB}$ ,

$\theta_{BC}$ , and  $\theta_{BD}$ ), which consider the possible conformational variation in the molecule.

These angles were obtained from sc-XRD (in the solid phase) and geometry optimization using DFT B3LYP 6-31G d,p (in the gas phase). In the solid phase,  $\theta_{AB}$ ,  $\theta_{BC}$ , and  $\theta_{BD}$  were  $0.52^\circ$ ,  $4.86^\circ$  and  $2.13^\circ$  smaller than the gas phase, respectively. This indicates that the molecules in solid were more planar than the gas phase, which may indicate that planarization occurs as the intermolecular distance gets closer. However, the angular differences were small, which means each molecule in solid phase could not significantly affect molecular geometry, allowing molecules to rotate freely. Thus far, we have shown that the RIR induced by external stimuli can suppress the fluorescence quenching process. The following section investigates the relationship between MFC and ICT properties.

#### **2.3.4 Correlation between MFC and Intramolecular charge transfer (ICT)**

As mentioned earlier, the emission spectrum shift of D-A sensitizers under external stimuli is associated with variations in

ICT character. According to previous research on D-A MFC luminogens, most of their molecules showed bathochromic emission shifts under external stimuli. These studies argued that MFC was due to the extended conjugation or the enhanced ICT strength of molecules based on PICT under external stress. [8-11] Such explanations are insufficient because they did not examine whether their MFC luminogens showed PICT characteristics and did not investigate the direct relationship between conjugation extension and bathochromic shift. With grinding, the AM2 showed a hypsochromic emission shift, unlike luminogens reported in other papers showed bathochromic emission shift. Therefore, the MFC properties of AM2 cannot be explained by extension of conjugation or PICT, which are the results of previous research. Instead, a possible explanation for this might be the TICT because molecular planarization decreases ICT character, and thus induces hypsochromic emission shift based on the TICT theory.

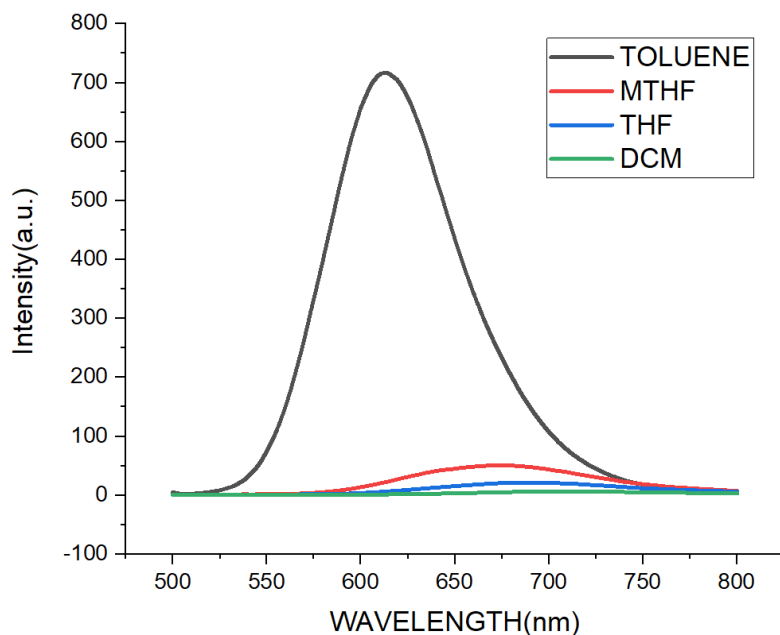


Figure 2.5 Emission spectra of AM2 in different solvents (Toluene, methyl tetrahydrofuran (MTHF), tetrahydrofuran (THF) and dichloromethane (DCM))

To test this hypothesis, we measured the emission spectra in various solvents (Figure 2.5). With an increase in the solvent polarizability, the intensity of emission decreased and emission spectra moved to the red region. In addition, the shape of emission became broad and flat, indicating the strong ICT character of the AM2. We also performed DFT and time-dependent density functional theory (TDDFT) quantum calculations to obtain qualitative ICT analysis (Figure 2.6).

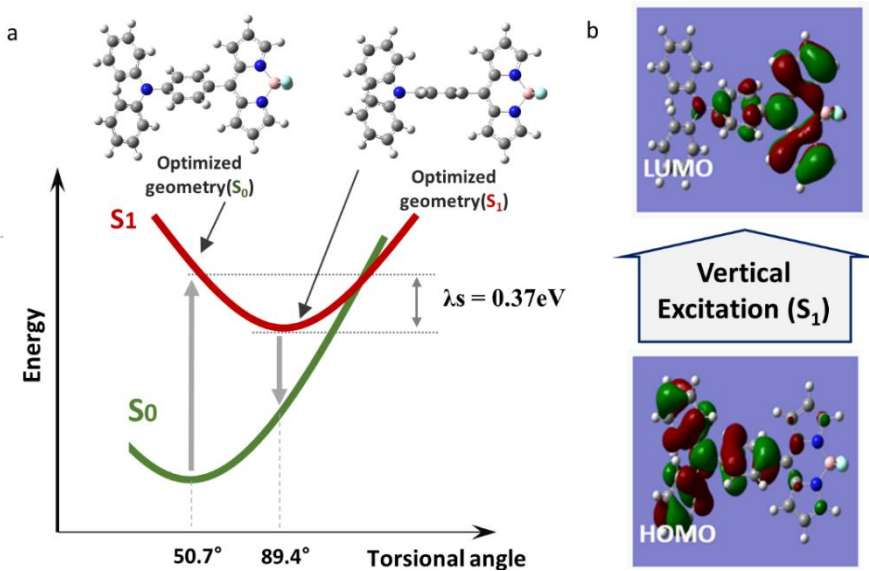


Figure 2.6 (a) Schematic representation of Excitation dynamics and optimized geometry (S<sub>0</sub>, S<sub>1</sub>). (b) Electron density distribution in HOMO and LUMO (corresponding to S<sub>0</sub> – S<sub>1</sub> transition)

TDDFT calculations showed that the electronic excitation of S<sub>0</sub> to S<sub>1</sub> corresponds to the orbital transition from HOMO to LUMO. The electron density distributions of HOMO and LUMO were mainly located on triphenylamine (D) and BODIPY (A), respectively, exhibiting an evident ICT characteristic.

### 2.3.5 Correlation between MFC and molecular geometry

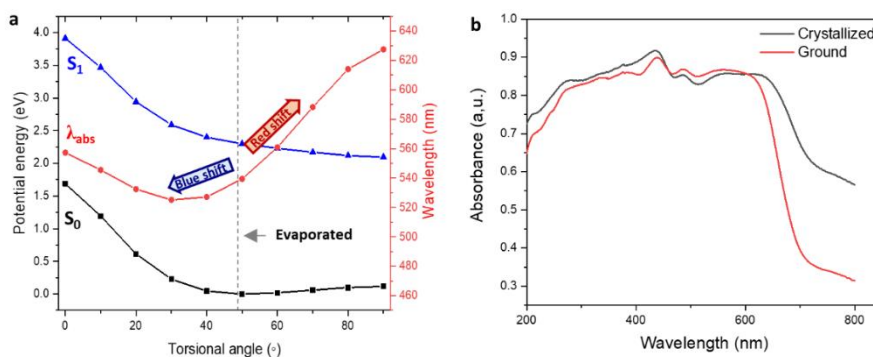


Figure 2.7 (a) Potential energy surface (PES) of S<sub>0</sub> and S<sub>1</sub> electronic states, maximum absorption wavelength ( $\lambda_{\text{abs}}$ ) converted from vertical excitation energy. (b) The solid-state absorption spectrum of AM2 in crystallized and ground states.

The energy level of the optimized singlet excited state was 0.37 eV lower than that of the Franck-Condon (FC) excited state, which means the geometry of the excited state was largely changed during the photoexcitation process. The most noticeable difference between the optimized S<sub>1</sub> and the optimized S<sub>0</sub> geometry was the torsional angles ( $\theta_{\text{AB}}$ ) of the donor and acceptor. That is, the  $\theta_{\text{AB}}$  of optimized S<sub>1</sub> state molecules was 89.4°, unlike 50.7° of the

optimized S0 state molecules. This is because of the charge separated S1 state with a high dipole moment, which can be stabilized by the high torsional angle between D-A; this may be an evidence that AM2 exhibits TICT characteristics. These results suggest that one of the major factors determining fluorescence properties is the torsional angle between donor and acceptor. We have, thus, explored intramolecular potential energy surface (PES) of S1 and S0 state as a function of torsional angle using (TD) DFT calculations (Figure 2.7a). The  $\lambda_{\text{abs}}$  indicates the absorption wavelength obtained by converting the energy difference between S1 and S0 states at a specified torsional angle. It should be noted that the torsional angle of the crystallized sample was  $50.7^\circ$  from the previous sc-XRD section. As  $\theta_{\text{AB}}$  increased from  $50.7^\circ$ ,  $\lambda_{\text{abs}}$  moved to longer wavelengths (bathochromic shift). while as  $\theta_{\text{AB}}$  decreased up to roughly  $20^\circ$ , the  $\lambda_{\text{abs}}$  was hypsochromically shifted. The absorption spectrum of the ground sample was shorter than that of the crystallized sample, the torsional angle of the ground sample was, therefore, approximately in the range of  $20$ - $50^\circ$  (Figure 2.7b). This result directly demonstrates that external stimuli (grinding) induced molecular planarization.

To support this, the Cross Polarization Magic-Angle Spinning (CP-MAS)  $^{13}\text{C}$  NMR experiment was applied in a solid state. When comparing the  $^{13}\text{C}$  NMR spectrum of the ground sample and the crystallized sample, most of the peaks except  $\text{C}_2$  (127ppm) and  $\text{C}_3$  (130ppm) showed nearly similar shapes and values. Both  $\text{C}_2$  and  $\text{C}_3$  peaks of the crystallized sample were divided into two peaks. The two separated peaks of  $\text{C}_2$  ( $\text{C}_3$ ) can be assigned to  $\text{C}_{2a}$  and  $\text{C}_{2b}$  ( $\text{C}_{3a}$ ,  $\text{C}_{3b}$ ), respectively, as depicted in Figure 2.8a, which means that  $\text{C}_{2a}$  and  $\text{C}_{2b}$  ( $\text{C}_{3a}$ ,  $\text{C}_{3b}$ ) are in different chemical shielding environments.

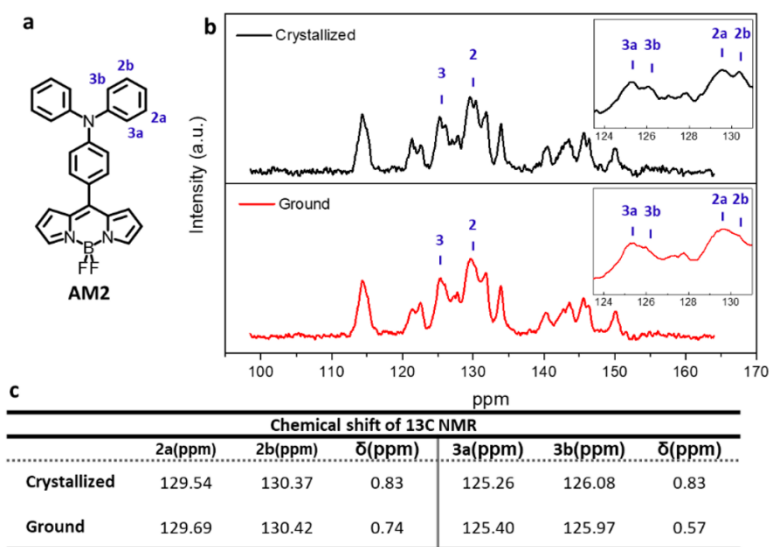


Figure 2.8 (a) Assigned molecular structure and (b) CP-MAS  $^{13}\text{C}$  NMR spectrum of AM2. The inset graph (b) shows the extended CP-MAS  $^{13}\text{C}$  NMR spectrum of AM2. (c) Assigned chemical shift ( $^{13}\text{C}$  NMR) of AM2.

This may suggest that the electron density of 2a and 2b (3a and 3b) was predominantly affected more than that of other carbons.

[46] The graph of the ground sample appeared to show one peak due to their decreased chemical shielding difference. However, in the enlarged graph, the hidden peaks can be found at the point where the slope of the graph changes slightly. The quantitative chemical shifts of both samples are shown in Figure 2.8c. The  $\delta\text{ppm}$  indicates the chemical shift difference between separated peaks of  $\text{C}_2$  or  $\text{C}_3$  in each sample. The  $\delta\text{ppm}$  of  $\text{C}_2$  (0.7357) and  $\text{C}_3$  (0.5701) in the ground sample were lower than in the crystallized sample (0.8274). The difference in  $\delta\text{ppm}$  in both samples can be caused by the torsional angle between donor and acceptor.

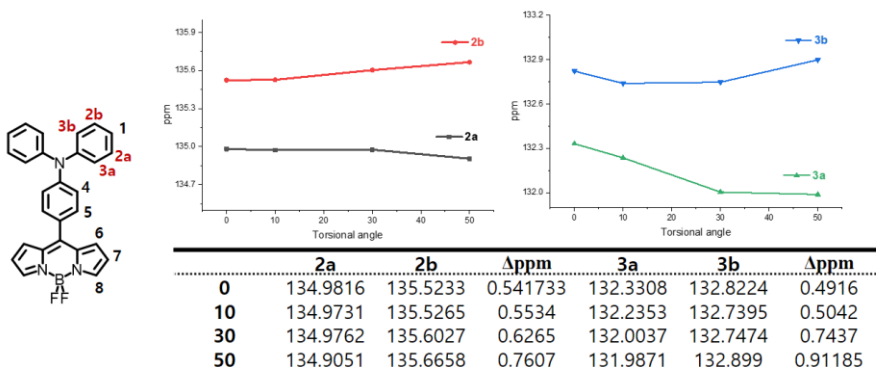


Figure 2.9 A  $^{13}\text{C}$  chemical shift of AM2 obtained from  $^{13}\text{C}$  NMR spectrum using GIAO-DFT method with 6-31G+(2d, p) as the function of the torsional angle.

This data was confirmed by the calculated  $^{13}\text{C}$  NMR data using gauge-invariant atomic orbital (GIAO)/6-311G+(2d,p), B3LYP method (Figure 2.9). The  $\delta$ ppm of C2 and C3 at  $50^\circ$  were 0.76 and 0.91, gradually reduced to 0.54 and 0.49, respectively, as their degrees decreased to  $0^\circ$ , whose trends were identical to the measured NMR spectrum. From the measured and calculated  $^{13}\text{C}$  NMR data, it is apparent that the grinding process reduces the torsional angle between D-A, causing molecular planarization.

The previous section demonstrated that the grinding process induced molecular planarization. It is now necessary to show the

correlation between the molecular planarization and fluorescence properties (MFC). To analyze this, the ICT properties of samples were calculated as a function of the torsional angle (Figure 2.10). The electron density distribution of the AM2 was largely modified depending on the torsional angle. As the torsional angle is 0 °, the electron density of the HOMO is distributed throughout the whole part of the molecules, and that of the LUMO is located not only on the BODIPY (A) but also on the nitrogen part of the TPA (D). On the other hand, as the torsional angle increases, the electron distribution area of the HOMO and LUMO gradually decreases. At 90 degrees, the electrons of HOMO and LUMO are localized only in TPA (D), and BODIPY (A), respectively, which indicates the high torsional angle between donor and acceptor increases charge transfer strength.

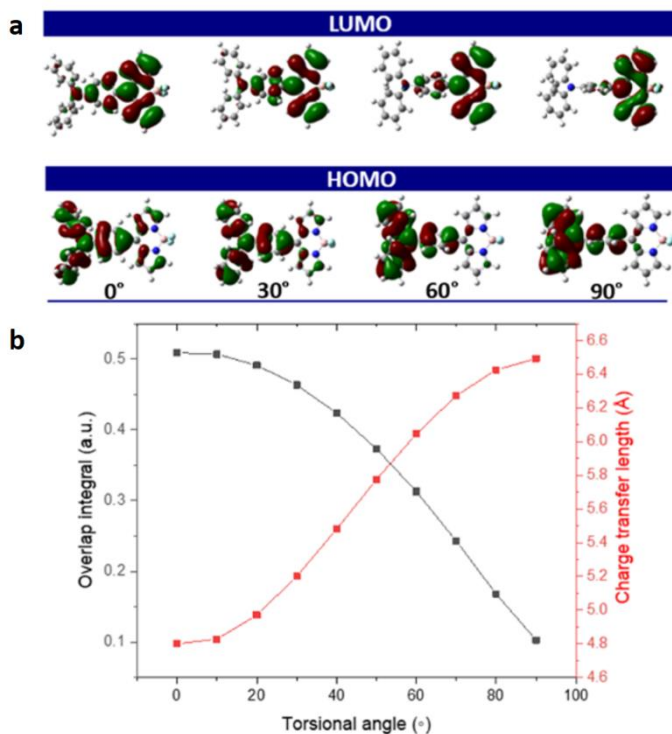
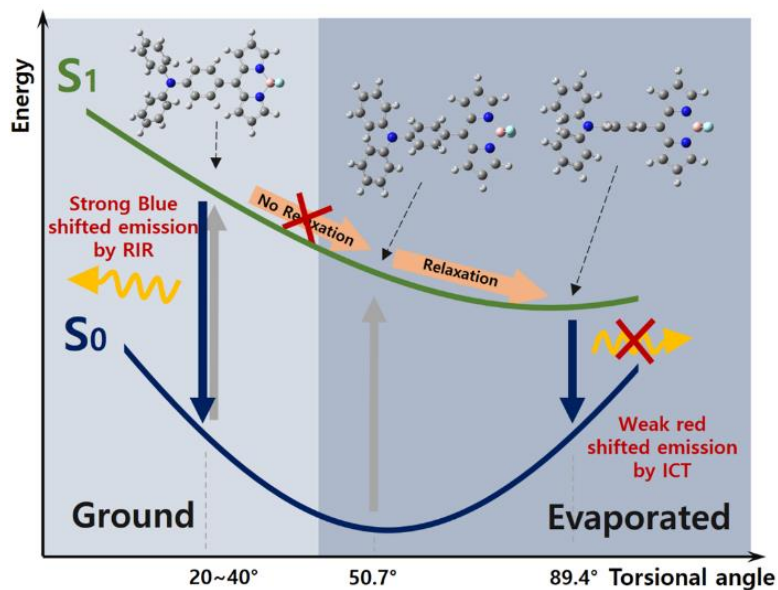


Figure 2.10 (a) electron density distribution of HOMO and LUMO at different torsional angles. (b) Overlap of the integral (black) and charge transfer length (red) of AM2 with increasing torsional angle

To investigate the quantified charge transfer characteristics, the overlap integral and charge transfer length of AM2 were calculated using Multiwfn software (Figure 2.10b). As the torsional angle increased to the 90°, the overlap integral decreases, and the charge transfer length increases, showing that charge transfer strength was gradually enhanced. Given the general accounting

that an increase in the charge transfer strength causes a red-shift, it is concluded that the hypsochromic emission shift of the ground sample was induced by the reduced ICT character.



Scheme 2.2. Excitation dynamics of the evaporated and ground sample

## 2.4 Conclusions

The MFC excitation dynamics of D-A BODIPY dye can be described by Scheme 2.2. The intramolecular rotation of D-A BODIPY dye ground sample is strongly suppressed by the surrounding molecules; further, the dihedral angle between the

donor and the acceptor is so small that the sample is an approximately planarized structure. This rotational restriction induces emission enhancement of molecules because the non-radiative decay channel is suppressed. The planar structure is also maintained during the photoexcitation process owing to the suppression of vibrational relaxation. This results in a relatively weak CT character and therefore causes a hypsochromic emission shift. Evaporated and crystallized samples, on the other hand, can rotate relatively freely owing to their small interactions with surrounding molecules, resulting in fluorescence quenching.

The torsional angle of the crystallized sample between D and A is approximately  $50^\circ$ , which is changed to  $90^\circ$  by the free vibrational relaxation during the photoexcitation process. Molecules with a high torsional angle of  $90^\circ$  show a red-shifted emission and have a smaller fluorescence intensity because they have a high ICT character. This study demonstrated that the MFC is related to RIR and ICT characters using various analysis methods such as ss-NMR and DFT calculations and has provided valuable insight into the structure of molecules with MFC properties. Therefore, the

results of this study will provide a significant contribution in designing future MFC materials including BODIPY

## 2.5 References

- [1] Ooyama Y, Ito G, Fukuoka H, Nagano T, Kagawa Y, Imae I, et al. Mechanofluorochromism of heteropolycyclic donor- $\pi$ -acceptor type fluorescent dyes. *Tetrahedron*. 2010;66(36):7268-71.
- [2] Ooyama Y, Yamaguchi N, Inoue S, Nagano T, Miyazaki E, Fukuoka H, et al. Mechanofluorochromism of carbazole-type D- $\pi$ -A fluorescent dyes. *Tetrahedron*. 2012;68(2):529-33.
- [3] Sharber SA, Mann A, Shih K-C, Mullin WJ, Nieh M-P, Thomas SW. Directed polymorphism and mechanofluorochromism of conjugated materials through weak non-covalent control. *Journal of Materials Chemistry C*. 2019;7(27):8316-24.
- [4] Cao Y, Xi Y, Teng X, Li Y, Yan X, Chen L. Alkoxy substituted D- $\pi$ -A dimethyl-4-pyrone derivatives: aggregation induced emission enhancement, mechanochromic and solvatochromic properties. *Dyes and Pigments*. 2017; 137:75-83.

- [5] Ekbote A, Jadhav T, Misra R. T-Shaped donor–acceptor–donor type tetraphenylethylene substituted quinoxaline derivatives: aggregation-induced emission and mechanochromism. *New Journal of Chemistry*. 2017;41(17):9346-53.
- [6] Gong Y, Tan Y, Liu J, Lu P, Feng C, Yuan WZ, et al. Twisted D– $\pi$ –A solid emitters: efficient emission and high contrast mechanochromism. *Chemical Communications*. 2013;49(38):4009-11.
- [7] Zhao J, Sun J, Simalou O, Wang H, Peng J, Zhai L, et al. multi-stimuli-responsive fluorescent aminostyrylquinoxalines: Synthesis, solvatochromism, mechanofluorochromism and acidochromism. *Dyes and Pigments*. 2018; 151:296-302.
- [8] Cheng D, Xu D, Wang Y, Zhou H, Zhang Y, Liu X, et al. High contrast mechanochromic luminescence of aggregation-induced emission (AIE)-based 9,9-dimethyl-9,10-dihydroacridine-containing cruciform luminophores. *Dyes and Pigments*. 2020; 173:107934.
- [9] Sun J, Dai Y, Ouyang M, Zhang Y, Zhan L, Zhang C. Unique torsional cruciform  $\pi$ -architectures composed of donor and acceptor axes exhibiting mechanochromic and electrochromic properties. *Journal of Materials Chemistry C*. 2015;3(14):3356-63.

- [10] Wang Y, Cheng D, Zhou H, Liu J, Liu X, Cao J, et al. Mechanochromic luminescence of AIEE-active tetraphenylethene-containing cruciform luminophores. *Dyes and Pigments*. 2019; 171:107739.
- [11] Wang Y, Cheng D, Zhou H, Liu X, Wang Y, Han A, et al. Reversible solid-state mechanochromic luminescence originated from aggregation-induced enhanced emission-active Donor–Acceptor cruciform luminophores containing triphenylamine. *Dyes and Pigments*. 2019; 171:107689.
- [12] Arivazhagan C, Maity A, Bakthavachalam K, Jana A, Panigrahi SK, Suresh E, et al. Phenothiazinyl Boranes: A New Class of AIE Luminogens with Mega Stokes Shift, Mechanochromism, and Mechanoluminescence. *Chemistry–A European Journal*. 2017;23(29):7046-51.
- [13] Chen M, Chen R, Shi Y, Wang J, Cheng Y, Li Y, et al. Malonitrile-Functionalized Tetraphenylpyrazine: Aggregation-Induced Emission, Ratiometric Detection of Hydrogen Sulfide, and Mechanochromism. *Advanced Functional Materials*. 2018;28(6):1704689.
- [14] Hariharan P, Venkataramanan N, Moon D, Anthony SP. Self-reversible mechanochromism and thermochromism of a triphenylamine-

based molecule: tunable fluorescence and nanofabrication studies. *The Journal of Physical Chemistry C*. 2015;119(17):9460-9.

[15] Hariharan PS, Mothi EM, Moon D, Anthony SP. Halochromic isoquinoline with mechanochromic triphenylamine: smart fluorescent material for rewritable and self-erasable fluorescent platform. *ACS applied materials & interfaces*. 2016;8(48):33034-42.

[16] Jiang M, Gu X, Kwok RT, Li Y, Sung HH, Zheng X, et al. Multifunctional AIEgens: ready synthesis, tunable emission, mechanochromism, mitochondrial, and bacterial imaging. *Advanced Functional Materials*. 2018;28(1):1704589.

[17] Mizuguchi K, Kageyama H, Nakano H. Mechanochromic luminescence of 4-[bis (4-methylphenyl) amino] benzaldehyde. *Materials Letters*. 2011;65(17-18):2658-61.

[18] Morris WA, Kolpaczynska M, Fraser CL. Effects of  $\alpha$ -substitution on mechanochromic luminescence and aggregation-induced emission of difluoroboron  $\beta$ -diketonate dyes. *The Journal of Physical Chemistry C*. 2016;120(39):22539-48.

[19] Sun J, Han J, Liu Y, Duan Y, Han T, Yuan J. Mechanochromic luminogen with aggregation-induced emission: implications for ink-free

rewritable paper with high fatigue resistance and low toxicity. *Journal of Materials Chemistry C*. 2016;4(35):8276-83.

[20] Wang S, Xiao S, Chen X, Zhang R, Cao Q, Zou K. Crystalline solid responsive to mechanical and acidic stimuli: Boron–fluorine derivative with TICT characteristic. *Dyes and Pigments*. 2013;99(3):543-7.

[21] Wei J, Liang B, Cheng X, Zhang Z, Zhang H, Wang Y. High-contrast and reversible mechanochromic luminescence of a D– $\pi$ –A compound with a twisted molecular conformation. *RSC Advances*. 2015;5(88):71903-10.

[22] Dong YQ, Lam JW, Tang BZ. Mechanochromic Luminescence of Aggregation-Induced Emission Luminogens. *J Phys Chem Lett*. 2015;6(17):3429-36.

[23] Jadhav T, Dhokale B, Mobin SM, Misra R. Aggregation induced emission and mechanochromism in pyrenoimidazoles. *Journal of Materials Chemistry C*. 2015;3(38):9981-8.

[24] Lu Y, Tan Y, Gong Y, Li H, Yuan W, Zhang Y, et al. High efficiency DA structured luminogen with aggregation-induced emission and mechanochromic characteristics. *Chinese Science Bulletin*. 2013;58(22):2719-22.

- [25] Xu B, Chi Z, Zhang J, Zhang X, Li H, Li X, et al. Piezofluorochromic and Aggregation-Induced-Emission Compounds Containing Triphenylethylene and Tetraphenylethylene Moieties. *Chemistry–An Asian Journal*. 2011;6(6):1470-8.
- [26] Zhan Y, Gong P, Yang P, Jin Z, Bao Y, Li Y, et al. Aggregation-induced emission and reversible mechanochromic luminescence of carbazole-based triphenylacrylonitrile derivatives. *RSC Advances*. 2016;6(39):32697-704.
- [27] Boens N, Leen V, Dehaen W. Fluorescent indicators based on BODIPY. *Chemical Society Reviews*. 2012;41(3):1130-72.
- [28] Kamkaew A, Lim SH, Lee HB, Kiew LV, Chung LY, Burgess K. BODIPY dyes in photodynamic therapy. *Chemical Society Reviews*. 2013;42(1):77-88.
- [29] Ulrich G, Ziessel R, Harriman A. The chemistry of fluorescent bodipy dyes: versatility unsurpassed. *Angewandte Chemie International Edition*. 2008;47(7):1184-201.
- [30] Ziessel R, Ulrich G, Harriman A. The chemistry of Bodipy: a new El Dorado for fluorescence tools. *New Journal of Chemistry*. 2007;31(4):496-501.

- [31] Duan C, Zhou Y, Shan G-G, Chen Y, Zhao W, Yuan D, et al. Bright solid-state red-emissive BODIPYs: facile synthesis and their high-contrast mechanochromic properties. *Journal of Materials Chemistry C*. 2019;7(12):3471-8.
- [32] Liu Y, Duan J, Qi F, Tian D, Wang X, Liu Z, et al. Optical properties and mechanofluorochromism of new BODIPY dyes based on the pyridine–pyrimidine hybrid structure. *Dalton Transactions*. 2017;46(31):10332-8.
- [33] Ooyama Y, Hagiwara Y, Oda Y, Fukuoka H, Ohshita J. BODIPY dye possessing solid-state red fluorescence and green metallic luster properties in both crystalline and amorphous states. *RSC Advances*. 2014;4(3):1163-7.
- [34] Gao Y, Qu Y, Jiang T, Zhang H, He N, Li B, et al. Alkyl-triphenylamine end-capped triazines with AIE and large two-photon absorption cross-sections for bioimaging. *Journal of Materials Chemistry C*. 2014;2(31):6353-61.
- [35] Huang J, Jiang Y, Yang J, Tang R, Xie N, Li Q, et al. Construction of efficient blue AIE emitters with triphenylamine and TPE moieties for non-doped OLEDs. *Journal of Materials Chemistry C*. 2014;2(11):2028-36.

- [36] Liu Y, Kong M, Zhang Q, Zhang Z, Zhou H, Zhang S, et al. A series of triphenylamine-based two-photon absorbing materials with AIE property for biological imaging. *Journal of Materials Chemistry B*. 2014;2(33):5430-40.
- [37] Padalkar VS, Sakamaki D, Kuwada K, Tohnai N, Akutagawa T, Sakai K-i, et al. AIE active triphenylamine–benzothiazole based motifs: ESIPT or ICT emission. *RSC Advances*. 2016;6(32):26941-9.
- [38] Bañuelos J, Arroyo-Córdoba IJ, Valois-Escamilla I, Alvarez-Hernández A, Peña-Cabrera E, Hu R, et al. Modulation of the photophysical properties of BODIPY dyes by substitution at their meso position. *RSC Advances*. 2011;1(4):677-84.
- [39] Hu D, Zhang T, Li S, Yu T, Zhang X, Hu R, et al. Ultrasensitive reversible chromophore reaction of BODIPY functions as high ratio double turn on probe. *Nature Communications*. 2018;9(1):362.
- [40] Hu R, Lager E, Aguilar-Aguilar A, Liu J, Lam JWY, Sung HHY, et al. Twisted Intramolecular Charge Transfer and Aggregation-Induced Emission of BODIPY Derivatives. *The Journal of Physical Chemistry C*. 2009;113(36):15845-53.
- [41] Levine Y, Partington P, Roberts G. Calculation of dipolar nuclear magnetic relaxation times in molecules with multiple internal rotations: I.

Isotropic overall motion of the molecule. *Molecular Physics*. 1973;25(3):497-514.

[42] Lubach JW, Xu D, Segmuller BE, Munson EJ. Investigation of the effects of pharmaceutical processing upon solid-state NMR relaxation times and implications to solid-state formulation stability. *Journal of pharmaceutical sciences*. 2007;96(4):777-87.

[43] Ou H, Li J, Chen C, Gao H, Xue X, Ding D. Organic/polymer photothermal nanoagents for photoacoustic imaging and photothermal therapy in vivo. *Science China Materials*. 2019:1-19.

[44] Tokumaru K, Jin B, Yoshida S, Takanishi Y, Ishikawa K, Takezoe H, et al. Molecular rotation in an antiferroelectric liquid crystal studied by <sup>13</sup>C-nuclear magnetic resonance spin-lattice relaxation time measurement. *Japanese journal of applied physics*. 1999;38(1R):147.

[45] Zhao Z, Chen C, Wu W, Wang F, Du L, Zhang X, et al. Highly efficient photothermal nanoagent achieved by harvesting energy via excited-state intramolecular motion within nanoparticles. *Nature communications*. 2019;10(1):768.

[46] Ramachandran E, Dhamodharan R. Tetrakis(trialkylsilylethynylphenyl)ethenes: mechanofluorochromism

arising from steric considerations with an unusual crystal structure. *J*

*Mater Chem C.* 2017;5(40):10469-76.

[47] SMART, SAINT and SADABS, Bruker AXS Inc., Madison, Wisconsin, USA, 2012.

[48] G. M. Sheldrick, SADABS v 2.03, University of Göttingen, Germany, 2002.

[49] SHELXTL v 6.10; Bruker AXS, Inc: Madison, Wisconsin, USA, 2000.

[50] Tian Lu, Feiwu Chen, Multiwfn: A Multifunctional Wavefunction Analyzer, *J. Comput. Chem.* **33**, 580-592 (2012)

## **Chapter 3**

# **A study on photophysical and photodynamic properties of donor–acceptor BODIPY complexes: Correlation between singlet oxygen quantum yield and singlet-triplet energy gap**

### **3.1 Introductions**

Recent trends in photodynamic therapy (PDT) have led to the development of non-porphyrin photosensitizers (PSs) because conventional porphyrin-based PSs have major drawbacks such as dark toxicity (e.g., Purlytin), long-lasting photosensitivity (e.g., Photofrin, Foscan, and Purlytin), and severe pain to patients during irradiation (e.g., Levulan and Metvix). [1-14] Among non-porphyrin PSs, the main focus was on heavy-atom-based PSs, which generate reactive oxygen species by spin-orbit coupling. [1-3] However, although heavy-atom-based PSs afforded high singlet oxygen quantum yield (SOQY), they

exhibited severe side effects such as high dark toxicity. [15] Therefore, the development of novel heavy-atom-free photosensitizers is required. Recently, donor–acceptor (D–A) PSs based on BODIPY have been garnering increasing interest because D–A PSs can potentially increase the intersystem crossing (ISC) rate and SOQY without the use of a heavy atom. [10-13, 15] There are two possible explanations for the ISC mechanism of D–A PSs: (1) the hyperfine coupling ISC (HFC-ISC) between the singlet charge transfer state ( $^1\text{CT}$ ) and triplet charge transfer state ( $^3\text{CT}$ ), and (2) the spin-orbit charge transfer ISC (SOCT-ISC) between the  $^1\text{CT}$  and triplet locally excited state ( $^3\text{LE}$ ). Although the detailed mechanism of ISC in D–A PSs is still controversial, it has been generally accepted that SOCT is the predominant factor for the increased ISC in D–A PSs, because the  $^1\text{CT}$  to  $^3\text{CT}$  transition of HFC is forbidden because of the high electron exchange energy ( $J$ ) and small coupling matrix elements induced by the same spatial distribution of molecular orbitals in both states. [13, 16-18]

Several studies have reported that reducing the energy gap between  $^1\text{CT}$  and  $^3\text{LE}$  can increase the triplet quantum yield, thereby increasing SOQY. [16, 19, 20] To verify this, most studies compared the SOQY or triplet quantum yield with the energy gap, which was controlled by the

solvent polarity. However, because of the modification in solvent polarity change factors such as saturated oxygen concentration, oxygen diffusivity, and dye diffusivity, as well as  $\Delta E_{ST}$ , it could be less reliable to compare  $\Delta E_{ST}$  and SOQY. Most of the triplet quantum yields are measured using the triplet-triplet annihilation fluorescence method, and this might not be the ideal comparison under strictly controlled conditions because the diffusivities of the triplet donor and annihilator are different for each solvent. Nevertheless, to the best of our knowledge, no studies have thus far investigated the impact of  $\Delta E_{ST}$  on SOQY (or triplet yield) under controlled conditions. Although some studies have examined the SOQY of the sensitizers according to the electron-donating power control under the same conditions, these were not directly explained by  $\Delta E_{ST}$ .

Here, to examine the correlation between  $\Delta E_{ST}$  and the SOQY under identical conditions, we prepared D-A photosensitizers comprising triphenylamine (TPA, donor) and boron-dipyrromethene (BODIPY, acceptor). For these cases, highly polar solvents were excluded because of the unique characteristics of the  $^1CT$  state in D-A photosensitizers. In general, the  $^1CT$  state is known as a dark state; thus, nonradiative transition ( $^1CT \rightarrow S_0$ ) occurs rapidly in highly polar solvents.

As a result, the SOQY as well as  $\Delta E_{ST}$  can be affected by the transition of  $^1CT \rightarrow S_0$ . Therefore, low-polarity toluene was selected for imposing identical conditions to avoid nonradiative decay. BODIPY was selected as an acceptor because of its excellent photophysical properties such as high absorption coefficient, fluorescence quantum yield, and low dark toxicity. In addition, the properties of BODIPY can be efficiently controlled via structural modifications at several positions. Therefore, D-A based BODIPY are promising candidates for use as triplet photosensitizers.

## **3.2 Experimental**

### **3.2.1 Materials**

All of the commercial reagents were purchased from Sigma-Aldrich or Tokyo Chemical Industry (TCI) and used without further purification. Anhydrous solvents used in the reactions were purchased from Sigma-Aldrich or Alfa aesar.

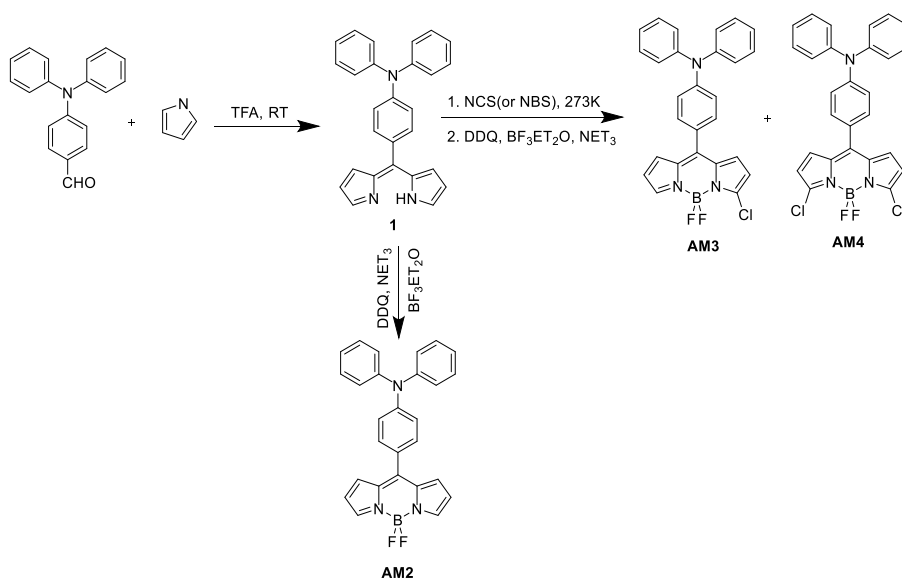
### **3.2.2 Instruments**

$^1H$  NMR spectra were recorded on a Bruker Avance 500 spectrometer

(National Center for Inter-University Research Facilities at Seoul National University) at 500 MHz using dimethyl sulfoxide-d<sub>6</sub>, chloroform-d with tetramethylsilane (TMS). Low resolution mass experiments were operated on a Q-TOF 5600 mass spectrometer equipped with an ESI source (National Instrumentation Center for Environmental Management). Research Facilities at Seoul National University). Solvatochromic absorption and fluorescence solutions were measured by an UV-vis spectrophotometer (LAMBDA 25, Perkin Elmer Co.) and a fluorescence spectrometer (LS-55, Perkin Elmer Co.), respectively. Phosphorescence spectra of solutions were conducted at 77 K (the liquid nitrogen temperature) by the fluorescence spectrometer (LS-55, Perkin Elmer Co.). A 1 ms delay time was inserted between the pulsed excitation and the collection of the emission spectrum (gate time: 1ms, cycle: 16, flash counts: 1). Time-resolved photoluminescence decay of 10  $\mu$ M photosensitizers solutions were measured with a fluorophotometer (fluorolog3, HORIBA SCIENTIFIC) by irradiation of a laser ( $\lambda$  = 467 nm). Photoluminescence (PLQY) of 10  $\mu$ M photosensitizers solutions were estimated using an integrating sphere (QE-1100, Otsuka electronics Co.). Singlet oxygen quantum yield (SOQY) measurements in all solvents were carried out by using the

indirect method. (standard: 2,3,7,8-tetrabromo-5,5-difluoro-10-phenyl-5H-4(1,5(14)-dipyrrolo[1,2-c:2',1'-f][1,3,2]diazaborinine,  $\Phi_{\Delta} = 0.49$ ). [27] Oxygen was bubbled into the solvents for 30min before sample preparation. All samples in 3.5ml solvents contained diphenylisobenzofuran (DPBF) were irradiated with laser (505nm. 5mW  $\pm 3\%$ ). The concentration of DPBF was fixed to 30mM for preventing from chain reaction. The ground-state geometry was optimized with Gaussian 16 software using the B3LYP hybrid functional and the 6-31G (d, p) basis set.

### 3.2.3 Synthesis



### Scheme 3.1 Synthesis of the photosensitizers (AM1-AM4)

#### 3.2.3.1 Preparation of compound 1 (4-(di(1H-pyrrol-2-yl)methyl)-N,N-diphenylaniline)

In three neck round bottom flask, 4-(Diphenylamino) benzaldehyde (1.05g, 3.85 mmol) and pyrrole (1.033g, 15.4 mmol, 4eqn) were dissolved into dry dichloromethane (250 mL), then a solution of trifluoroacetic acid (0.5 mmol, 0.13eqn) in dry dichloromethane (2.5 mL) were slowly added to the mixture at room temperature under N<sub>2</sub> atmosphere. Then the reaction mixture was quenched by 2mL, trimethylamine and evaporated. The brown, oily residue is simply purified by column chromatography on silica with CH<sub>2</sub>Cl<sub>2</sub>: n-hexane = 1:1 to produce 1 as brown solid (1.47g).

#### 3.2.3.2 Preparation of compound AM1

**AM1** were prepared according to the literature procedure. (yield 6%) **<sup>1</sup>H NMR** (500 MHz, CDCl<sub>3</sub>) δ 7.87 (s, 2H), 7.57-7.40 (m, 5H), 6.86 (d, J=4.0Hz, 2H), 6.47 (d, J=4.0Hz, 2H), **<sup>13</sup>C NMR** (500 MHz, CDCl<sub>3</sub>) δ 147.6, 144.3, 135.2, 134.0, 131.8, 131.0, 130.7, 128.6, 118.7 **HRMS**

(M+H<sup>+</sup>) Calcd for C<sub>15</sub>H<sub>11</sub>BF<sub>2</sub>N<sub>2</sub>: 269.1056. Found: 269.1049

### 3.2.3.3 Preparation of compound AM2

After 3 h, 2,3-Dichloro-5,6-dicyano-1,4-benzoquinone (DDQ) (0.87 g, 3.85 mmol) was added to the crude mixture of **1** (700mg) under ice bath cooling and stirred for 10 min. The solution is stirred for an additional 1 h at room temperature. Triethylamine (55.44 mmol, 14.5eqn) is added, followed by slow addition of BF<sub>3</sub> Et<sub>2</sub>O (62.37 mmol, 16.2eqn). After 2 h, the reaction mixture was washed at room temperature with saturated aqueous Na<sub>2</sub>CO<sub>3</sub> solution (3 x 100 mL), dried over MgSO<sub>4</sub>, and concentrated on a rotary evaporator. The brown, oily residue is purified by column chromatography on silica with CH<sub>2</sub>Cl<sub>2</sub>: n-hexane = 2:1 to produce AM2 as red-brown solid. (250 mg, 13% yield). **<sup>1</sup>H NMR** (500 MHz, CDCl<sub>3</sub>) δ 7.90 (s, 2H), 7.49-7.44 (d, J=8.7Hz, 2H), 7.39-7.32 (t, J=7.5Hz, 4H), 7.25-7.00 (d, J=7.5Hz, 4H), 7.19-7.13 (t, J=7.4Hz, 2H), 7.13-7.08 (d, J=8.6Hz, 2H), 7.08-7.04 (d, J=4.0Hz, 2H), 6.5 (m, 2H) **<sup>13</sup>C NMR** (500 MHz, CDCl<sub>3</sub>) δ 151.1, 147.7, 146.6, 142.9, 134.8, 132.5, 131.3, 129.9, 126.4, 126.1, 124.9, 120.2, 118.2; **HRMS-ESI** (M+H<sup>+</sup>) Calcd for C<sub>27</sub>H<sub>21</sub>BF<sub>2</sub>N<sub>3</sub>: 436.1796. Found: 436.1772

### 3.2.3.4 Preparation of compound **AM3** and **AM4**

In a three-neck flask, a crude mixture of compound **1** (779 mg, 2 mmol) was dissolved into dry THF (40 mL) and the mixture was cooled to -78 °C under nitrogen atmosphere. N-Chlorosuccinimide, (588 mg, 4.4 mmol) was slowly added over 30 min. After 2 h, 2,3-Dichloro-5,6-dicyano-1,4-benzoquinone, DDQ (454 mg, 2 mmol) in 7 mL dry THF was added dropwise over 10 min at same temperature. Then the reaction temperature was increased to RT and the solvent was distilled on rotary evaporator. Then the crude compound was dissolved in 50 mL dichloromethane, neutralized with triethylamine (9.73 mL, 70 mmol) and treated with BF<sub>3</sub>.Et<sub>2</sub>O (12.5 mL, 99.5 mmol) at room temperature for additional 2-3 h. The reaction mixture was quenched with 20 mL 0.1 M NaOH solution and extract from water. The organic layer was dried over MgSO<sub>4</sub>, filtered, and evaporated. The crude product was purified by silica gel column chromatography eluting with hexane/dichlorometane (95:5) to produce compound **AM3**(41mg ,4.5% yield) **AM4** as red colour solid (89mg, 9.2% yield).

**AM3: 1H NMR** (500 MHz, CDCl<sub>3</sub>) δ 7.85 (s, 2H), 7.39-7.31 (d, J=7.3Hz, 2H), 7.31-7.25 (t, J=7.0Hz, 4H), 7.16-7.13 (d, J=6.3Hz, 4H),

7.12-7.08 (t, J=6.2Hz, 2H), 7.05-7.00 (d, J=7.3Hz, 2H), 6.98-6.92 (m, J=4.0Hz, 2H), 6.50 (m, 1H), 6.36 (d, J=3.6Hz, 1H), **<sup>13</sup>C NMR** (500 MHz, CDCl<sub>3</sub>) δ 151.0, 146.4, 145.9, 143.2, 143.0, 134.3, 133.7, 132.2, 131.3, 131.0, 129.7 126.0, 125.4, 124.8, 120.0, 118.4; 117.8 HRMS-ESI (M+H<sup>+</sup>) Calcd for C<sub>27</sub>H<sub>20</sub>BClF<sub>2</sub>N<sub>3</sub>: 470.1407. Found: 470.1381 **AM4: <sup>1</sup>H NMR** (500 MHz, CDCl<sub>3</sub>) δ 7.95 (s, 1H), 7.73 (s, 1H), 7.47-7.42 (d, J=7.4Hz, 2H), 7.40-7.36 (t, J=7.1Hz, 4H), 7.26-7.22 (dd, J=6.2Hz, 4H), 7.22-7.17 (t, J=6.2Hz, 2H), 7.14-7.12 (d, J=3.7Hz, 1H), 7.12-7.08 (d, J=7.4Hz, 2H), 6.92 (s, 1H), 6.60 (dd, J=3.5Hz, 1H), **<sup>13</sup>C NMR** (500 MHz, CDCl<sub>3</sub>) δ 151.4, 146.2, 144.5, 138.6, 132.4, 129.8, 126.8, 126.1, 126.0, 125.5, 125.0 119.8 HRMS-ESI (M+H<sup>+</sup>) Calcd for C<sub>27</sub>H<sub>19</sub>BCl<sub>2</sub>F<sub>2</sub>N<sub>3</sub>: 504.1017. Found: 504.1008

### **3.2.4 Determination of onsager cavity radius for molecules [28, 29]**

The estimation of van der Waals volume ( $V_{vdw}$ ) for the molecules was done theoretically using the atomic and bond contributions of  $V_{vdw}$ . According to Abraham and co-workers, the van der Waals volume ( $\text{\AA}^3$  /molecule) can be calculated from the following formula:

$$V_{vdw} = \sum (\text{all atom contributions}) - 5.92N_B - 14.7R_A - 3.8R_{NA}$$

where,  $N_B$  is the number of bonds,  $R_A$  is the number of aromatic rings, and  $R_{NA}$  is the number of non-romantic rings. If the total number of atoms in the molecule is  $N$ , then the number of bonds present ( $N_B$ ) can be calculated using the relation:

$$N_B = N - 1 + R_A + R_{NA}$$

The van der Waals volumes ( $V_{vdw}$ ) for carbon, hydrogen, boron, fluorine, nitrogen, and chlorine are considered to be as 20.58, 7.24, 40.48, 13.31, 15.6 and 22.45Å respectively. For example, the molecular formula of AM2 is:  $C_{28}H_{22}BF_2N_3S$ . Thus, the sum of all atom contribution for each of these molecules turns out to be:

$$\begin{aligned} \sum (\text{all atom contributions}) &= (27 \times 20.58) + (20 \times 7.24) + (1 \times 40.48) \\ &+ (2 \times 13.31) \\ &+ (3 \times 15.6) = 555.66 + 144.8 + 40.48 + 26.62 + 46.8 \\ &= 814.36 \end{aligned}$$

The number of bonds present in AM2 can be calculated as:

$$\begin{aligned} N_B &= N - 1 + R_A + R_{NA} \\ &= 53 - 1 + 6 + 0 \end{aligned}$$

$$= 58$$

Thus, the calculated van der Waals volumes ( $V_{vdw}$  in  $\text{\AA}^3$ ) for should be given by:

$$\begin{aligned} V_{vdw} &= \sum (\text{all atom contributions}) - 5.92N_B - 14.7R_A - 3.8R_{NA} \\ &= 814.36 - (5.92 \times 58) - (14.72 \times 6) - (3.8 \times 0) \\ &= 814.36 - 343.36 - 88.32 \\ &= 382.72 \end{aligned}$$

Now, if we consider the Onsager radius to be 'a' (in  $\text{\AA}$ ) for a spherical molecule, then the van der Waals volume ( $V_{vdw}$  in  $\text{\AA}^3$ ) can be regarded as,

$$V_{vdw} = \frac{4}{3}\pi a^3$$

Thus, for a molecule such as AM1, the relation turns out to be,

$$\frac{4}{3}\pi a^3 = 382.72$$

$$\text{i.e. } a^3 = 91.37$$

$$\text{Thus, } a = 4.50 \text{ \AA}$$

Table 3.1 Parameters for determination of onsager cavity radius for molecules

|  | AM2 | AM3 | AM4 |
|--|-----|-----|-----|
|--|-----|-----|-----|

| Molecular Formula                      | C <sub>27</sub> H <sub>20</sub> BF <sub>2</sub> N <sub>3</sub> | C <sub>27</sub> H <sub>19</sub> BClF <sub>2</sub> N <sub>3</sub> | C <sub>27</sub> H <sub>18</sub> BCl <sub>2</sub> F <sub>2</sub> N <sub>3</sub> |
|--|--|--|--|
| Σ (all atom contributions)             | 814.36   | 829.57   | 844.78   |
| N <sub>B</sub>                         | 58   | 58   | 58   |
| Van der Waals volume (Å <sup>3</sup> ) | 382.72   | 398.01   | 413.22   |
| Onsager cavity radius (Å)              | 4.50   | 4.56   | 4.62   |

### 3.2.5 Femtosecond Transient Absorption and Transient Absorption Anisotropy Analysis

Dual-beam femtosecond time-resolved transient absorption (TA) spectrometer consisted of two independently-tunable home-made noncollinear optical parametric amplifiers (NOPA) pumped by a regeneratively amplified Ti: sapphire laser system (Spectra-Physics, Hurricane-X) operating at 3 kHz repetition rate and an optical detection system. The NOPA was based on non-collinearly phase-matching geometry, which was easily color-tuned by controlling optical delay between white light continuum seed pulses (450-1400 nm) and visible pump pulses (400 nm) produced by using a sapphire window and BBO crystal, respectively. The generated visible OPA pulses had a pulse

width of  $\sim 35$  fs and an average power of 10 mW at 3 kHz repetition rate in the range 500-700 nm after a fused-silica prism compressor. Two OPA pulses were used as the pump and probe pulses, respectively, for TA measurement. The probe beam was split into two parts. The one part of the probe beam was overlapped with the pump beam at the sample to monitor the transient (signal), while the other part of the probe beam was passed through the sample without overlapping the pump beam to compensate the fluctuation of probe beam. The time delay between pump and probe beams was carefully controlled by making the pump beam travel along a variable optical delay (Newport, ILS250). To obtain the time-resolved transient absorption difference signal at specific wavelength, the monitoring wavelength was selected by using a narrow interference filter (FWHM  $\sim 10$  nm). By chopping the pump pulses at 47 Hz, the modulated probe pulses as well as the reference pulses were detected by two separate photodiodes (New Focus, Femtowatt Photoreceiver). The modulated signals of the probe pulses were measured by a gated-integrator (SRS, SR250) and a lock-in amplifier (EG&G, DSP7265) and stored in a personal computer for further signal processing. In general, experimental conditions, time-resolutions of less than 50 fs were achieved. For transient absorption anisotropy (TAA)

measurement, both  $I_{//}(t)$  and  $I_{\perp}(t)$  signals were collected simultaneously by combination of polarizing beam-splitter cube and dual lock-in amplifiers as following equation: [30]

$$r(t) = [I_{//}(t) - I_{\perp}(t)] / [I_{//} + 2I_{\perp}(t)]$$

where  $I_{//}(t)$  and  $I_{\perp}(t)$  represent TA signals with the polarization of the pump and probe pulses being mutually parallel and perpendicular, respectively. The pump pulses were set to vertical polarization and that of probe pulse was set to  $45^{\circ}$  with respect to the pump pulse by using Glan-laser polarizers and half-wave plates. After the probe pulse passes through the sample cell, it was split by polarizing beam-splitter cube and then detected by two separate photodiodes. Two gated-integrators and two lock-in amplifiers record the signal simultaneously within a single scan. As a standard anisotropy measurement showed a clean single exponential decay with reorientational relaxation times of  $122.1 \pm 0.3$  ps and the initial anisotropy  $r_0$  value of  $0.39 \pm 0.02$  for rhodamine 6G dye in methanol, which are well-matched with other references. For all TAA measurements, a thin absorption cell with a path length of 0.5 mm was used to eliminate additional chirping.

### **3.2.6 Nanoseconds transient absorption spectroscopy**

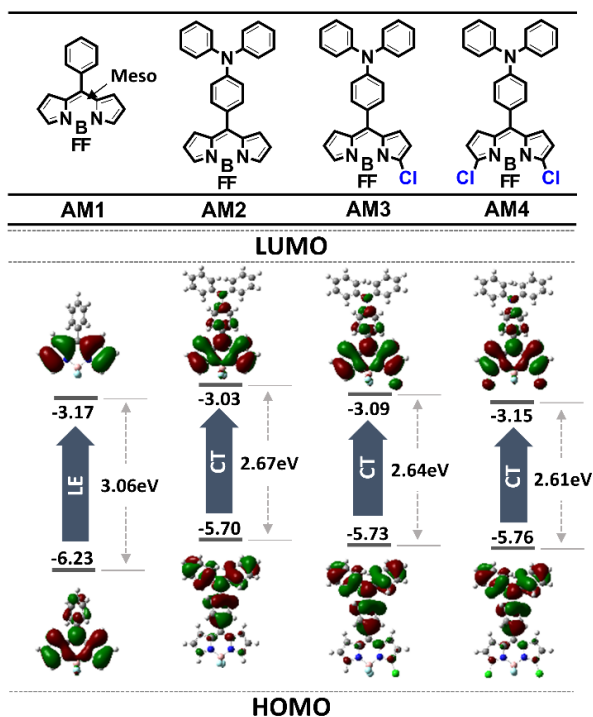
Nanosecond TA spectra were obtained using nanosecond flash photolysis. Specifically, a tunable excitation pulse was generated using an optical parametric oscillator system (Continuum, Surelite OPO) that was pumped with 355 nm light from the third-harmonic output of a Q-switched Nd: YAG laser (Continuum, Surelite II-10). The duration of the excitation pulse was ca. 6 ns, and the pulse energy was ca. 2 mJ/pulse. A CW Xe lamp (150 W) was used as the probe light source for the TA measurement. The probe light was collimated at the sample cell and was spectrally resolved using a 15 cm monochromator (Acton Research, SP150) equipped with a 600 grooves/mm grating after the light passed the sample. The spectral resolution was approximately 3 nm for the TA experiment. The light signal was detected using an avalanche photodiode (APD). The output signal from the APD was recorded using a 500 MHz digital storage oscilloscope (Lecroy, WaveRunner 6050A) for temporal profile measurement. Since the triplet-state dynamics of molecules in solution are strongly dependent on the dissolved oxygen concentration, we attempted to remove oxygen by bubbling with Ar gas for 30 min.

## 3.3 Results and discussion

### 3.3.1 Molecular design

To systematically investigate the correlation between  $\Delta E_{ST}$  and SOQY, a strategy to control  $\Delta E_{ST}$  is required. The introduction of a strong electron-donating (or accepting) group in the D–A complex reduces  $\Delta E_{ST}$  and elicits large charge separation between the donor and acceptor.

Herein, the electron-accepting strength of the D–A complex was modulated by introducing different numbers of chlorine (Cl) atoms (AM2(2H)<AM3(1Cl)<AM4(2Cl)). Benzene-introduced BODIPY was used as a standard for the comparison of CT effects, because the electron-donating power of benzene is weak, unlike that of TPA. The synthesized organic dyes (AM1-4) and their calculated spatial distributions of the HOMO and LUMO energy densities are shown in Scheme 3.2.



Scheme 3.2. Molecular structures of BODIPY photosensitizers (AM1–AM4) and frontier molecular orbitals including the transition type.

Steric hindrance between TPA and BODIPY results in a D–A torsional angle (AM2: 51.5°, AM3: 52.3°, and AM4: 52.4°), leading to spatial charge separation in the HOMO and LUMO. The HOMOs of AM2–4 are mainly localized over the TPA moiety, while the LUMOs are mainly localized on the BODIPY moiety, indicating the strong CT character of AM2–4. In contrast, the HOMO and LUMO of AM1 are spatially localized on the BODIPY moiety, indicating the locally excited character

of AM1, which occurs because the benzene moiety cannot transfer charge from donor to acceptor owing to its weak electron-donating power, even though it exhibits a large torsional angle ( $57.7^\circ$ ).

### 3.3.2 Optical properties.

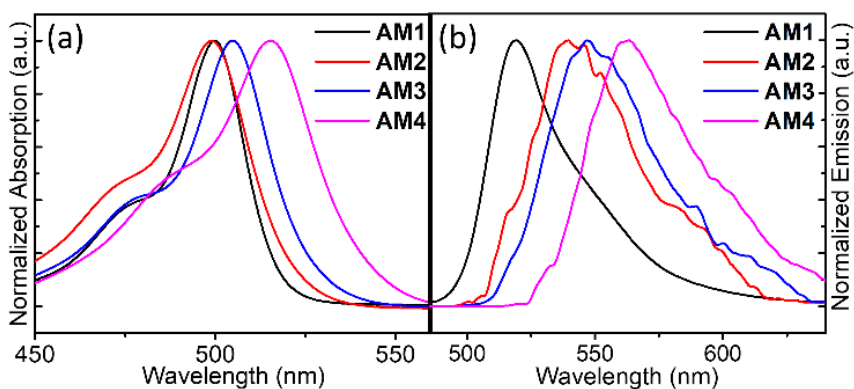


Figure 3.1. (a) Normalized UV-VIS absorption and (b) Normalized emission spectra of the photosensitizers in hexane solution.

Figure 3.1 shows the normalized absorption and emission spectra of the AM1-4 photosensitizers, measured in dilute n-hexane (HEX) ( $10^{-5}$  M). The absorption maxima of AM1 and AM2 were nearly identical, supporting that substitution at *meso*- position on BODIPY has no influence on the absorption spectrum. [21] The increase in electron-accepting power in going from AM2 to AM4 led to a bathochromic shift

of the absorption and emission spectra, indicating that the energy required for absorption and emission is diminished. These results can be confirmed by the calculated HOMO–LUMO energy gaps (Scheme 3.2). The increased accepting power reduces the HOMO and LUMO energy levels and the energy gap between them was decreased, since the magnitude of the decrease in LUMO was larger than that in HOMO. This trend can be explained by the fact that withdrawing groups induce conjugated molecules to more readily accept an electron, thereby, lowering the LUMO effectively. [22] Thus, a strategy to introduce a different number of chlorines into the D–A complex was efficient for controlling the electron-accepting power, as intended.

### **3.3.3 Solvatochromic properties.**

Based on the DFT calculation and steady-state measurement results, absorption and emission spectra of the AM1–4 photosensitizers were normalized in different solvents (Figure 3.2). While the absorption maxima of the AM2–4 photosensitizers, which exhibited a nearly constant wavelength peak regardless of solvent polarity, the emission maxima were bathochromically shifted as the solvent polarity increased.

In addition, the fluorescence quantum yield decreased as the solvent polarity increased (Table 3.2). The large bathochromic shift of the emission spectra and the fluorescence quenching in polar solvents indicate that the AM2–4 photosensitizers show a strong CT character due to the lowered excited singlet state by stabilization through surrounding polar solvent molecules.

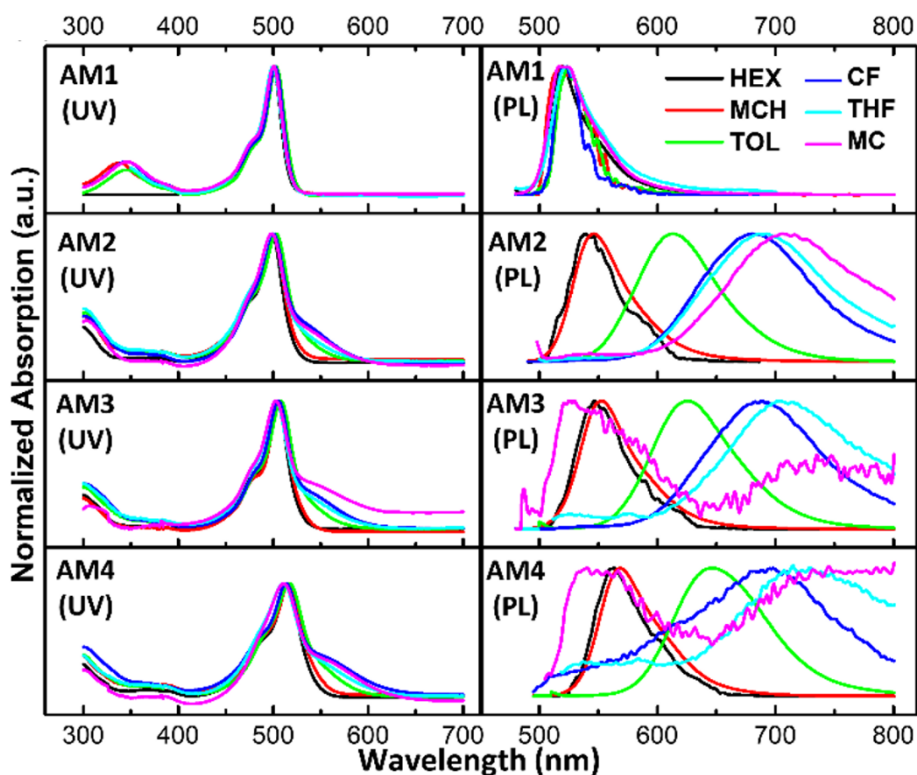


Figure 3.2 Normalized UV-VIS absorption and emission spectra of the photosensitizers ( $10^{-5}$  M)

Table 3.2 Absorption and emission maximum wavelength, photophysical properties of photosensitizers in five different solvents. (HX: n-hexane, MCH: methyl cyclohexane, TOL: toluene, CF: chloroform, THF: tetrahydrofuran, MC: methylene chloride)

| Solvents | $\lambda_{\text{abs}}$ | $\lambda_{\text{emi}}$ | $\Delta f$ | $\Phi_F$ | $\tau$ | $k_r+k_{nr}$       | $k_r$              | $k_{nr}$           |       |
|----------|------------------------|------------------------|------------|----------|--------|--------------------|--------------------|--------------------|-------|
|          | [nm]                   | [nm]                   | [nm]       |          | [ns]   | [10 <sup>9</sup> ] | [10 <sup>9</sup> ] | [10 <sup>9</sup> ] |       |
| AM2      | HX                     | 499                    | 540        | 41       | 0.34   | 0.993              | 1.007              | 0.342              | 0.665 |
|          | MCH                    | 500                    | 546        | 46       | 0.12   | 1.413              | 0.708              | 0.085              | 0.623 |
|          | TOL                    | 503                    | 614        | 111      | 0.32   | 4.322              | 0.231              | 0.074              | 0.157 |
|          | CF                     | 500                    | 680        | 180      | 0.11   | 3.18               | 0.314              | 0.035              | 0.280 |
|          | THF                    | 499                    | 693        | 194      | 0.03   | 0.95               | 1.053              | 0.032              | 1.021 |
|          | MC                     | 498                    | 706        | 208      | 0.01   | - <sup>a</sup>     | -                  | -                  | -     |
| AM3      | HX                     | 505                    | 547        | 42       | 0.22   | 1.82               | 0.549              | 0.121              | 0.429 |
|          | MCH                    | 506                    | 553        | 47       | 0.197  | 2.543              | 0.393              | 0.077              | 0.316 |
|          | TOL                    | 508                    | 627        | 119      | 0.33   | 4.528              | 0.221              | 0.073              | 0.148 |
|          | CF                     | 505                    | 689        | 184      | 0.1    | 3.23               | 0.310              | 0.031              | 0.279 |
|          | THF                    | 503                    | 705        | 202      | 0.02   | 0.45               | 2.222              | 0.044              | 2.178 |
|          | MC                     |                        |            |          | 0.01   | - <sup>a</sup>     | -                  | -                  | -     |
| AM4      | HX                     | 515                    | 563        | 48       | 0.26   | 2.65               | 0.377              | 0.098              | 0.279 |
|          | MCH                    | 516                    | 569        | 53       | 0.124  | 3.161              | 0.316              | 0.039              | 0.277 |
|          | TOL                    | 517                    | 648        | 131      | 0.32   | 4.239              | 0.236              | 0.075              | 0.160 |
|          | CF                     | 513                    | 689        | 176      | 0.03   | 1.54               | 0.649              | 0.019              | 0.630 |
|          | THF                    | 511                    | 715        | 204      | 0.03   | 0.16               | 6.250              | 0.188              | 6.063 |

MC 0.01 -<sup>a</sup> - - -

---

<sup>a</sup>Singlet state lifetime of AM2-4 photosensitizers were not observed.

In contrast, both the absorption and emission maxima of the AM1 photosensitizer were at a nearly constant wavelength regardless of the solvent polarity, indicating a local excitation (LE) character instead of the CT character. The mirror image relationship between the absorption and emission spectra of the AM2–4 photosensitizers in nonpolar solvents such as HEX and methyl-cyclohexane (MCH) was observed.

The emission of these photosensitizers in nonpolar solvents may be assigned to the singlet locally excited (<sup>1</sup>LE) band from the singlet locally excited state. The emission spectra in polar solvents such as toluene (TOL), chloroform (CF), tetrahydrofuran (THF), and di-chloromethane (MC) were broad and shapeless, implying that the emission band of AM2-4 in polar solvents has significant singlet charge transfer (<sup>1</sup>CT) character in polar solvents. Meanwhile, in high polar dichloromethane (MC), AM3 and AM4 shows the mixed emission spectra from <sup>1</sup>LE and <sup>1</sup>CT. The results indicate that the radiative decay channels are efficiently quenched due to the enhanced <sup>1</sup>CT character.

### 3.3.4 Lippert–Mataga plot and excited state dipole moment

Because the SOCT-ISC occurs in the transition between  $^1\text{CT}$  and  $^3\text{LE}$ , it is necessary to distinguish whether the  $S_1$  state in a specific environment (solvent) is due to the CT state or the LE state. In particular, as the solvent polarity increases, the  $S_1$  of the D–A molecule participating in the photochemical reaction changes from  $^1\text{LE}$  to  $^1\text{CT}$ .

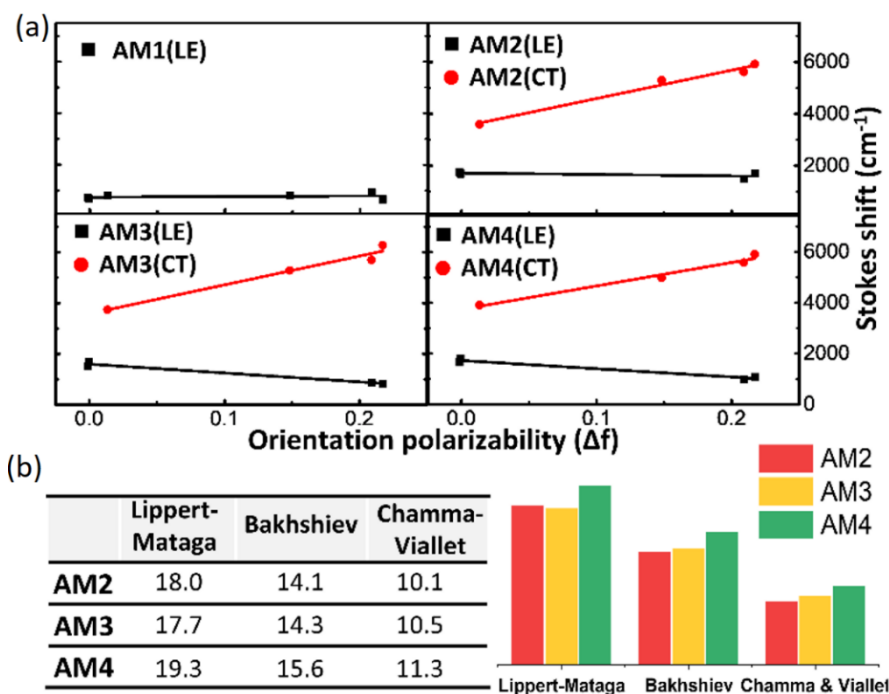


Figure 3.3 (a) Lippert–Mataga plot in different solvents (non-polar: HEX, MCH, low-polar: TOL, mid-polar: CF, high-polar: THF, MC), (b) Excited state dipole moment table and graph of AM2, AM3 and AM4 calculated

by using Lippert-Mataga, Bakshiev and Chamma & Viallet correlation method. [23.24]

Although the characteristics of  $S_1$  were classified by the band shape of the emission spectrum discussed in the previous solvatochromic section, the assignment of  $^1LE$  and  $^1CT$  can be confirmed by the Lippert–Mataga plot. To differentiate between  $^1LE$  and  $^1CT$ , we plotted the Stokes shift against the solvent polarity parameter in five different solvents (i.e., the Lippert–Mataga plot) (Figure 3.3a). The Stokes shift of AM1 in all selected solvents appeared over the small range of 600–800  $cm^{-1}$ , and no specific tendency was observed with respect to the orientation polarizability ( $\Delta f$ ), indicating that the emission of AM1 originated from  $^1LE$ . In contrast, the AM2–4 exhibited two patterns with increasing solvent polarity: one with a significant increase in the Stokes shift and the other with a small change in the Stokes shift. The former appeared in the polar solvent (TOL, CF, THF, and MC), corresponding to the CT state in which the photosensitizers showed large Stokes shifts. The latter appeared in nonpolar and highly polar solvents (HEX, MCH, THF and MC), and can be assigned to the LE state, showing a small Stokes shift regardless of the solvent polarity.

These assigned characteristics of the S<sub>1</sub> state were consistent with the results of the previous solvatochromic section. The magnitude of CT can be estimated by the excited state dipole moment (μ<sub>e</sub>). To obtain the μ<sub>e</sub> of the photosensitizers, ground-state dipole moments from DFT calculations and three different solvatochromic methods (Lippert–Mataga method, Bakshiev method, and Chamma and Viallet method) were considered.[1, 2] Detailed calculations are described as follows.

In order to obtain the excited state dipole moment, photosensitizers are considered as a dipole in a continuum with constant dielectric constant. And Energy level of molecules can be manipulated by the molecular dipole moments and solvent polarizability. In particular, maxima of absorption ( $\bar{\nu}_a$ ) and emission ( $\bar{\nu}_f$ ) of molecules are strongly correlated with energy level of excited and ground state dipole moment, which, therefore, can be calculated from proportionality of linear graphs between polarizability( $f_n$ ) and maxima of spectrum. Such correlation can be determined by Lippert mataga formulation, Bakshiev formulation and Chamma and Viallet formulation.

$$\bar{\nu}_a - \bar{\nu}_f = S_1 f_1(D, n) + \text{constant} \dots \dots \dots \text{eq. 1 (Lippert mataga formulation)}$$

$$\bar{\nu}_a - \bar{\nu}_f = S_2 f_2(D, n) + \text{constant} \dots \dots \dots \text{eq. 2 (Bakshiev formulation)}$$

$$\frac{(\bar{\nu}_a + \bar{\nu}_f)}{2} = S_3 f_3(D, n) + \text{constant} \dots \dots \dots \text{eq. 3 (Chamma and Viallet formulation)}$$

where,  $\bar{\nu}_a$  and  $\bar{\nu}_f$  are respectively the absorption and fluorescence maxima,  $n$  and  $D$  indicate the refractive indices and the dielectric constants of the solvents, respectively,

The proportionalities of the linear fit of  $(\bar{\nu}_a - \bar{\nu}_f)$  and  $\frac{(\bar{\nu}_a + \bar{\nu}_f)}{2}$  versus  $f_m$  ( $D, n$ ) can be expressed by

$$S_1 \text{ and } S_2 = \frac{2(\mu_e - \mu_g)^2}{a^3 h C}, \quad S_3 = -\frac{2(\mu_e^2 - \mu_g^2)}{a^3 h C}$$

where, 'a' is the Onsager cavity radius (in Å) and 'c' and 'h' are the velocity of light and Planck's constant respectively. The polarizability functions  $f_m$  can be expressed as:

$$f_1(D, n) = \frac{D - 1}{2D + 1} - \frac{n^2 - 1}{2n^2 + 1}$$

$$f_2(D, n) = \left( \frac{2n^2 + 1}{n^2 + 2} \right) \left[ \frac{D - 1}{D + 2} - \frac{n^2 - 1}{n^2 + 2} \right]$$

$$f_3(D, n) = \frac{1}{2} f_2(D, n) + \frac{3(n^4 - 1)}{2(n^2 + 2)^2}$$

The obtained  $\mu_e$  increased in the order of AM2 < AM3 < AM4, which indicates that the increase in electron-accepting power induces a strong CT character. (Figure 3.3b) because the strong CT induces large charge separation in the D–A complex, i.e., a high excited dipole moment.

### 3.3.5 Singlet-triplet energy gap ( $\Delta E_{ST}$ ) between $^1CT$ and $^3LE$ state

Figure 3.4 shows fluorescence (in toluene) and phosphorescence (in MCH) spectra of AM2-4 photosensitizers excluding AM1, where the phosphorescence spectrum was not observed. The energy levels of  $S_1$  and  $T_1$  were obtained from the spectra, and  $\Delta E_{ST}$  between  $S_1$  and  $T_1$  was calculated from the difference between the calculated energy levels. As observed in the previous solvatochromic section and Lippert–Mataga experiments, the  $S_1$  state of the AM2–4 photosensitizers were in  $^1LE$  and  $^1CT$  in nonpolar (MCH) and polar (TOL) solvents, respectively. Thus, it is inferred that the  $T_1$  state of the AM2–4 photosensitizers can be in  $^3LE$  in MCH. Therefore,  $\Delta E_{ST}$  obtained from both spectra is between  $^1CT$  and  $^3LE$ .  $\Delta E_{ST}$  decreased from AM2 to AM4, and the same trend was observed in the DFT calculations. The  $\Delta E_{ST}$  value of AM1 obtained from the calculation showed a larger value (1.3 eV) than the other photosensitizers, which certainly makes the ISC process of AM1 difficult to occur.

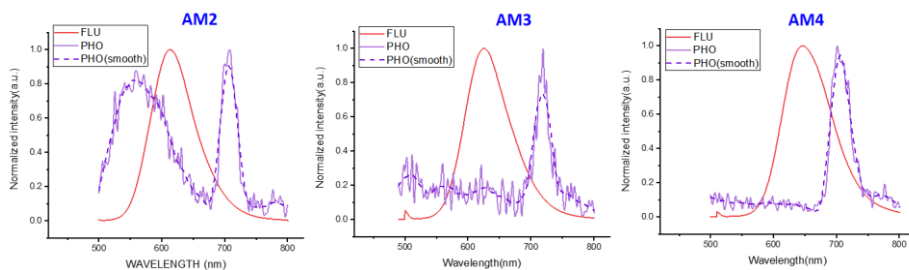


Figure 3.4 Normalized fluorescence spectra of photosensitizers( $10^{-5}\text{M}$ ) in toluene and normalized phosphorescence spectra of photosensitizers( $10^{-5}\text{M}$ ) in methycyclohexane at 77K.

### 3.3.6 Natural transition orbital (NTO) analysis

Because ISC occurs between  $S_1$  and  $T_n$  that can interact with the  $S_1$  state, all the triplet excited states that can interact with  $S_1$  must be verified. Therefore, to investigate the excited states, the natural transition orbitals (NTO) of the excited states were obtained by DFT optimization (Figure 3.5).  $S_1$ ,  $T_1$ , and  $T_2$  of AM1 showed the LE character; thus, the ISC of AM1 cannot occur theoretically. Similarly, because both  $S_1$  and  $T_2$  of AM2–4 showed the CT character, SOCT-ISC cannot occur theoretically between the two states. In contrast, because  $S_1$  and  $T_1$  each have CT and LE characters, SOCT-ISC between the  $S_1$  and  $T_1$  states is possible.

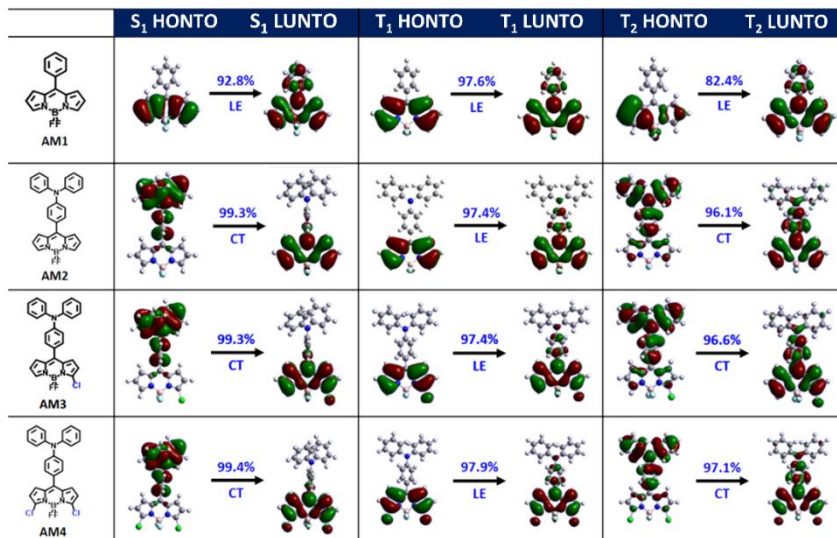


Figure 3.5 Highest occupied and lowest unoccupied natural transition orbitals (HONTO and LUNTO) of AM1–AM4 photosensitizers.

### 3.3.7 Relationship between $\Delta E_{ST}$ and SOQY

Herein, SOQYs were measured using an indirect method with 1,3-diphenylisobenzofuran (DPBF) as a quencher. For accuracy of our results, the SOQY was determined by conducting five independent experiments per sample.

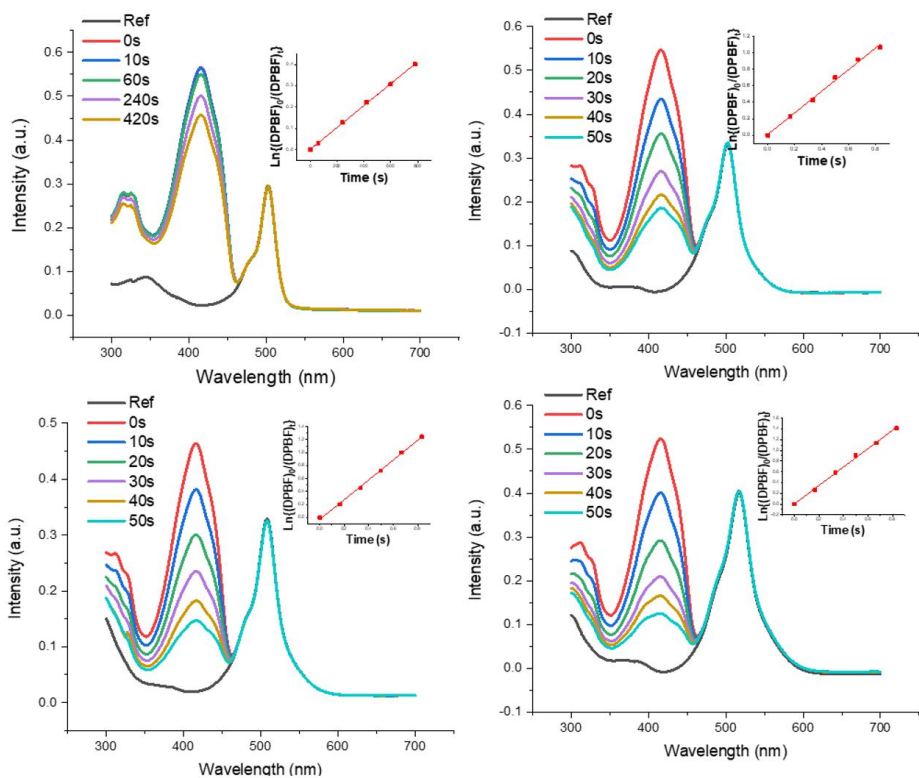


Figure 3.6 Singlet oxygen quantum yield (SOQY) of AM1-AM4 photosensitizers of photosensitizers

Table 3.3 Reorganization energies, singlet- triplet energy gaps and FCWDs, and SOQYs of AM1-4 photosensitizers

|     | States                | $\lambda_T$<br>(eV) | $\Delta E_{ST}$<br>(eV) |        | FCWD  |       | SOQY |
|-----|-----------------------|---------------------|-------------------------|--------|-------|-------|------|
|     |                       |                     | Onset                   | Calc.  | Onset | Calc. |      |
| AM1 | S <sub>1</sub> (LE) – | 0.196               | -                       | - 1.30 | -     | -     | 0.89 |
|     | T <sub>1</sub> (LE)   |                     |                         |        |       |       |      |
| AM2 | S <sub>1</sub> (CT) – | 0.255               | - 0.40                  | -0.35  | 1.56  | 2.47  | 31.9 |
|     | T <sub>1</sub> (LE)   |                     |                         |        |       |       |      |
| AM3 | S <sub>1</sub> (CT) – | 0.256               | - 0.39                  | - 0.31 | 1.76  | 3.11  | 42.3 |
|     | T <sub>1</sub> (LE)   |                     |                         |        |       |       |      |
| AM4 | S <sub>1</sub> (CT) – | 0.256               | - 0.28                  | - 0.28 | 3.40  | 3.42  | 43.5 |
|     | T <sub>1</sub> (LE)   |                     |                         |        |       |       |      |

The SOQYs of the photosensitizers with the CT character were 0.32, 0.42, and 0.44 for AM2, AM3, and AM4, respectively, which were higher than the 0.01 for AM1 (Figure 3.6, Table 3.3). This indicates that the ISC between singlet and triplet states of the AM2–4 photosensitizers increased upon introduction of TPA (D) to BODIPY (A). Unlike AM2–4, the ISC of AM1 upon introduction of benzene did not occur.

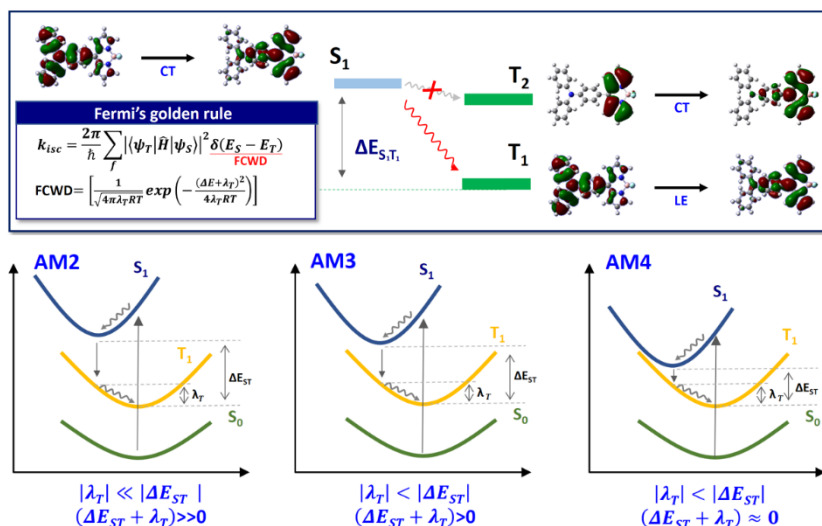
The reduction of  $\Delta E_{ST}$  by lowering the electron-accepting power increased the SOQY. For a more detailed analysis, the Frank–Condon weighted density of state (FCWD) and reorganization E ( $\lambda_T$ ) of Fermi's golden rule were calculated. According to Fermi's golden rule, the rate constant of ISC can be defined as follows:

$$k_{isc} = \frac{2\pi}{\hbar} \sum_f |\langle \psi_T | \hat{H} | \psi_S \rangle|^2 FCWD$$

The FCWD can be represented as follows:

$$FCWD = \left[ \frac{1}{\sqrt{4\pi\lambda_T RT}} \exp\left(-\frac{(\Delta E_{ST} + \lambda_T)^2}{4\lambda_T RT}\right) \right]$$

where  $\lambda_T$  denotes reorganization E and  $\Delta E_{ST}$  is the energy difference between  $S_1$  and  $T_n$ . The reorganization E of AM2–4 photosensitizers showed similar values of 0.255 –0.256 eV, indicating that they have similar structures except for their edges. As the electron-accepting power increased,  $\Delta E_{ST}$  gradually decreased; thus, the value of  $\Delta E_{ST} + \lambda_T$  became closer to zero (Scheme 3.3). This behavior indicates that the lowest energy level of  $S_1$  meets the potential energy surface of  $T_1$ , which can promote ISC from  $S_1$  to  $T_1$  state.



Scheme 3.3 SOCT-ISC between  $^1\text{CT}$  and  $^3\text{LE}$  (above) and schematic mechanisms of the ISC process in AM2, AM3, and AM4 photosensitizers (below).

### 3.3.8 Femtosecond transient absorption spectroscopy (fs-TA) analysis

Fs-TA measurements were performed at different time delays from 0 to 3 ns in toluene to obtain the information on the CT dynamics of AM2-4 photosensitizers. In the range of 450-550 nm, the fs-TA spectra of AM2-4 photosensitizers showed negative bands corresponding to steady state absorption (ground state bleaching, GSB), and no

significant excited state dynamics of the GSB was observed during the measurement time. (Fig. 3.7) However, the stimulated emission (SE) band of AM2-4 photosensitizers in 600-700 nm displayed notable spectral evolutions in a few picoseconds, implying the CT processes from  $^1\text{LE}$  to  $^1\text{CT}$ . The global analysis was conducted to clarify the excited state dynamics of AM2-4 by obtaining evolution-associated spectra (EAS), respectively (Fig. 3.8d-f).

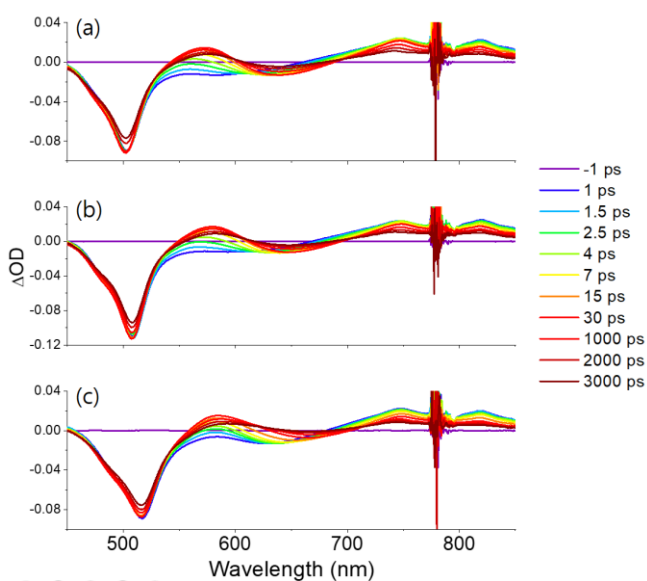


Figure 3.7 Femtosecond transient absorption spectra of AM2 (a), AM3(b) and AM4(c) in deaerated toluene at different delay times ( $\lambda_{\text{ex}} = 510 \text{ nm}$ )

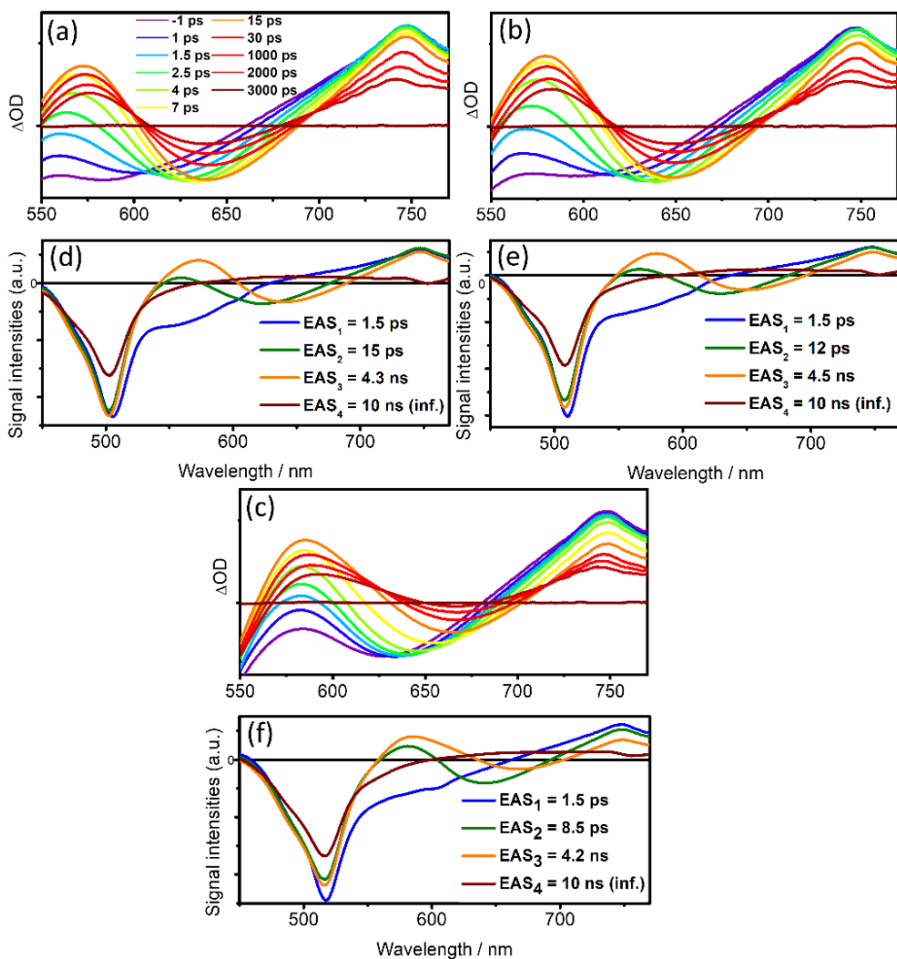


Figure 3.8. Femtosecond transient absorption spectra of AM2 (a), AM3 (b), and AM4 (c) in deaerated TOL at different delay times ( $\lambda_{ex} = 510$  nm), and their corresponding local EAS species from a global analysis of AM2 (d), AM3 (e), and AM4 (f).

The EAS<sub>1</sub> with the fast component was composed of GSB and broad ESA band, which were assigned to the vibrational relaxation or structural reordering processes from the initial Frank Condon state. The characteristic spectral changes were revealed in EAS<sub>2</sub>, showing the red shifts of SE bands within the time scales corresponding to the solvation dynamics of a dipolar molecule in toluene. [25] It indicates that the definite CT processes occur in AM2-4. Furthermore, the systematically enhanced CT processes were observed for photosensitizers with larger accepting power, showing the faster CT transition. These results are correspondent with the solvatochromic properties where the substituents of the electron donor group bring about the efficient CT transition. EAS<sub>3</sub> and EAS<sub>4</sub> indicate the singlet state lifetime and the generation of the triplet state from the singlet CT states, respectively.

### **3.3.9 Nanosecond transient absorption spectroscopy (Ns-TA).**

Ns-TA were measured to investigate the triplet character of the photosensitizers (Figure 3.9). Similar to that observed for the fs-TA, the GSB bands of AM2–4 photosensitizers were shown over the range of 450–580 nm, corresponding to the GSB band of each photosensitizer.

In addition, the ESA bands of the photosensitizers were observed over the range of 400–450 nm, which is typical for  $T_1 \rightarrow T_n$  transition of BODIPY. [26] The triplet state lifetimes determined from the decay profile at 430 nm were  $\sim 12\text{--}13\ \mu\text{s}$ , which indirectly demonstrate that ISC occurred from  $S_1$  to  $T_1$  in both AM2–4 photosensitizers.

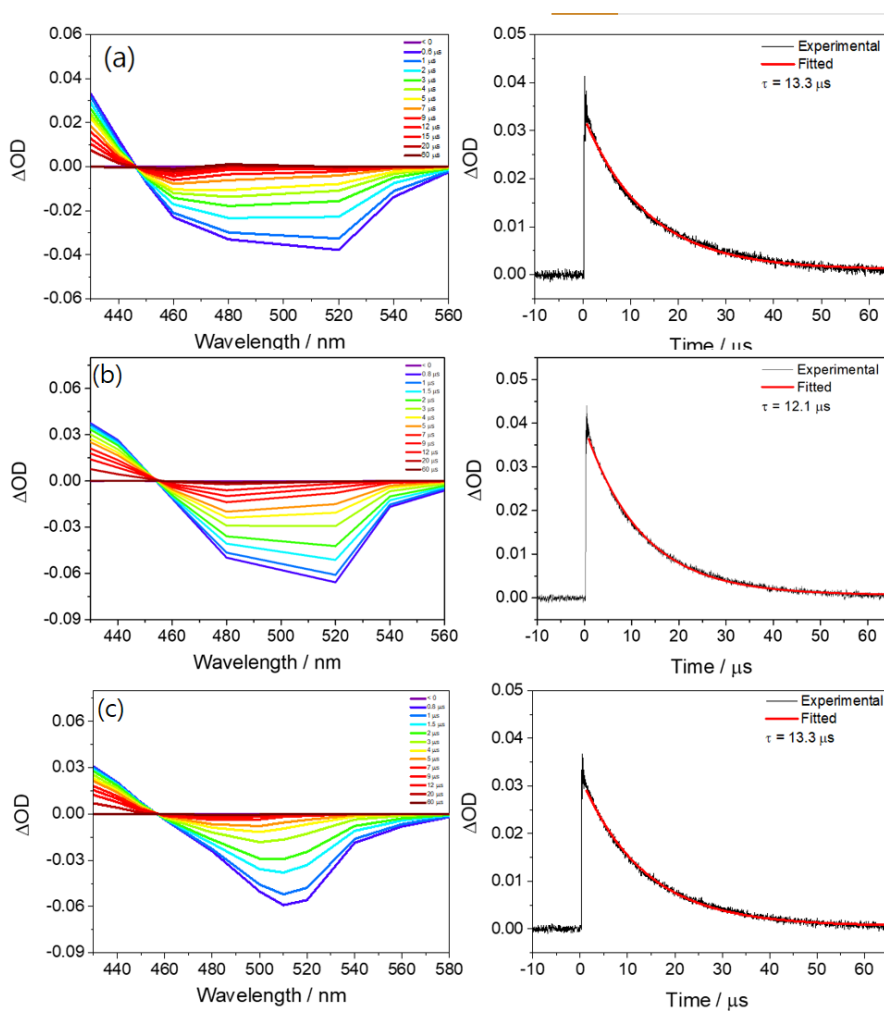


Figure 3.9 Nanosecond transient absorption spectra (left) and its decay

profile (right) of (a) AM2, (b) AM3, and (c) AM4 at 430nm in deaerated toluene.

### 3.4 Conclusions

In conclusion, our research goal was to assess and investigate the correlation between  $\Delta E_{ST}$  and SOQY to understand the mechanism of SOCT-ISC and to find strategies to improve SOQY. For this, three D–A photosensitizers (AM2–4) with the CT character and a standard (AM1) without the CT character were synthesized. The AM2–4 photosensitizers showed higher SOQY than AM1, which indicates that D–A molecules can increase the ISC rate because of the CT character. In addition, as the electron-accepting power increased,  $\Delta E_{ST}$  between  $^1CT$  and  $^3LE$  gradually decreased, which increased SOQY. This is because the value of  $(\Delta E_{ST} + \lambda_T)$  approaches zero as  $\Delta E_{ST}$  decreases. This study confirmed that the reduction of  $\Delta E_{ST}$  between  $^1CT$  and  $^3LE$  by controlling the CT character can lead the photosensitizers to have a high SOQY. Despite this, further studies focused on the investigation of the correlation between  $\Delta E_{ST}$  and SOQY should be conducted to generalize this hypothesis.

### 3.5 References

- [1] Gorman A, Killoran J, O'Shea C, Kenna T, Gallagher WM, O'Shea DF. In Vitro Demonstration of the Heavy-Atom Effect for Photodynamic Therapy. *Journal of the American Chemical Society*. 2004;126(34):10619-31.
- [2] Yang Y, Guo Q, Chen H, Zhou Z, Guo Z, Shen Z. Thienopyrrole-expanded BODIPY as a potential NIR photo-sensitizer for photodynamic therapy. *Chemical Communications*. 2013;49(38):3940-2.
- [3] Zou J, Yin Z, Ding K, Tang Q, Li J, Si W, et al. BODIPY Derivatives for Photodynamic Therapy: Influence of Configuration versus Heavy Atom Effect. *ACS Applied Materials & Interfaces*. 2017;9(38):32475-81.
- [4] Diwu Z, Lown JW. Photosensitization with anticancer agents: 15. Perylenequinonoid pigments as potential photodynamic therapeutic agents: Formation of semiquinone radicals and reactive oxygen species on illumination. *Journal of Photochemistry and Photobiology B: Biology*. 1993;18(2):131-43.
- [5] Kriska T, Korecz L, Nemes I, Gal D. Physicochemical Modeling of the Role of Free Radicals in Photodynamic Therapy. III. Interactions of Stable Free Radicals with Excited Photosensitizers Studied by Kinetic

ESR Spectroscopy. Biochemical and Biophysical Research Communications. 1995;215(1):192-8.

[6] Viola A, Hadjur C, Jeunet A, Julliard M. Electron paramagnetic resonance evidence of the generation of superoxide ( $O_2^-$ ) and hydroxyl ( $\cdot OH$ ) radicals by irradiation of a new photodynamic therapy photosensitizer, Victoria Blue BO. Journal of Photochemistry and Photobiology B: Biology. 1996;32(1):49-58.

[7] Wang Z, Gao Y, Hussain M, Kundu S, Rane V, Hayvali M, et al. Efficient Radical-Enhanced Intersystem Crossing in an NDI-TEMPO Dyad: Photophysics, Electron Spin Polarization, and Application in Photodynamic Therapy. Chemistry – A European Journal. 2018;24(70):18663-75.

[8] Huang L, Yu X, Wu W, Zhao J. Styryl Bodipy-C60 Dyads as Efficient Heavy-Atom-Free Organic Triplet Photosensitizers. Organic Letters. 2012;14(10):2594-7.

[9] Ji S, Ge J, Escudero D, Wang Z, Zhao J, Jacquemin D. Molecular Structure–Intersystem Crossing Relationship of Heavy-Atom-Free BODIPY Triplet Photosensitizers. The Journal of Organic Chemistry. 2015;80(11):5958-63.

- [10] Chen K, Yang W, Wang Z, Iagatti A, Bussotti L, Foggi P, et al. Triplet Excited State of BODIPY Accessed by Charge Recombination and Its Application in Triplet–Triplet Annihilation Upconversion. *The Journal of Physical Chemistry A*. 2017;121(40):7550-64.
- [11] Wang Z, Zhao J. Bodipy–Anthracene Dyads as Triplet Photosensitizers: Effect of Chromophore Orientation on Triplet-State Formation Efficiency and Application in Triplet–Triplet Annihilation Upconversion. *Organic Letters*. 2017;19(17):4492-5.
- [12] Zhang X-F, Yang X, Xu B. PET-based bisBODIPY photosensitizers for highly efficient excited triplet state and singlet oxygen generation: tuning photosensitizing ability by dihedral angles. *Physical Chemistry Chemical Physics*. 2017;19(36):24792-804.
- [13] Filatov MA. Heavy-atom-free BODIPY photosensitizers with intersystem crossing mediated by intramolecular photoinduced electron transfer. *Organic & Biomolecular Chemistry*. 2020;18(1):10-27.
- [14] O'Connor AE, Gallagher WM, Byrne AT. Porphyrin and Nonporphyrin Photosensitizers in Oncology: Preclinical and Clinical Advances in Photodynamic Therapy. *Photochemistry and Photobiology*. 2009;85(5):1053-74.

- [15] Wang Z, Ivanov M, Gao Y, Bussotti L, Foggi P, Zhang H, et al. Spin–Orbit Charge-Transfer Intersystem Crossing (ISC) in Compact Electron Donor–Acceptor Dyads: ISC Mechanism and Application as Novel and Po-tent Photodynamic Therapy Reagents. *Chemistry – A European Journal*. 2020;26(5):1091-102.
- [16] Rehmat N, Toffoletti A, Mahmood Z, Zhang X, Zhao J, Barbon A. Carbazole-perylenebisimide electron do-nor/acceptor dyads showing efficient spin orbit charge transfer intersystem crossing (SOCT-ISC) and photo-driven intermolecular electron transfer. *Journal of Materials Chemistry C*. 2020;8(14):4701-12.
- [17] Zhao J, Chen K, Hou Y, Che Y, Liu L, Jia D. Recent progress in heavy atom-free organic compounds show-ing unexpected intersystem crossing (ISC) ability. *Organic & Biomolecular Chemistry*. 2018;16(20):3692-701.
- [18] Lim BT, Okajima S, Chandra AK, Lim EC. Radiationless transitions in electron donor-acceptor complexes: selection rules for  $S_1 \rightarrow T$  intersystem crossing and efficiency of  $S_1 \rightarrow S_0$  internal conversion. *Chemical Physics Letters*. 1981;79(1):22-7.
- [19] Hou Y, Liu Q, Zhao J. An exceptionally long-lived triplet state of red light-absorbing compact phenothiazine-styrylBodipy electron

donor/acceptor dyads: a better alternative to the heavy atom-effect?

Chemical Communications. 2020;56(11):1721-4.

[20] Lei Y, Chen K, Tang G, Zhao J, Gurzadyan GG. Bodipy-Phenylethynyl Anthracene Dyad: Spin-Orbit Charge Transfer Intersystem Crossing and Triplet Excited-State Equilibrium. Journal of Photochemistry and Photobiology A: Chemistry. 2020;398:112573.

[21] Liang H, Sun S, Zafar M, Yuan Z, Dong Y, Ji S, et al. Tuning the SOCT-ISC of bodipy based photosensitizers by introducing different electron donating groups and its application in triplet-triplet-annihilation upconversion. Dyes and Pigments. 2020;173:108003.

[22] Mao Y, Head-Gordon M, Shao Y. Unraveling substituent effects on frontier orbitals of conjugated molecules using an absolutely localized molecular orbital based analysis. Chemical Science. 2018;9(45):8598-607.

[23] Mukhopadhyay A, Maka VK, Moorthy JN. Remarkable influence of 'phane effect' on the excited-state properties of cofacially oriented coumarins. Physical Chemistry Chemical Physics. 2017;19(6):4758-67.

[24] Zhao YH, Abraham MH, Zissimos AM. Fast Calculation of van der Waals Volume as a Sum of Atomic and Bond Contributions and Its

Application to Drug Compounds. *The Journal of Organic Chemistry*. 2003;68(19):7368-73.

[25] Dereka B, Vauthey E. Solute–Solvent Interactions and Excited-State Symmetry Breaking: Beyond the Di-pole–Dipole and the Hydrogen-Bond Interactions. *The Journal of Physical Chemistry Letters*. 2017;8(16):3927-32.

[26] Dong Y, Sukhanov AA, Zhao J, Elmali A, Li X, Dick B, et al. Spin–Orbit Charge-Transfer Intersystem Cross-ing (SOCT-ISC) in Bodipy-Phenoxazine Dyads: Effect of Chromophore Orientation and Conformation Restriction on the Photophysical Properties. *The Journal of Physical Chemistry C*. 2019;123(37):22793-811.

[27] Zhang X-F, Yang X. Singlet Oxygen Generation and Triplet Excited-State Spectra of Brominated BODIPY. *The Journal of Physical Chemistry B*. 2013;117(18):5533-9.

[28] Mukhopadhyay A, Maka VK, Moorthy JN. Remarkable influence of ‘phane effect’ on the excited-state properties of cofacially oriented coumarins. *Physical Chemistry Chemical Physics*. 2017;19(6):4758-67.

[29] Zhao YH, Abraham MH, Zissimos AM. Fast Calculation of van der Waals Volume as a Sum of Atomic and Bond Contributions and Its

Application to Drug Compounds. *The Journal of Organic Chemistry*. 2003;68(19):7368-73.

[30] Min C-K, Joo T, Yoon M-C, Kim CM, Hwang YN, Kim D, et al. Transient absorption anisotropy study of ultrafast energy transfer in porphyrin monomer, its direct meso–meso coupled dimer and trimer. *The Journal of Chemical Physics*. 2001;114(15):6750-8.

## **Chapter 4**

# **Synergistic effects of photoinduced electron transfer and heavy atom effect based on BODIPY for efficient triplet photosensitizers**

### **4.1 Introductions**

Triplet sensitizers are molecules capable of generating electrons in excited triplet states; these have applications in several fields such as photocatalytic organic reactions, OLEDs, and photodynamic therapy (PDT). [1] In particular, triplet–triplet annihilation-based upconversion (TTA-UC), in which triplet sensitizers play a key role, have attracted more attention owing to their unique anti-Stokes photoluminescence properties. Porphyrin-based sensitizers have been the most widely used as triplet sensitizers; however, because of their major disadvantages, such as low absorption coefficient, dark toxicity, and long-lasting photosensitivity, recently, there has been growing demand for the non-porphyrin-based triplet photosensitizers. However, non-porphyrin-based

sensitizers generally have a low intersystem crossing (ISC) yield and short triplet lifetime than that of porphyrin-based ones; thus, it becomes challenging to enhance triplet properties.

Among the various strategies for developing non-porphyrin-based triplet photosensitizers, the heavy atom effect (HAE) and photoinduced electron transfer (PET) are the most widely used. [2-7] In HAE, heavy atoms such as selenium and bromine in the photosensitizer generate spin-orbit coupling (SOC), which results in a higher ISC yield between the singlet and triplet states. The magnitude of the SOC is determined based on the probability of electrons encountering a heavy atom. [8]

In contrast, PET in donor-acceptor (D-A) molecules generates a charge transfer state, which results in ISC from the singlet state to the triplet state. ISC by PET is caused by spin-orbit charge transfer (SOCT) or hyperfine coupling (HFC). Although it is not clear which mechanism is more prevalent, it is obvious that increasing the charge separation between D and A enhances the ISC. [9]

To improve charge separation, various strategies are commonly used to increase the electron donating or accepting capability of the molecule or to ensure that the dihedral angle between D and A is close to  $90^\circ$ . [10] Theoretically, both mechanisms, HAE and PET, are local effects wherein

electrons adjacent to heavy atoms induce ISC because of the HAE, and the electrons transferred from D to A induce ISC because of the SOCT or HFC. Therefore, if both strategies are introduced in the same molecule, the ISC may be independently generated according to the spatial distribution of electrons, resulting in an increased ISC yield.

Several researchers have studied triplet sensitizers, independently investigating HAE and PET. [2-7] However, to the best of our knowledge, the simultaneous utilization of HAE and PET has not been investigated. Here, we developed novel non-porphyrin-based donor-acceptor-heavy atom (D-A-H) photosensitizers, in which both HAE and PET strategies were involved in the same molecule. The triplet characteristics and their singlet oxygen quantum yield ( $\Phi_{\Delta}$ ), triplet lifetime ( $\tau_T$ ), and photophysical dynamics were thoroughly investigated. Finally, the synthesized triplet sensitizers were employed to achieve TTA-UC and photochemical characteristics, which were observed to be precisely correlated with triplet characteristics.

## **4.2 Experimental**

### **4.2.1 Materials**

All of the commercial reagents were purchased from Sigma-Aldrich or

Tokyo Chemical Industry (TCI) and used without further purification. Anhydrous solvents used in the reactions were purchased from Sigma-Aldrich or Alfa aesar.

#### **4.2.2 Instruments**

<sup>1</sup>H NMR spectra were recorded on a Bruker Avance 500 spectrometer (National Center for Inter-University Research Facilities at Seoul National University) at 500 MHz using chloroform-d with tetramethylsilane (TMS). High resolution mass experiments were operated on a Q-TOF 5600 mass spectrometer (AM2, AM5, AM6, and AM7) equipped with an ESI source (National Instrumentation Center for Environmental Management) and on JMS-700 (JEOL, Japan), 6890 Series (AM8). Solvatochromic absorption and fluorescence solutions were measured by an UV-vis spectrophotometer (LAMBDA 25, Perkin Elmer Co.) and a fluorescence spectrometer (LS-55, Perkin Elmer Co.), respectively. Photoluminescence quantum yield (PLQY) of 10 μM photosensitizers in various solvents were estimated using an integrating sphere (QE-1100, Otsuka electronics Co.).

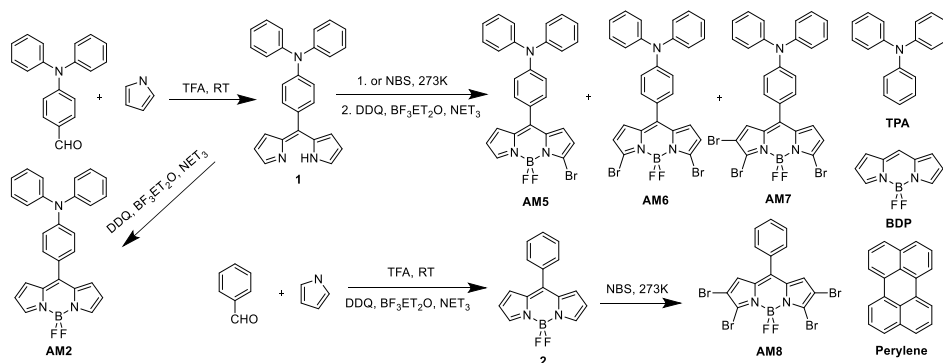
## 4.2.3 Synthesis

### 4.2.3.1 Preparation of compound 1, 2, and AM2

Synthesis and characterization of 1, 2, and AM2 are described on chapter3. [11]

### 4.2.3.2 Preparation of compound AM5, AM6, and AM7

In a three-neck flask, a crude mixture of compound 1 (584 mg, 1.5 mmol) was dissolved into dry THF (30 ml) and the mixture was cooled to -78 °C under nitrogen atmosphere. N-bromosuccinimide, (587mg, 3.3 mmol) was slowly added over 30 min.



Scheme 4.1 Synthesis of the photosensitizers (AM2-AM8). A triphenylamine (TPA), a BODIPY (BDP) and a perylene moiety for measuring cyclic voltammetry and TTA-UC preperities

After 2 h, 2,3-Dichloro-5,6-dicyano-1,4-benzoquinone, DDQ (341 mg, 1.5 mmol) in 5 ml dry THF was added dropwise over 10 min at same temperature. Then the reaction temperature was increased to RT and the solvent was distilled on rotary evaporator. Then the crude compound was dissolved in 50 ml dichloromethane, neutralized with triethylamine (7.30 ml, 52 mmol) and treated with  $\text{BF}_3 \cdot \text{Et}_2\text{O}$  (9.4 ml, 74.6 mmol) at room temperature for additional 2-3 h. The reaction mixture was quenched with 20 ml 0.1 M NaCl solution and extract from water. The organic layer was dried over  $\text{MgSO}_4$ , filtered, and evaporated. The crude product was purified by silica gel column chromatography eluting with hexane/dichlorometane (1:1) to produce compound **AM5** (44 mg, 5.7% yield) **AM6** (86 mg, 9.6% yield) and **AM7** (37 mg, 3.6% yield) as violet solid.

**AM5**:  $^1\text{H NMR}$  (500 MHz,  $\text{CDCl}_3$ )  $\delta$  7.92 (s, 2H), 7.43-7.39 (d,  $J=8.7\text{Hz}$ , 2H), 7.38-7.33 (t,  $J=8.2\text{Hz}$ , 4H), 7.23-7.20 (d,  $J=7.5\text{Hz}$ , 4H), 7.19-7.14 (t,  $J=7.4\text{Hz}$ , 2H), 7.12-7.07 (d,  $J=7.3\text{Hz}$ , 2H), 7.04 (m, 1H), 6.96 (d,  $J=4.2\text{Hz}$ , 1H), 6.57 (m, 1H), 6.55-6.51(d,  $J=4.3\text{Hz}$ , 1H)  $^{13}\text{C NMR}$  (500 MHz,  $\text{CDCl}_3$ )  $\delta$  151.0, 146.4, 143.2, 132.2, 131.3, 131.1, 129.7 126.0, 125.4, 124.8, 120.0, HRMS-ESI ( $\text{M}+\text{H}^+$ ) Calcd for  $\text{C}_{27}\text{H}_{20}\text{BrF}_2\text{N}_3$ : 514.0902. Found: 514.0870 **AM6**:  $^1\text{H NMR}$  (500

MHz, CDCl<sub>3</sub>) δ 7.39-7.33 (m, 6H), 7.23-7.19 (d, J=7.6Hz, 4H), 7.19-7.14 (t, J=7.4Hz, 2H), 7.08 (d, J=8.7, 2H), 6.93 (d, J=4.1Hz, 2H), 6.55 (d, J=4.3Hz, 2H) 13C NMR (500 MHz, CDCl<sub>3</sub>) δ 151.3, 146.6, 143.8, 135.4, 132.4, 131.5, 131.2, 130.0, 126.2, 125.1, 124.9 122.4, 120.1 HRMS-ESI (M+H+) Calcd for C<sub>27</sub>H<sub>19</sub>BBr<sub>2</sub>F<sub>2</sub>N<sub>3</sub>: 593.9987. Found: 593.9952 **AM7**: 1H NMR (500 MHz, CDCl<sub>3</sub>) δ 7.41-7.33 (m, J=8.4Hz, 6H), 7.24-7.16 (m, J=7.4Hz, 6H), 7.11-7.06 (d, J=8.7Hz, 2H), 6.98 (s, 2H), 6.59 (d, J=4.4Hz, 2H) 13C NMR (500 MHz, CDCl<sub>3</sub>) δ 151.6, 146.4, 143.6, 135.6, 134.4, 133.3, 132.6, 132.5, 131.1, 130.2, 130.0 126.4, 125.3, 124.3, 123.2 120.0, 110.4 HRMS-ESI (M+H+) Calcd for C<sub>27</sub>H<sub>18</sub>BBr<sub>3</sub>F<sub>2</sub>N<sub>3</sub>: 670.9056. Found: 670.9076

#### 4.2.3.3 Preparation of compound AM8

To **2** (25 mg, 0.093 mmol) in 10 ml of dry in CH<sub>2</sub>Cl<sub>2</sub> was added dropwise N-bromosuccinimide (NBS) (83mg, 0.465 mmol) in CH<sub>2</sub>Cl<sub>2</sub> (5 ml) over a period of 0.5h. The mixture was left stirring for an additional 24 h, washed with an aqueous solution of sodium chloride, and extracted by CH<sub>2</sub>Cl<sub>2</sub>. Organic layers were extracted, dried over MgSO<sub>4</sub>, and evaporated to dryness. Purification was performed by column

chromatography on silica gel using hexane/CH<sub>2</sub>Cl<sub>2</sub> (1:1, v/v). AM8 was obtained as dark purple solid (13mg, 37% yield)

**AM8** <sup>1</sup>H NMR (500 MHz, CDCl<sub>3</sub>) δ 7.65-7.62 (t, J=7.5Hz, 1H), 7.57-7.54 (t, J=8Hz, 2H), 7.49-7.47 (d, J=7.5Hz, 2H), 6.91 (s, 2H) <sup>13</sup>C NMR (500 MHz, CDCl<sub>3</sub>) δ 143.0, 135.4, 135.0, 131.8, 131.7, 130.5, 129.1, 112.3 HRMS-ESI (M+H<sup>+</sup>) Calcd for C<sub>27</sub>H<sub>18</sub>BBr<sub>3</sub>F<sub>2</sub>N<sub>3</sub>: 579.7404. Found: 579.7408

#### 4.2.4 Singlet oxygen quantum yield measurements

SOQY were measured by using the indirect method in toluene. (standard: 2,3,7,8-tetrabromo-5,5-difluoro-10-phenyl-5H-4(1H),5(1H)-dipyrrolo[1,2-c:2',1'-f][1,3,2]diazaborinine, Φ<sub>Δ</sub> = 0.49 in toluene) [7] To determine SOQY, a following eqn 4.1 was used:

$$\Phi_{\Delta,sam} = \Phi_{\Delta,std} \left( \frac{m_{sam}}{m_{std}} \right) \left( \frac{1-10^{-A_{std}}}{1-10^{-A_{sam}}} \right) \left( \frac{n_{sam}}{n_{std}} \right)^2 \quad \text{eqn. 4.1}$$

where Φ<sub>Δ, sam</sub> – SOQY of the sample, Φ<sub>Δ, std</sub> – SOQY of the standard (AM8 in toluene). m<sub>std</sub> and m<sub>sam</sub> – the slope of the absorbance changing at 413nm in standard and the sample. n<sub>std</sub> and n<sub>sam</sub> – the refractive index of solution in which the standard and the sample are dissolved. Oxygen was bubbled into the solvents for 30min before sample preparation. All

samples in 3.5ml solvents contained diphenylisobenzofuran (DPBF) were irradiated with laser (505nm. 3.16mW  $\pm$ 3%). The concentration of DPBF was fixed to 30mM for preventing from chain reaction.

#### 4.2.5 TTA-UC emission efficiency measurement

The TTA-UC emission efficiency ( $\eta_{UC}$ ) of samples was measured relative to the fluorescence quantum yield of AM5 in toluene in response to laser excitation at 532 nm ( $\Phi_{std}$  (AM5) = 2.4%, measured using QE-1100, Otsuka). The calculation of efficiency yield was performed with using eqn 4.2.

$$\eta_{UC,sam} = 2\Phi_{std} \left( \frac{I_{sam}}{I_{std}} \right) \left( \frac{1-10^{-A_{std}}}{1-10^{-A_{sam}}} \right) \left( \frac{n_{sam}}{n_{std}} \right)^2 \quad \text{eqn. 4.2}$$

Where  $\eta_{UC, sam}$  – upconversion emission efficiency of the sample,  $\Phi_{std}$  – fluorescence quantum yield of the standard (AM5 in toluene).  $I_{std}$  and  $I_{sam}$  – Integrated photoluminescence intensities of the standard and the sample.  $A_{std}$  and  $A_{sam}$  – Absorbance of standard and sample at excitation wavelength.  $n_{std}$  and  $n_{sam}$  – the refractive index of solution in which the standard and the sample are dissolved.

#### 4.2.6 Calculation

The ground and excited state geometry was optimized with Gaussian

09 software using the DFT and TDDFT/B3LYP hybrid functional and the 6-31+G (d, p) basis set with toluene as a solvent (IEFPCM). The dihedral angle between donor and acceptor obtained from the optimized geometry at  $S_0$ . Overlap integral of  $S_1$  transition was analyzed by multifunctional wavefunction analyzer (Multiwfn) version 3.7. [12] Spin orbit coupling matrix element (SOCME) was calculated using the ORCA.

## **4.3 Results and discussion**

### **4.3.1 Molecular designs**

To investigate the synergistic effect of HAE and PET, three different D-A-H photosensitizers (AM5, AM6, and AM7) were prepared: donor, acceptor, and heavy atom of the D-A-H photosensitizers were selected as triphenylamine (TPA), BODIPY, and bromine, respectively.

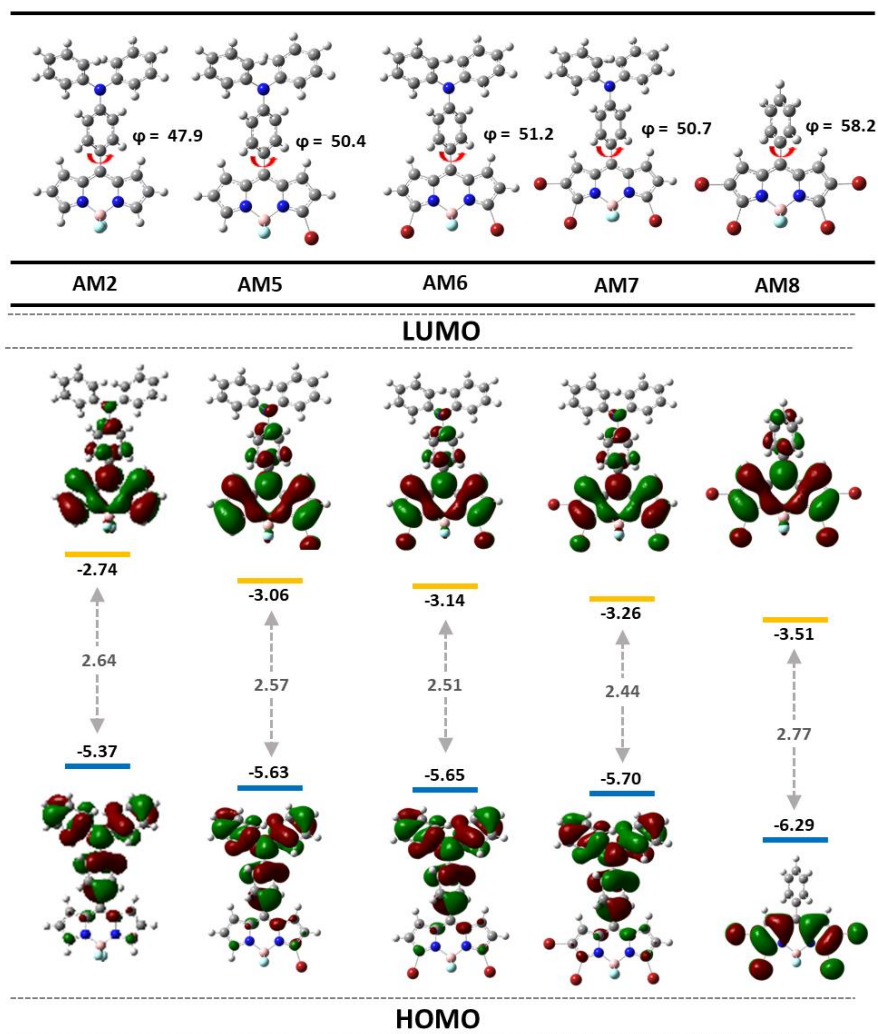


Figure 4.1 Optimized geometry, the highest occupied molecular orbital (HOMO) and lowest unoccupied molecular orbital (LUMO) of AM2-AM8 photosensitizers

AM2 and AM8 were prepared as standards, with their structures containing only a donor-acceptor (D-A) and heavy atoms on BODIPY,

respectively. To examine the effect of the number of bromine atoms, AM2(0Br), AM5(1Br), AM6(2Br), and AM7(3Br) were designed. Bromine atoms were introduced at the end of BODIPY to maintain the dihedral angle between D and A. And they were 48–51°, which indicates that the PET of molecules is only affected by the number of bromine atoms and not by the dihedral angles (Figure 4.1). It is expected that the HAE and the degree of charge separation by PET will increase by increasing the number of bromine atoms in the following order: AM2(0Br) < AM5(1Br) < AM6(2Br) < AM7(3Br)), resulting in an increased SOQY. In contrast, AM8 results in a low SOQY because PET does not occur.

### 4.3.2 Solvatochromic properties

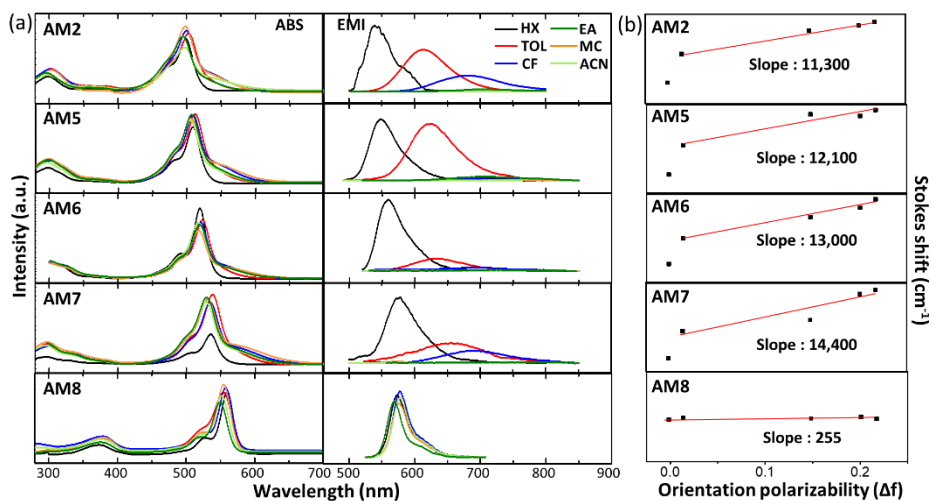


Figure 4.2 (a) UV-VIS absorption, emission spectra, and (b) Lippert-Mataga plots of AM2–AM8 photosensitizers in hexane (HX), toluene (TOL), chloroform (CF), ethyl acetate (EA), dichloromethane (MC), and acetonitrile (ACN) solutions.

The absorption and emission spectra of AM2-AM8 were measured using different solvents (Figure 4.2). All photosensitizers exhibited a constant wavelength of absorption maximum, irrespective of solvent polarity. For AM2–8, an additional weak absorption was observed on the low energy side of the major band. Considering that the weak absorption band increases and the bandwidth broadens with increasing solvent polarity, it can be deduced that the band corresponds to the charge transfer

absorption ( $S_0 \rightarrow {}^1\text{CT}$  state). Unlike the absorption spectra, as the solvent polarity increased, the emission maxima of the AM2-8 photosensitizers were bathochromically shifted and their photoluminescence quantum yields were reduced. (Table 4.1). The emission spectra of the photosensitizers AM2–AM7 in hexane mirrored the respective absorption spectra, corresponding to the local excitation ( ${}^1\text{LE}$ ) band from the local excited state. The emission spectra of AM2–AM7 in polar solvents, such as toluene, showed shapeless and broad emission bands, corresponding to the charge transfer ( ${}^1\text{CT}$ ) band. The existence of the CT absorption band and solvent-dependent fluorescence quenching indicated that the charge separation in AM2–AM7 was due to PET, as was intended. The linear dependence of the Stokes shift of the photosensitizers on solvent polarizability ( $\Delta f$ ) was demonstrated using the Lippert–Mataga plot (Figure 4.2b, Tables 4.2). For AM8, a non-linear relationship was observed between the Stokes shift and  $\Delta f$  (R-square = 0.11), indicating that the emission of AM8 originated from the  ${}^1\text{LE}$  state. For AM2–AM7, Stokes shift increased significantly with increasing  $\Delta f$ . However, the Stokes shift in hexane deviated considerably from the overall trend because the emission in hexane originated from the  ${}^1\text{LE}$  state, unlike those in other solvents that

are initiated from the  $^1\text{CT}$  state. To evaluate the magnitude of charge separation, the changes in dipole moment ( $\Delta\mu_{\text{ge}} = \mu_{\text{e}} - \mu_{\text{g}}$ ) of the  $^1\text{CT}$  states were calculated from the slopes of the Lippert-Mataga plots obtained in polar solvents.

According to the Lippert–Mataga equation (eqn. 4.3)

$$\bar{\nu}_{\text{a}} - \bar{\nu}_{\text{f}} = S \cdot f(D, n) + \text{constant} \quad \text{eqn. 4.3}$$

where  $\bar{\nu}_{\text{a}}$  and  $\bar{\nu}_{\text{f}}$  are the absorption and emission wavenumbers, respectively, and  $D$  and  $n$  are the dielectric constants and refractive index of the solvents, respectively. The slope ( $S$ ) obtained from linear regression of the Lippert-Mataga plot (eqn. 4.4) and the orientation polarizability functions (eqn. 4.5) are expressed as

$$S = \frac{2(\Delta\mu_{\text{ge}})^2}{a^3hc} \quad \text{eqn. 4.4}$$

$$f(D, n) = \frac{D-1}{2D+1} - \frac{n^2-1}{2n^2+1} \quad \text{Eqn. 4.5}$$

where  $a$ ,  $h$ , and  $c$  are the Onsager cavity radius, Planck's constant, and the speed of light in vacuum, respectively. A larger cavity radius was obtained from the optimized geometry using DFT/B3LYP(6-31G+(d, p)) in toluene as a solvent (IEFPCM). All the calculated parameters are summarized in Tables 4.2. AM2, AM5, AM6, and AM7 showed higher  $\Delta\mu_{\text{ge}}$  values of 12.39 D, 12.82 D, 13.67 D, and 15.00 D, respectively,

compared to the change in dipole moment of AM8 ( $\Delta\mu_{ge} = 1.67$  D). A large value of  $\Delta\mu_{ge}$  indicates charge separation through PET; therefore, the electric charge of AM8 may not be separated. [13-16] In addition,  $\Delta\mu_{ge}$  increased in the order of AM2 < AM5 < AM6 < AM7, indicating that the additional bromine atoms enhanced electron-accepting power and induced a strong PET character.

Table 4.1 Absorption and emission maximum wavelength, absorption coefficients, stokes shift and photoluminescence quantum yield of photosensitizers in different solvents. (n-hexane (HX), toluene (TOL), chloroform (CF), ethyl-acetate (EA), dichloromethane (MC))

| Solvents |     | $\lambda_{abs}$<br>[nm] | $\epsilon$<br>[M <sup>-1</sup> cm <sup>-1</sup> ] | $\lambda_{emi}$<br>[nm] | $\Delta f$<br>[nm] | $\Phi_F$ |
|----------|-----|-------------------------|---|-------------------------|--------------------|----------|
| AM2      | HX  | 499                     | 40,000  | 540                     | 41                 | 0.34     |
|          | TOL | 503                     | 45,000  | 614                     | 111                | 0.32     |
|          | CF  | 500                     | 47,000  | 680                     | 180                | 0.11     |
|          | EA  | 496                     | 42,000  | 690                     | 194                | 0.04     |
|          | MC  | 498                     | 50,000  | 706                     | 208                | 0.01     |
|          | ACN | 497                     | 34,000  | -                       | -                  | < 0.01   |
| AM5      | HX  | 509                     | 83,000  | 549                     | 40                 | 0.02     |

|       |     |     |        |     |     |        |
|-------|-----|-----|--------|-----|-----|--------|
|       | TOL | 512 | 72,000 | 626 | 114 | 0.02   |
|       | CF  | 509 | 68,000 | 722 | 213 | < 0.01 |
|       | EA  | 507 | 69,000 | 712 | 205 | < 0.01 |
|       | MC  | 507 | 64,000 | 734 | 218 | < 0.01 |
|       | ACN | 506 | 63,000 | -   | -   | < 0.01 |
| <hr/> |     |     |        |     |     |        |
|       | HX  | 520 | 75,000 | 560 | 40  | 0.05   |
|       | TOL | 523 | 62,000 | 629 | 16  | 0.01   |
| AM6   | CF  | 520 | 55,000 | 691 | 171 | < 0.01 |
|       | EA  | 522 | 54,000 | 729 | 207 | < 0.01 |
|       | MC  | 518 | 53,000 | 755 | 237 | < 0.01 |
|       | ACN | 518 | 54,000 | -   | -   | < 0.01 |
| <hr/> |     |     |        |     |     |        |
|       | HX  | 535 | 35,000 | 578 | 43  | 0.03   |
|       | TOL | 538 | 82,000 | 656 | 118 | < 0.01 |
|       | CF  | 535 | 72,000 | 688 | 153 | < 0.01 |
| AM7   | EA  | 533 | 77,000 | 786 | 253 | < 0.01 |
|       | MC  | 531 | 76,000 | 800 | 269 | < 0.01 |
|       | ACN | 529 | 74,000 | -   | -   | < 0.01 |
| <hr/> |     |     |        |     |     |        |
|       | HX  | 556 | 62,000 | 573 | 17  | 0.29   |
| AM8   | TOL | 556 | 60,000 | 578 | 22  | 0.28   |

|     |     |        |     |    |      |
|-----|-----|--------|-----|----|------|
| CF  | 558 | 63,000 | 578 | 20 | 0.30 |
| EA  | 549 | 57,000 | 572 | 23 | 0.27 |
| MC  | 555 | 56,000 | 573 | 18 | 0.30 |
| ACN | 554 | 58,000 | 573 | 19 | 0.26 |

Table 4.2 Ground state and excited state dipole moment of photosensitizers

|   | AM2    | AM5    | AM6    | AM7    | AM8    |
|---|--------|--------|--------|--------|--------|
| Ground state dipole moment ( $\mu_g$ ) [D] <sup>a</sup> | 9.59   | 10.26  | 11.30  | 11.52  | 7.88   |
| Onsager cavity radius[Å] <sup>a</sup>                   | 5.16   | 5.24   | 5.32   | 5.40   | 4.79   |
| S <sup>b</sup>  | 11,292 | 12,090 | 13,037 | 14,410 | 255    |
| (R <sup>2</sup> )                                       | (0.99) | (0.92) | (0.97) | (0.84) | (0.11) |
| $\Delta\mu$ [D] <sup>c</sup>                            | 12.39  | 12.82  | 13.67  | 15.00  | 1.67   |
| Excited state dipole moment ( $\mu_e$ ) [D]             | 21.98  | 23.08  | 24.98  | 26.52  | 9.55   |

<sup>a</sup> Ground state dipole moments and the onsager cavity radius were calculated by DFT/B3LYP (6-31G+ (d, p)) including the polarizable

continuum model (IEFPCM). <sup>b</sup>The slope of Lippert-Mataga plot, <sup>c</sup> the dipole moment changes between excited state and ground state calculated by Lippert-Mataga formulation (eqn 4.4).

### 4.3.3 Singlet oxygen quantum yield (SOQY)

The triplet generation of the photosensitizers was assessed through the generation of singlet oxygen (SOQY). The SOQYs of AM2, AM5, AM6, AM7, and AM8 in toluene were 0.32, 0.66, 0.70, 0.74, and 0.49, respectively (Figures 4.3, 4.4, and Table 4.5). AM2 does not have any heavy atoms; therefore, the generation of singlet oxygen is only attributed to PET, and because AM8 is not a D-A structure, the generation of singlet oxygen is attributed to the HAE. The SOQYs of AM5–8 were higher than those of AM2 and AM8, as we proposed. Notably, the SOQYs of AM5–8 were significantly higher than those of AM8, even though the number of bromine atoms in AM5–8 was less than that in AM8. These results may indicate the synergistic effect of PET and HAE. In addition, SOQY tends to increase with an increase in the number of bromine atoms, which could be because the introduction of additional bromine atoms increases the HAE as well as the PET. On

the other hand, the SOQYs of AM2, AM5, AM6, and AM7 in dichloromethane (MC) were 0.05, 0.16, 0.20, and 0.05, respectively, which were lower than those of the SOQYs in toluene (Figure 4.5). This might be because charge recombination from the  $^1\text{CT}$  to the  $\text{S}_0$  state was favorable in highly polar solvents. The  $^1\text{CT}$  state can become highly stabilized in polar solvents, leading to increased rates of charge recombination [17, 18]. For AM8, the SOQYs in MC were almost similar to those in toluene because PET was not allowed.

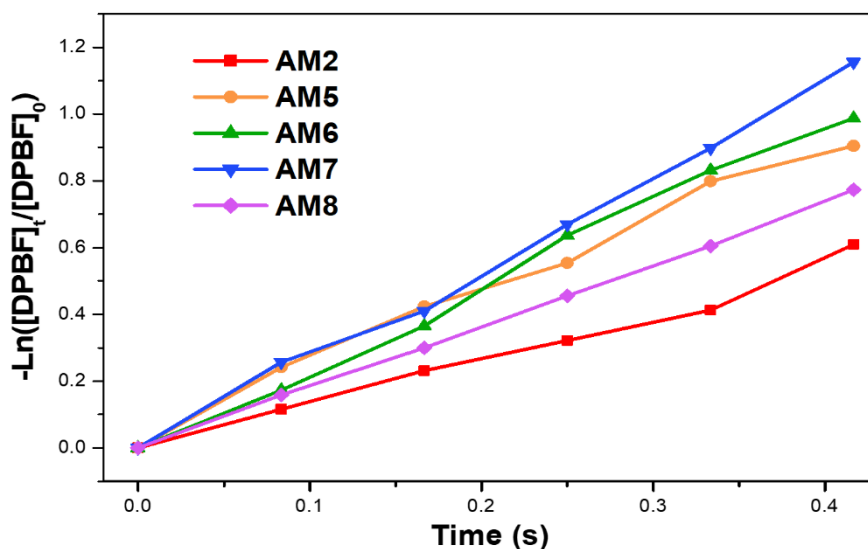


Figure 4.3 Time dependence of  $\ln([\text{DPBF}]_t/[\text{DPBF}]_0)$  in mixtures with Photosensitizers and DPBF under toluene (505nm laser excitation).

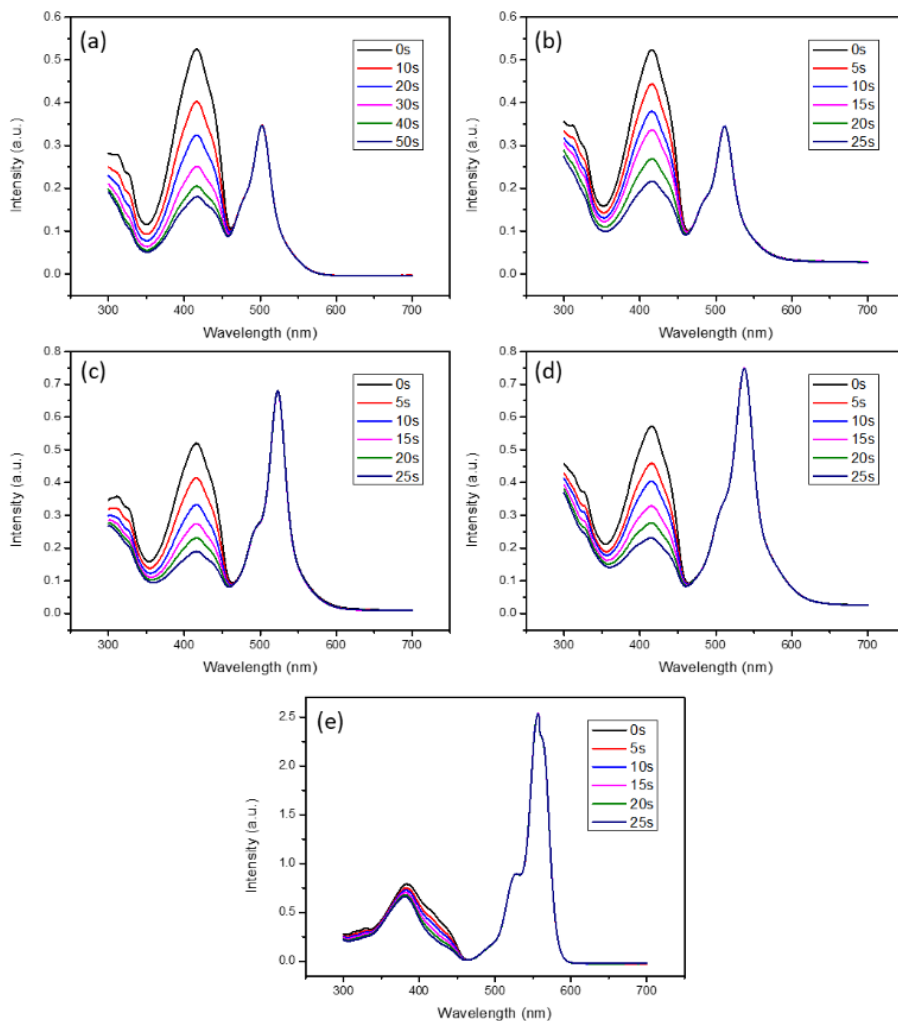


Figure 4.4 Determination of singlet oxygen quantum yield of AM2 (a), AM5 (b), AM6 (c), AM7 (d), and AM8 (e) photosensitizers in toluene (absorbance at 505nm = 0.3)

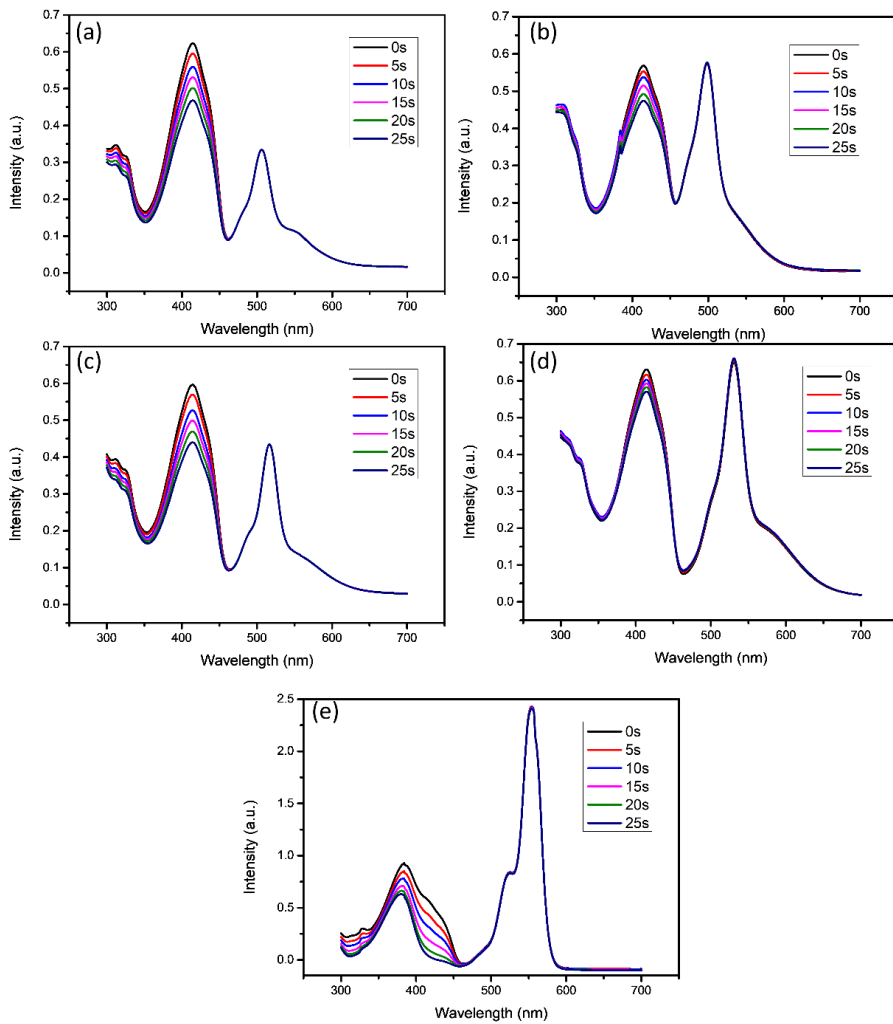


Figure 4.5 Determination of singlet oxygen quantum yield of AM2 (a), AM5 (b), AM6 (c), AM7 (d), and AM8 (e) photosensitizers in dichloromethane (absorbance at 505nm = 0.3)

### 4.3.4 Electrochemical properties

The redox potentials of the photosensitizers AM2–AM8, triphenylamine (TPA), and BODIPY (BDP) in dichloromethane were obtained by cyclic voltammetry (Figure 4.6), and the results are summarized in Table 4.3. The photosensitizers AM2–AM7 exhibited a one-electron reversible oxidation process on the positive potential side, which was attributed to the TPA moiety in comparison with the oxidation wave of the pristine TPA.

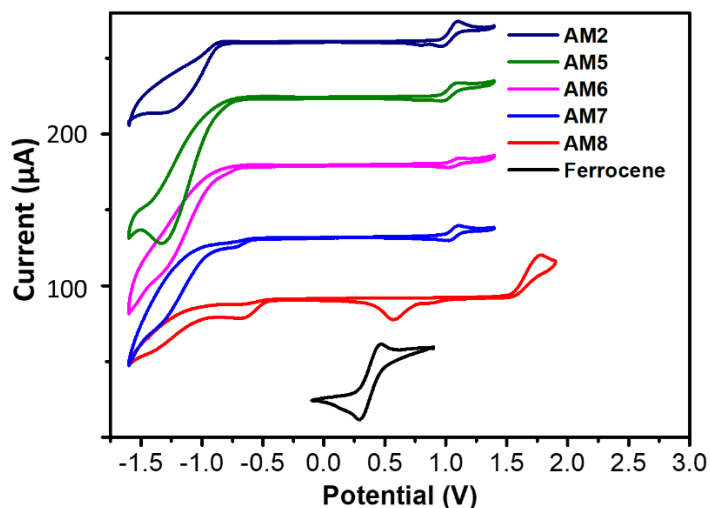


Figure 4.6 Cyclic voltammograms of AM2–AM8 (0.1 mM) in dichloromethane containing 0.10 M Bu<sub>4</sub>N[PF<sub>6</sub>] as the supporting electrolyte, and Ag/AgCl as the reference electrode. Scan rates: 50 mV/s. Ferrocene (Fc) was used as the external reference [ $E_{1/2} = +0.38$

V (Fc<sup>+</sup>/Fc)].

On the other hand, irreversible reduction waves were observed for all the photosensitizers on the negative potential sides. For AM2, the first electron reduction potential was observed at  $-0.77$  V, which may be attributed to the reduction of the pristine BDP unit, supported by the CV curve of the reference BDP moiety (Figure 4.7).

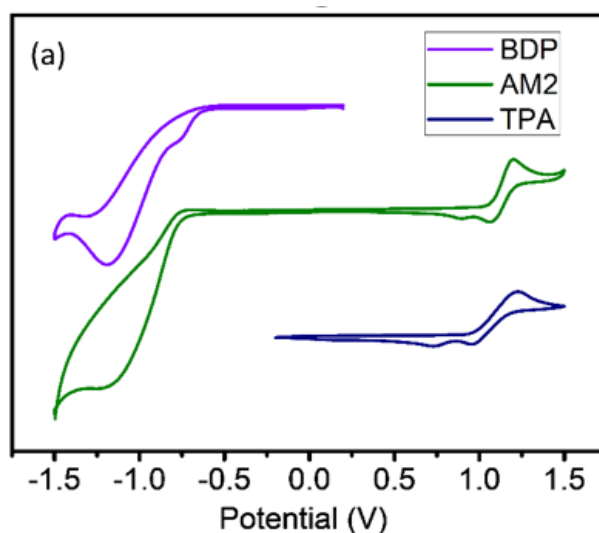


Figure 4.7 Cyclic voltammogram of AM2, triphenylamine (TPA), BODIPY (BDP) moiety.

In addition, the first reduction potentials increased in the following order: AM2 ( $-0.77$  V) < AM5 ( $-0.74$  V) < AM6 ( $-0.69$  V) < AM7 ( $-0.59$  V) < AM8 ( $-0.48$  V). This trend was attributed to bromine atoms acting on the BODIPY core as electron-withdrawing groups, and thus inducing

conjugated molecules to accept an electron more readily.

Table 4.3 Oxidation ( $E_{OX}$ ) and reduction ( $E_{RED}$ ) potential, charge separation driving force ( $\Delta G_{CS}$ ), reorganization energy ( $\lambda$ ), and Franck–Condon weighted density of states (FCWD)

|     | $E_{OX}$ (V) <sup>a</sup> |       | $E_{RED}$ (V) <sup>b</sup> |       | $\Delta G_{CS}$ (eV) <sup>c</sup> |      | $\lambda$ (eV) |      | FCWD |    |
|-----|---------------------------|-------|----------------------------|-------|-----------------------------------|------|----------------|------|------|----|
|     | TOL                       | MC    | TOL                        | MC    | TOL                               | MC   | TOL            | MC   | TOL  | MC |
| AM2 | 0.98                      | -0.77 | -0.21                      | -0.87 | 0.26                              | 0.63 | 3.22           | 1.60 |      |    |
| AM5 | 0.98                      | -0.74 | -0.23                      | -0.86 | 0.27                              | 0.62 | 3.74           | 1.66 |      |    |
| AM6 | 0.99                      | -0.69 | -0.24                      | -0.84 | 0.27                              | 0.65 | 3.91           | 1.92 |      |    |
| AM7 | 1.02                      | -0.60 | -0.26                      | -0.85 | 0.25                              | 0.59 | 3.92           | 0.91 |      |    |
| AM8 | 1.56                      |       | -0.48                      |       | -                                 | -    |                |      |      |    |

<sup>a</sup> The first oxidation onset potential and <sup>b</sup> the first reduction onset potential determined by the cyclic-voltammetry in dichloromethane.

The rate of photoinduced electron transfer is proportional to the Franck–Condon weighted density of states (FCWD), which is expressed by

$$FCWD = \frac{1}{\sqrt{4\pi\lambda k_B T}} \times \exp\left[-\frac{(\lambda + \Delta G_{CS})^2}{4\pi\lambda k_B T}\right] \quad \text{Eqn. 4.6}$$

where  $\lambda$  and  $\Delta G_{CS}$  are reorganization energy and Gibbs free energy changes of charge separation. The  $\Delta G_{CS}$  was obtained through the Rehm-Weller equation (eqn. 4.7).

$$\Delta G_{CS} = e[E_{OX} - E_{RED}] - E_{00} + \Delta G_S \quad \text{eqn. 4.7}$$

$$\Delta G_S = -\frac{e^2}{4\pi\epsilon_s\epsilon_0 R_{CC}} - \frac{e^2}{8\pi\epsilon_0} \left( \frac{1}{R_D} + \frac{1}{R_A} \right) \left( \frac{1}{\epsilon_{REF}} + \frac{1}{\epsilon_s} \right) \quad \text{eqn. 4.8}$$

where  $E_{OX}$  and  $E_{RED}$  are the first oxidation and reduction onset potentials, respectively, determined by cyclic voltammetry,  $E_{00}$  is the energy of the lowest excited state,  $\Delta G_S$  is the static coulombic energy,  $e$  is the elementary charge,  $\epsilon_s$  is the static dielectric constant of the solvent,  $\epsilon_0$  is the vacuum permittivity, and  $R_{CC}$  is the center-to-center distance between the electron donor (TPA) and the electron acceptor (BDP including bromine).  $R_D$  and  $R_A$  are the radii of the electron donor (TPA) and the acceptor unit (BDP including bromine), respectively, obtained from DFT optimization (DFT/B3LYP/6-31+G (d, p)). The  $R_{CC}$  values of AM2, AM5, AM6, and AM7 were 7.57, 7.59, 7.62, and 7.61 Å, respectively. The reorganization energy ( $\lambda$ ) of charge separation was evaluated by the arithmetic average of the forward ( $\lambda_1$ ) and backward ( $\lambda_2$ ) reorganization energy using DFT calculation, which was expressed by the Eqn. 4.9.

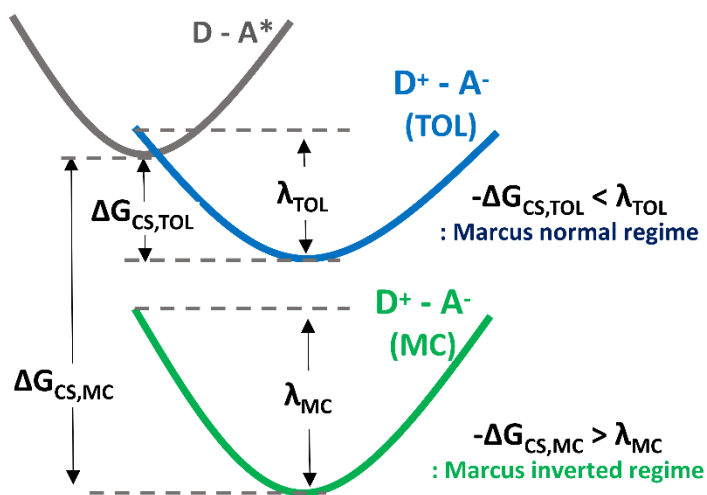
$$\begin{aligned} \lambda_1 &= E(D^+|D) - E(D^+|D^+) + E(A^-|A^*) - E(A^-|A^-) \\ \lambda_2 &= E(D|D^+) - E(D|D) + E(A^*|A^-) - E(A^*|A^*) \end{aligned} \quad \text{eqn. 4.9}$$

where the symbolization  $E(X|Y)$  denotes that the single point energy of the X state at the Y geometry. The  $\lambda_1$  and  $\lambda_2$  were determined by the sum of the reorganization energy of the donor and the acceptor

independently. [19-23]

In toluene, the  $-\Delta G_{CS}$  increased in the order  $AM2 < AM5 < AM6 < AM7$ , representing that the ability of charge separation tentatively increased from AM2 to AM7. The  $\lambda$  of AM2, AM5, and AM6 were 0.26, 0.27, and 0.27 respectively, which was higher than the  $-\Delta G_{CS}$ . This indicates that the charge separation occurs in the Marcus normal regime (Scheme 4.2). For AM7, the  $-\Delta G_{CS}$  was slightly higher than the  $\lambda$ , corresponding to the Marcus inverted region. In addition, the value of  $(\lambda + \Delta G_{CS})$  became close to zero with increasing the number of bromines, resulting in the increased the FCWD. This clearly shows that the degree of charge separation increased with increasing the number of bromine atoms. On the other hand, in MC, no significant correlation was observed between the  $-\Delta G_{CS}$  and the number of bromine atoms, and the charge separation occurs in the Marcus inverted regime, because  $-\Delta G_{CS}$  was higher than the  $\lambda$ . In addition, the value of  $(\lambda + \Delta G_{CS})$  in AM2-AM7 was large, so the FCWD in MC was low compared to that in toluene. This result means that the charge separation is relatively unfavorable in the MC, and as a result, the SOQY appears to be small. Although the driving force of all the photosensitizers in MC was higher than that in toluene, the charge separation in toluene may be more favorable than that in MC. This is

because the charge separation state in MC was located in the Marcus inverted region owing to the large charge separation driving force. Thus, this may be another factor that reduced the SOQY in dichloromethane along with charge recombination.



Scheme 4.2 Schematic representation of photoinduced electron transfer in toluene (TOL) and dichloromethane (MC)

#### 4.3.5 Triplet lifetime ( $\tau_T$ )

Time-resolved photoluminescence experiments at emission maxima wavelength were carried out to investigate the triplet lifetime of AM2–9 (Figure 4.8). All the samples showed a biexponential decay profile. A

fast component was assigned to a shortened decay by  $O_2$  because the decay curve of a fast component in a deaerated environment coincides with that in an aerated environment (Figure 4.9).

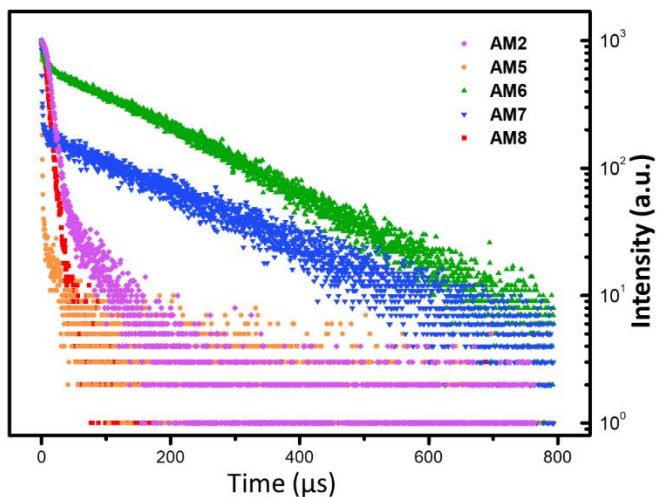


Figure 4.8 Phosphorescence decay curve of AM2-AM8 photosensitizers in deaerated toluene ( $10^{-5}M$ )

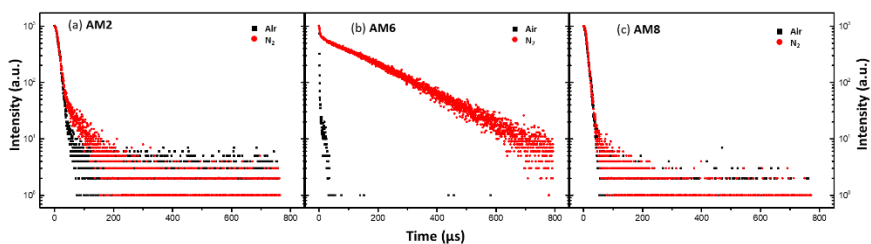


Figure 4.9 Phosphorescence decay curve of AM2, AM6 and AM8 photosensitizers in aerated and deaerated toluene ( $10^{-5}M$ )

The triplet lifetimes of the slow components of AM2, AM5, AM6, AM7,

and AM8 were 132, 122, 175, 199, and 57  $\mu\text{s}$ , respectively. AM8, which contains only heavy atoms, showed a short lifetime similar to the reported one (36  $\mu\text{s}$ ). This supported the findings of previous studies that the electrons of heavy atoms decay rapidly from  $T_1$  to  $S_0$  along the nonradiative pathway. [7] In contrast, D-A-H photosensitizers showed long triplet lifetimes. It is quite interesting that the triplet lifetimes of AM5, AM6, and AM7 were long despite the presence of heavy atoms. Although the triplet lifetime of AM5 was relatively short, those of AM6 and AM7, which contained heavy atoms, were longer than that of AM2, which did not contain heavy atoms. In addition, the triplet lifetime of the D-A-H photosensitizers increased with increasing number of bromine atoms. This is contrary to the results from previous studies, which showed an increase in SOQY and a decrease in triplet lifetime with increasing number of heavy atoms. [7] Therefore, this result indicated that increasing the number of heavy atoms in a D-A-H photosensitizer is a good strategy for improving its ISC yield as well as triplet lifetime.

## 4.3.6 Quantum chemical calculation

### 4.3.6.1 Overlap integral and spin density distribution

For a detailed understanding of the relationship between PET and SOQY, the orbital overlap between the HOMO and LUMO of the optimized  $S_1$  state was calculated using the overlap integral ( $S_r$ ) by Multiwfn.  $S_r$  is occasionally used in the field of OLED research as a parameter for quantifying the size of charge separation. [24, 25] The  $S_r$  values of AM2, AM5, AM6, and AM7 were 0.08328, 0.08158, 0.08133, and 0.07889, respectively, and gradually decreased as the number of bromine atoms increased (Table 4.5). Although there was no significant difference in the values of  $S_r$  of the photosensitizers, this trend is consistent with the results of the  $\Delta\mu_{ge}$  and the  $\Delta G_{CS}$  in the previous section. Overall, these results represent that an increase in the number of bromine enhances the charge separation. Notably, the  $S_r$  of AM8 was 0.64344, which is considerably higher than that of the other molecules. This significant difference in the orbital overlap can be intuitively confirmed by the visualized image (Figure 4.10), suggesting that PET does not occur in AM8.

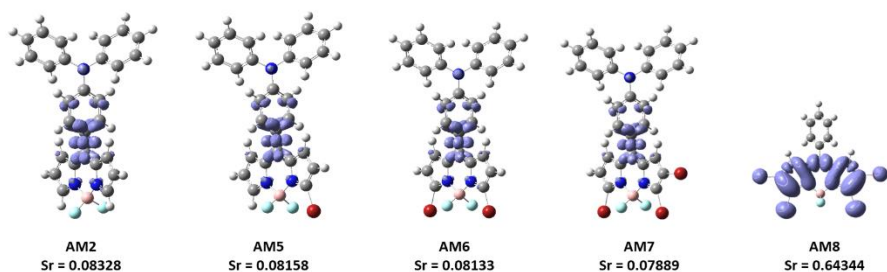


Figure 4.10 Overlap integrals (Sr) of AM2-9 photosensitizers. (S<sub>1</sub>)

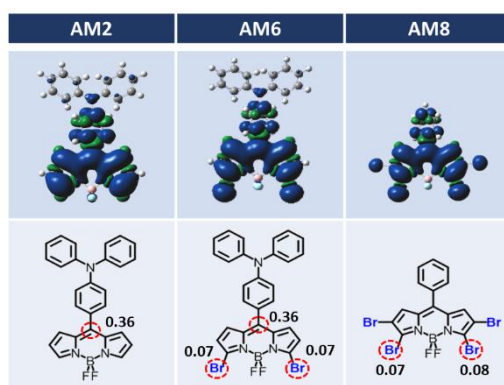


Figure 4.11 Spin density of AM2, AM6, and AM8 photosensitizers (optimized T<sub>1</sub> state)

To obtain deeper insights into the synergistic effect, the spin density distribution (SDD) in the optimized T<sub>1</sub> state of AM2, AM6, and AM8 was calculated by TDDFT/B3LYP/6-31+G (d, p). For AM2 and AM6, the spin was localized mainly in BODIPY, and for AM8, it was spread over the entire molecule (Figure 4.11). Zhao et al. reported that higher the spin density of the carbon atom at the meso position in BODIPY, larger the

ISC because of PET. [3] The spin density of carbon in AM2 and AM6 was 0.36 each. Although these are not consistent with the result of the  $\Delta\mu_{ge}$  and the  $\Delta G_{CS}$ , it indicates that the extent of PET in AM6 is similar to that in AM2. In addition, the spin density of bromine located at the end of BODIPY was 0.07 for AM6, which is similar to that for AM8. The spin density of a heavy atom is considered a parameter that determines HAE; therefore, this may indicate that HAE may have almost the same effect as that in case of AM8. [26] Therefore, based on the SDD results, it can be confirmed that AM6 showed HAE and PET simultaneously, which is a synergistic effect.

#### **4.3.6.2 Natural transition orbital (NTO) and Intersystemcrossing kinetics**

In order to evaluate the transition characteristics of the singlet and triplet excited states, the natural transition orbitals (NTO) and the energy levels of all the excited states participating in photochemical kinetics were also investigated. For all the photosensitizers, except AM8, the  $S_1$  and  $T_2$  states exhibited CT characteristics, and the  $S_2$  and  $T_1$  states exhibited LE characteristics (Figures 4.12 and 4.13).

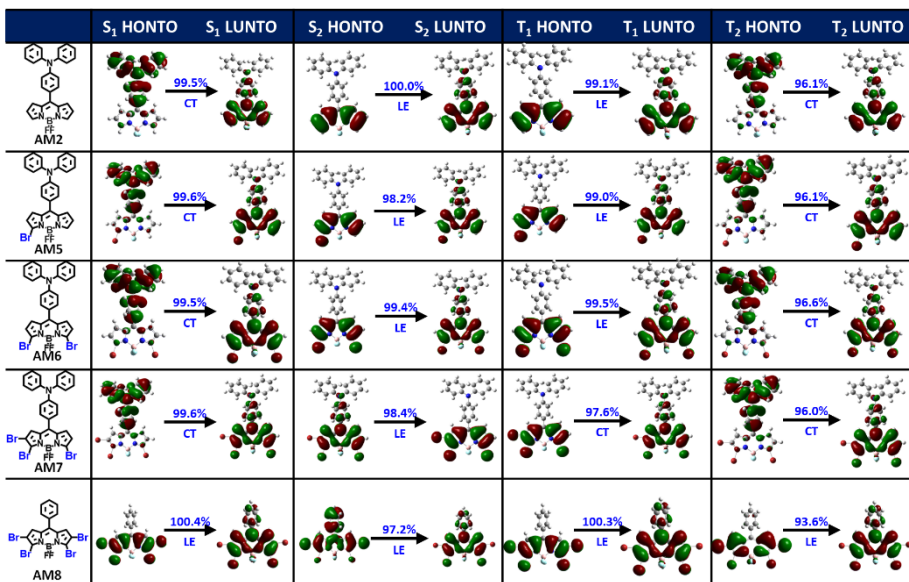


Figure 4.12 Highest occupied natural transition orbital (HONTO) and lowest unoccupied natural transition orbital (LUNTO) of AM2-AM8 photosensitizers (S<sub>1</sub>, S<sub>2</sub>, T<sub>1</sub>, and T<sub>2</sub> states)

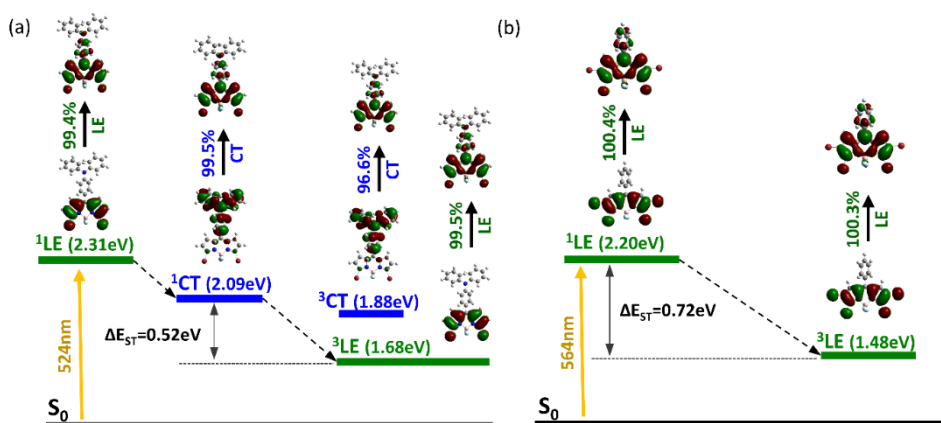


Figure 4.13. Schematic of the mechanism of intersystem crossing

between the excited singlet and triplet states.  $^1\text{LE}$  and  $^1\text{CT}$  states were determined by spectroscopic and cyclic voltammetric analyses. The triplet excited states were calculated by TDDFT/B3LYP/6-31+G (d, p). Natural transition orbitals (NTO) and their transition probabilities corresponding to the excited states are included.

The AM8 photosensitizer showed LE character in all the calculated states because PET did not occur in AM8. The excited-state energy levels of AM6 appeared in the order  $T_1$  (1.68 eV) <  $T_2$  (1.88 eV) <  $S_1$  (2.09 eV) <  $T_3$  (2.75 eV); AM2–AM7 also showed a similar order of energy levels. ISC from the  $S_1$  state to the  $T_3$  state was thermodynamically not allowed because the  $T_3$  state had higher energy than the  $S_1$  state. The SOCT-induced ISC (SOCT-ISC) would occur between the  $S_1$  and  $T_1$  states because the  $S_1$  and  $T_1$  states are assigned to the  $^1\text{CT}$  and  $^3\text{LE}$  states, respectively. According to Fermi's golden rule, the SOCT-ISC process is governed by the energy gap ( $\Delta E_{S_1-T_1}$ ) between the  $S_1$  and  $T_1$  states, and  $\Delta E_{S_1-T_1}$  was determined to slightly decrease from AM2 to AM7, which enhanced the SOCT-ISC.

In addition, the HFC-induced ISC (HFC-ISC) between the  $S_1$  and  $T_2$  states is valid, because both the  $S_1$  and  $T_2$  states have CT

characteristics. Similar to SOCT-ISC, HFC-ISC was determined by the energy gap ( $\Delta E_{S_1-T_2}$ ) between the  $S_1$  and  $T_2$  states. The  $\Delta E_{S_1-T_2}$  values of AM2–AM7 decreased marginally with increasing number of bromine atoms. Therefore, it is believed that HFC-ISC might increase from AM2 to AM7. However, the HFC may rarely contribute to the total ISC because an extremely small  $\Delta E_{ST}$  (20  $\mu\text{eV}$ ) is required to generate HFC-ISC. [27] On the other hand,  $\Delta E_{S_1-T_2}$  is identical to twice the electron exchange energy ( $J$ ), which is the constant of exchange interaction. The extent of  $J$  is influenced by of the overlap integral between orbitals with spin. [8] Thus, the  $J$  value can be compared with  $S_r$  in the previous section.  $J$  gradually decreased with increasing  $S_r$ , indicating that the increased PET by bromine decreased the overlap integral and therefore decreased  $J$  (Table 4.5). For AM8, the excited energy level was in the order  $T_1$  (1.48 eV) <  $S_1$  (2.20 eV) <  $T_2$  (2.61 eV); thus, ISC is only favorable between the  $S_1$  and  $T_1$  states. Although AM8 does not have PET characteristics, the SOC induced by HAE can encourage ISC. The  $\Delta E_{S_1-T_1}$  of AM8 was 0.72 eV, considerably larger than those of the other photosensitizers, and may lower ISC from the  $S_1$  to the  $T_1$  state.

### 4.3.6.3 Spin orbit coupling matrix element (SOCME)

The spin-orbit coupling matrix element (SOCME), calculated using ORCA software based on the optimized ground geometry (Figure 4.14, and Table 4.4) [28], is a key parameter that determines the magnitude of spin-orbit coupling, and thus provides important information on the dynamics of SOCT-ISC and HAE. The SOCME between  $S_1$  and  $T_1$  states was  $0.44 \text{ cm}^{-1}$  for AM8, indicating that the ISC of AM8 originated from the HAE induced SOC. On the other hand, AM2 exhibited an SOCME of  $0.57 \text{ cm}^{-1}$ , indicating that ISC was induced by spin-orbit charge transfer in AM2.

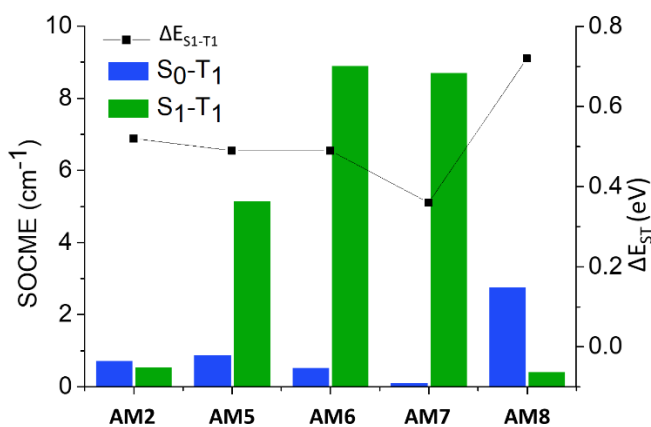


Figure 4.14 Spin-orbit coupling matrix element (SOCME) and energy gap ( $\Delta E_{S_1-T_1}$ ) between the  $S_1$  and  $T_1$  states of AM2–AM8.

The SOCME values of AM5, AM6, and AM7 were 5.18, 8.93, and 8.74  $\text{cm}^{-1}$  respectively, significantly higher than those of AM2 and AM8. Since this was identical to the trend of SOQY, it was postulated that ISC was mainly influenced by SOC, and not HFC. SOCME values between the  $S_1$  and  $T_2$  states for AM2–AM7 were relatively small, in the range from 0.00 to 0.16, which indicated that SOC did not occur properly because both the  $S_1$  and  $T_2$  states have CT characteristics. The SOCME between  $S_0$  and  $T_1$  correlated well with the triplet lifetime. In general, with increasing SOCME, the nonradiative decay from  $T_1$  to  $S_0$  became dominant, and as a result, the triplet lifetime decreased. The SOCME values of AM2, AM5, AM6, AM7, and AM8 were 0.76, 0.91, 0.56, 0.15, and 2.80  $\text{cm}^{-1}$ , respectively, and this trend was inversely correlated with the triplet lifetime.

Table 4.4 Spin orbit coupling matrix element (SOCME) and the energy gap between the excited singlet ( $S_n$ ) and triplet ( $T_m$ ) states.

|     |                           | SOCME                | $\Delta E_{S_n-T_m}$ |
|-----|---------------------------|----------------------|----------------------|
|     |                           | ( $\text{cm}^{-1}$ ) | (eV)                 |
|     | $S_0 \leftrightarrow T_1$ | 0.76                 | 1.68                 |
| AM2 | $S_1 \leftrightarrow T_1$ | 0.57                 | 0.52                 |
|     | $S_1 \leftrightarrow T_2$ | 0.03                 | 0.33                 |

|     |                           |      |      |
|-----|---------------------------|------|------|
|     | $S_0 \leftrightarrow T_1$ | 0.91 | 1.64 |
| AM5 | $S_1 \leftrightarrow T_1$ | 5.18 | 0.49 |
|     | $S_1 \leftrightarrow T_2$ | 0.16 | 0.28 |
|     | $S_0 \leftrightarrow T_1$ | 0.56 | 1.60 |
| AM6 | $S_1 \leftrightarrow T_1$ | 8.93 | 0.49 |
|     | $S_1 \leftrightarrow T_2$ | 0.00 | 0.28 |
|     | $S_0 \leftrightarrow T_1$ | 0.15 | 1.59 |
| AM7 | $S_1 \leftrightarrow T_1$ | 8.74 | 0.36 |
|     | $S_1 \leftrightarrow T_2$ | 0.10 | 0.21 |
|     | $S_0 \leftrightarrow T_1$ | 2.80 | 1.48 |
| AM8 | $S_1 \leftrightarrow T_1$ | 0.44 | 0.72 |

In particular, AM8 showed the highest SOCME, which resulted in the shortest triplet lifetime. On the other hand, the SOCME ( $S_0-T_1$ ) values of AM5–AM7 were reduced, even though they contained heavy atoms. The synergistic effect of PET and HAE lowered SOCME ( $S_0-T_1$ ) and selectively increased only SOCME ( $S_1-T_1$ ), which may result in shortened triplet lifetime and increased ISC yield.

#### **4.3.6.4 Triplet-triplet annihilation upconversion (TTA-UC)**

TTA-UC, which generates anti-Stokes emission, is generally achieved by molecular energy transfer between two different organic molecules, a sensitizer and an annihilator. Here, the triplet sensitizer plays an important role in generating the triplet annihilator by absorbing photons, being excited, and transferring energy to the annihilator. Therefore, the triplet feature of the sensitizer largely affects the overall UC emission efficiency of TTA-UC. Although porphyrin-based photosensitizers have been widely studied in TTA-UC, we employed AM2–9 photosensitizers as triplet sensitizers in TTA-UC and investigated their photochemical properties.

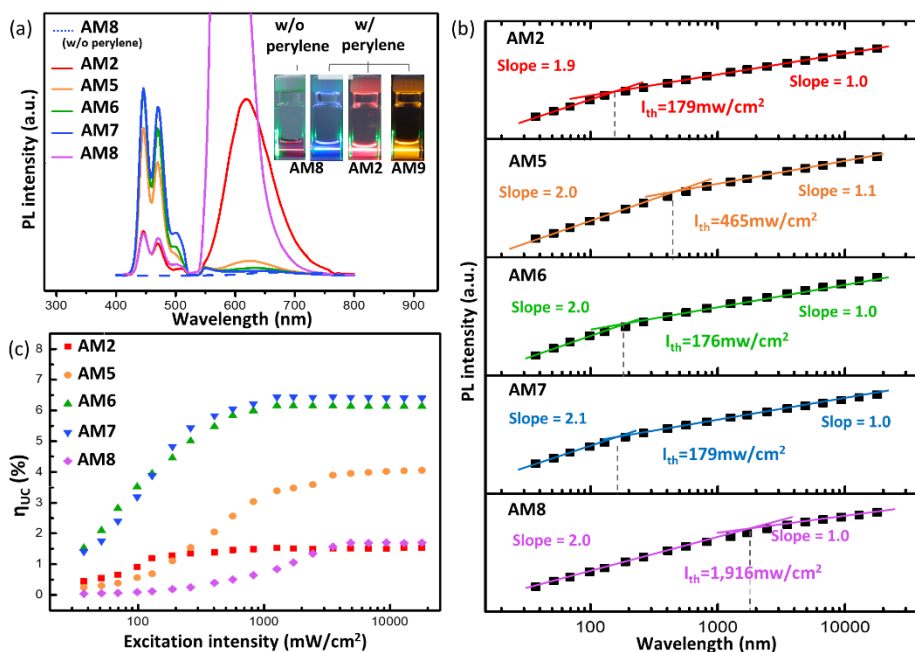


Figure 4.15 (a) TTA-UC photoluminescence spectra of AM2–9 (inset) photographs of emission in upconversion system. (b) Upconversion intensity (log scale) and (c) upconversion emission efficiencies of AM2–9 (sensitizer: 20 $\mu\text{M}$ , annihilator: 32 $\mu\text{M}$ ) as a function of incident laser power density ( $\text{mW}/\text{cm}^2$ )

Perylene was selected as a triplet annihilator because of its superior fluorescence quantum yield, and all measurements were performed in deaerated toluene using a 532 nm laser as a light source to achieve typical green-to-blue upconversion. The sensitizer and perylene concentrations were optimized to 20  $\mu\text{M}$  and 32  $\mu\text{M}$ , respectively, based

on the preliminary UC intensity measurements (Figure 4.16) using AM7.

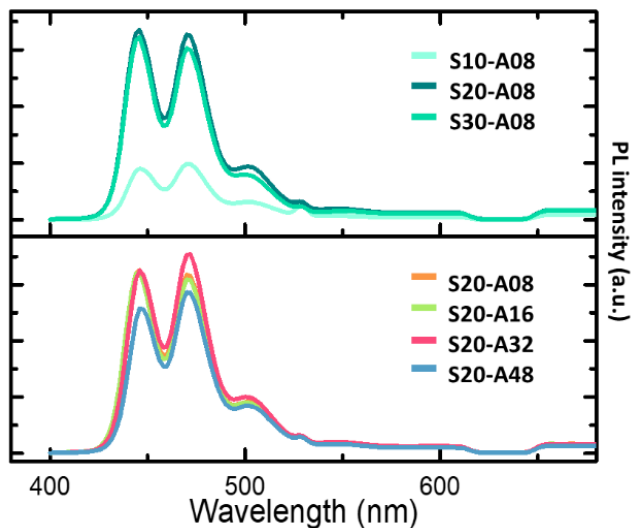


Figure 4.16 Upconversion emission spectra in different concentration of AM7(photosensitizer) and perylene (annihilator) for obtaining optimized condition. The concentrations of sensitizer and perylene were selected as 10, 20, 30 $\mu$ M and 8, 16, 32, 48 $\mu$ M respectively.

When a 532 nm laser (4.9 W/cm<sup>2</sup>) was irradiated onto the UC solution, upconverted blue emission (430–500 nm), attributed to delayed fluorescence of perylene, was clearly visible in all samples, along with spectral measurement, although there was a clear difference in UC intensity according to the type of sensitizer (Figure 4.15a).

Note that the AM7 solution, not including perylene (the leftmost picture in Figure 4.15a), shows down-shifted red fluorescence. Moreover, UC

intensity appeared in the order of AM7>AM6>AM5>AM8>AM2, which is consistent with the result of SOQY, demonstrating the triplet synergistic effect of AM5–8 photosensitizers. (Table 4.5)

To further characterize TTA-UC properties, UC emission efficiency ( $\eta_{UC}$ ) and UC intensities were measured by varying the laser excitation power (Figure 4.15b and c).

Table 4.5 Overlap integral (Sr), electron exchange energy (J), singlet oxygen quantum yield ( $\Phi_{\Delta}$ ), and triplet lifetime ( $\tau_T$ ), upconversion emission efficiency ( $\eta_{UC}$ ), and threshold intensity ( $I_{th}$ ) of AM2–9 photosensitizers under excitation at 532nm

|     | Sr <sup>a</sup> | J (eV) <sup>b</sup> | $\Phi_{\Delta}$                          | $\tau_T^c$ ( $\mu$ s) | $\eta_{UC}^e$ | $I_{th}$<br>(mW/cm <sup>2</sup> ) <sup>c</sup> |
|-----|-----------------|---------------------|--|-----------------------|---------------|--|
| AM2 | 0.08328         | 0.17                | 0.32 <sup>c</sup> ,<br>0.05 <sup>d</sup> | 132                   | 0.015         | 179  |
| AM5 | 0.08158         | 0.14                | 0.66 <sup>c</sup> ,<br>0.16 <sup>d</sup> | 122                   | 0.039         | 465  |
| AM6 | 0.08133         | 0.14                | 0.70 <sup>c</sup> ,<br>0.20 <sup>d</sup> | 175                   | 0.062         | 176  |
| AM7 | 0.07889         | 0.11                | 0.74 <sup>c</sup> ,<br>0.05 <sup>d</sup> | 199                   | 0.065         | 179  |
| AM8 | 0.64344         | -                   | 0.49 <sup>c</sup> ,<br>0.55 <sup>d</sup> | 57                    | 0.017         | 1,916  |

<sup>a</sup> Overlap integral was obtained from the natural transition orbital of S1 state. <sup>b</sup>

Electron exchange integral was determined by the energy difference between  $^1\text{CT}$  and  $^3\text{CT}$  states. In <sup>c</sup> toluene and <sup>d</sup> dichloromethane. <sup>e</sup> Upconversion emission efficiency was determined in toluene using a 532 nm laser (4.9 W/cm<sup>2</sup>)

As the laser power increased, the UC emission efficiency of all the solutions increased and then plateaued. The highest UC emission efficiency (6.5%) was obtained for the AM7 solution. Although higher levels of UC emission efficiency have been reported in porphyrin-based TTA-UC, [29, 30] this is close to the UC emission efficiency of iodine BODIPY photosensitizers, which showed the highest UC emission efficiency in toluene among BODIPY-based sensitizers. [31]

In the plot of UC intensity versus laser power density (Figure 4.15b), clear quadratic (at low power density, slope=2) to linear (at high power density, slope=1) power dependency was observed for all UC solutions, which is a typical feature of TTA-UC. [32-33] Meanwhile, the effectiveness of TTA-UC is also evaluated by the threshold intensity ( $I_{\text{th}}$ ), which is the laser power density at the point where these quadratic-to-linear correlations intersect. That is, for lower values of  $I_{\text{th}}$  value, the triplet annihilator is more rapidly generated, and the generated excited triplet annihilators are consumed by TTA, not by unimolecular decay. The  $I_{\text{th}}$  values of UC solutions containing AM2, AM5, AM6, AM7, and

AM8 were 179, 465, 176, 179, and 1,916 mW/cm<sup>2</sup>, respectively. Interestingly, the  $I_{th}$  values of the UC solutions containing D-A sensitizers (AM2, AM5, AM6, and AM7) were low, whereas that of the UC solution without the D-A sensitizer (AM8) was exceptionally high. Because the  $I_{th}$  is mainly determined by the triplet energy transfer efficiency from the sensitizer to the annihilator, [34] this difference is attributed to the increased triplet lifetime of the sensitizer because of the introduction of a donor molecule. These results clearly indicate that D-A coupled with heavy atoms reduces the high  $I_{th}$  of heavy atom photosensitizers.

#### **4.4 Conclusion**

In summary, we reported a novel approach for triplet photosensitizers comprising triphenylamine (D)-BODIPY (A)-bromine (H), and demonstrated that merging D-A molecules with heavy atoms drove the synergistic effect of PET and HAE, contributing to enhanced triplet characteristics such as SOQY and triplet lifetime. Moreover, the TTA-UC study showed that D-A-H photosensitizers achieved high upconversion emission efficiency and low  $I_{th}$  compared with standards (D-A and heavy atom photosensitizers). However, it was not possible to obtain excellent

triplet characteristics because the study was only focused on photosensitizers consisting of triphenylamine-BODIPY-bromine. Therefore, D-A-H photosensitizers with various donors, acceptor, and heavy atoms may achieve more improved triplet quantum yield, triplet lifetime, and upconversion properties.

## **4.5 References**

- [1] Zhao J, Wu W, Sun J, Guo S. Triplet photosensitizers: from molecular design to applications. *Chemical Society Reviews*. 2013;42(12):5323-51.
- [2] Hou Y, Biskup T, Rein S, Wang Z, Bussotti L, Russo N, et al. Spin–Orbit Charge Recombination Intersystem Crossing in Phenothiazine–Anthracene Compact Dyads: Effect of Molecular Conformation on Electronic Coupling, Electronic Transitions, and Electron Spin Polarizations of the Triplet States. *The Journal of Physical Chemistry C*. 2018;122(49):27850-65.
- [3] Hou Y, Kurganskii I, Elmali A, Zhang H, Gao Y, Lv L, et al. Electronic coupling and spin–orbit charge transfer intersystem crossing (SOCT-ISC) in compact BDP–carbazole dyads with

different mutual orientations of the electron donor and acceptor.

The Journal of Chemical Physics. 2020;152(11):114701.

[4] Ke M-R, Yeung S-L, Ng DKP, Fong W-P, Lo P-C. Preparation and in Vitro Photodynamic Activities of Folate-Conjugated Distyryl Boron Dipyrromethene Based Photosensitizers. Journal of Medicinal Chemistry. 2013;56(21):8475-83.

[5] Lee JM, Kang S, Hwang TG, Kim HM, Lee WS, Kim D, et al. A study on photophysical and photodynamic properties of donor–acceptor BODIPY complexes: Correlation between singlet oxygen quantum yield and singlet-triplet energy gap. Dyes and Pigments. 2021;187:109051.

[6] Wang Z, Ivanov M, Gao Y, Bussotti L, Foggi P, Zhang H, et al. Spin–Orbit Charge-Transfer Intersystem Crossing (ISC) in Compact Electron Donor–Acceptor Dyads: ISC Mechanism and Application as Novel and Potent Photodynamic Therapy Reagents. Chemistry – A European Journal. 2020;26(5):1091-102.

[7] Zhang X-F, Yang X. Singlet Oxygen Generation and Triplet Excited-State Spectra of Brominated BODIPY. The Journal of Physical Chemistry B. 2013;117(18):5533-9.

- [8] Turro NJ, Ramamurthy V, Scaiano JC. Modern molecular photochemistry of organic molecules: Viva Books University Science Books, Sausalito, 2017.
- [9] Gibbons DJ, Farawar A, Mazzella P, Leroy-Lhez S, Williams RM. Making triplets from photo-generated charges: observations, mechanisms and theory. *Photochemical & Photobiological Sciences*. 2020;19(2):136-58.
- [10] Chen X-K, Kim D, Brédas J-L. Thermally Activated Delayed Fluorescence (TADF) Path toward Efficient Electroluminescence in Purely Organic Materials: Molecular Level Insight. *Accounts of Chemical Research*. 2018;51(9):2215-24.
- [11] Lee Jm, Yuk Sb, Namgoong Jw, Kim Jp. Mechanofluorochromism of Triphenylamine-BODIPY: Effect of twisted intramolecular charge transfer and restriction in rotation on fluorescence. *Dyes and Pigments*. 2021;185:108864.
- [12] Lu T, Chen F. Multiwfn: a multifunctional wavefunction analyzer. *Journal of computational chemistry*. 2012;33(5):580-92.
- [13] Li X, Liang Z, Wang H, Qiao S, Liu Z, Jiang H, et al. Fluorinated D1(0.5)-A-D2(0.5)-A model terpolymer: ultrafast charge separation kinetics and electron transfer at the fluorinated D/A

interface for power conversion. *Journal of Materials Chemistry A*. 2020;8(3):1360-7.

[14] Wang Y, Hasegawa T, Matsumoto H, Mori T, Michinobu T. Rational Design of High-Mobility Semicrystalline Conjugated Polymers with Tunable Charge Polarity: Beyond Benzobisthiadiazole-Based Polymers. *Advanced Functional Materials*. 2017;27(2):1604608.

[15] Carsten B, Szarko JM, Son HJ, Wang W, Lu L, He F, et al. Examining the Effect of the Dipole Moment on Charge Separation in Donor–Acceptor Polymers for Organic Photovoltaic Applications. *Journal of the American Chemical Society*. 2011;133(50):20468-75.

[16] Masuhara N, MTOH. *Dynamics and Mechanisms of Photoinduced Electron Transfer and Related Phenomena*: North-Holland, 1992.

[17] Epelde-Elezcano N, Palao E, Manzano H, Prieto-Castañeda A, Agarrabeitia AR, Tabero A, et al. Rational Design of Advanced Photosensitizers Based on Orthogonal BODIPY Dimers to Finely Modulate Singlet Oxygen Generation. *Chemistry – A European Journal*. 2017;23(20):4837-48.

- [18] Filatov MA. Heavy-atom-free BODIPY photosensitizers with intersystem crossing mediated by intramolecular photoinduced electron transfer. *Organic & Biomolecular Chemistry*. 2020;18(1):10-27.
- [19] Ceroni P. The exploration of supramolecular systems and nanostructures by photochemical techniques: Springer Science & Business Media, 2011.
- [20] Iagatti A, Cupellini L, Biagiotti G, Caprasecca S, Fedeli S, Lapini A, et al. Efficient Photoinduced Charge Separation in a BODIPY–C60 Dyad. *The Journal of Physical Chemistry C*. 2016;120(30):16526-36.
- [21] López X, Carbó JJ, Bo C, Poblet JM. Structure, properties and reactivity of polyoxometalates: a theoretical perspective. *Chemical Society Reviews*. 2012;41(22):7537-71.
- [22] López X, Fernández JA, Poblet JM. Redox properties of polyoxometalates: new insights on the anion charge effect. *Dalton Transactions*. 2006(9):1162-7.
- [23] Toupalas G, Karlsson J, Black FA, Masip-Sánchez A, López X, Ben M'Barek Y, et al. Tuning Photoinduced Electron Transfer in

POM-Bodipy Hybrids by Controlling the Environment: Experiment and Theory. *Angewandte Chemie*. 2021;133(12):6592-9.

[24] Chen T, Zheng L, Yuan J, An Z, Chen R, Tao Y, et al. Understanding the Control of Singlet-Triplet Splitting for Organic Exciton Manipulating: A Combined Theoretical and Experimental Approach. *Scientific Reports*. 2015;5(1):10923.

[25] Mamada M, Inada K, Komino T, Potscavage WJ, Nakanotani H, Adachi C. Highly Efficient Thermally Activated Delayed Fluorescence from an Excited-State Intramolecular Proton Transfer System. *ACS Central Science*. 2017;3(7):769-77.

[26] Schott S, McNellis ER, Nielsen CB, Chen H-Y, Watanabe S, Tanaka H, et al. Tuning the effective spin-orbit coupling in molecular semiconductors. *Nature Communications*. 2017;8(1):15200.

[27] Ogiwara T, Wakikawa Y, Ikoma T. Mechanism of Intersystem Crossing of Thermally Activated Delayed Fluorescence Molecules. *The Journal of Physical Chemistry A*. 2015;119(14):3415-8.

[28] Neese F. Software update: the ORCA program system, version 4.0. *WIREs Computational Molecular Science*. 2018;8(1):e1327.

- [29] Khnayzer RS, Blumhoff J, Harrington JA, Haefele A, Deng F, Castellano FN. Upconversion-powered photoelectrochemistry. *Chemical Communications*. 2012;48(2):209-11.
- [30] Yonemura H, Naka Y, Nishino M, Sakaguchi H, Yamada S. Switch of the magnetic field effect on photon upconversion based on sensitized triplet–triplet annihilation. *Photochemical & Photobiological Sciences*. 2016;15(12):1462-7.
- [31] Zhou Q, Zhou M, Wei Y, Zhou X, Liu S, Zhang S, et al. Solvent effects on the triplet–triplet annihilation upconversion of diiodo-Bodipy and perylene. *Physical Chemistry Chemical Physics*. 2017;19(2):1516-25.
- [32] Kim J-H, Deng F, Castellano FN, Kim J-H. Red-to-Blue/Cyan/Green Upconverting Microcapsules for Aqueous- and Dry-Phase Color Tuning and Magnetic Sorting. *ACS Photonics*. 2014;1(4):382-8.
- [33] Kim J-H, Kim J-H. Triple-Emulsion Microcapsules for Highly Efficient Multispectral Upconversion in the Aqueous Phase. *ACS Photonics*. 2015;2(5):633-8.

[34] Bharmoria P, Bildirir H, Moth-Poulsen K. Triplet–triplet annihilation based near infrared to visible molecular photon upconversion. *Chemical Society Reviews*. 2020;49(18):6529-54.

## **Chapter 5**

# **Enhanced triplet-triplet annihilation upconversion luminescence through the conformational restriction based on donor - acceptor - heavy atom molecules**

### **5.1 Introductions**

Although numerous studies on the TTA-UC system that can be implemented at low power with high efficiency have been reported, the power density and upconversion emission efficiency is still required to be improved for commercialization. In order to improve upconversion properties, it is necessary to develop excellent triplet sensitizers and annihilators, which are components of the TTA-UC system. There are a variety of commercially available annihilators with high fluorescence quantum yield, but triplet photosensitizers have not yet been optimized. The study of triplet photosensitizer is mainly focused on increasing intersystemcrossing (ISC) yield, because the ISC from excited singlet to

triplet states of organic chromophore is forbidden. [1-3] However, little attention has been paid to the triplet lifetime ( $\tau_T$ ), although it is known that enlarged  $\tau_T$  can increase triplet-triplet energy transfer ( $\Phi_{TTET}$ ) yield and thus improve UC emission efficiency and threshold intensity ( $I_{th}$ ).  $\tau_T$  is determined by the radiative or nonradiative decay from the T1 state to the S0 state, and the nonradiative decay may be promoted by the molecular vibration or rotation. In the research field of room temperature phosphorescence (RTP), a number of studies have been reported that organic photosensitizers, encapsulated in a rigid matrix such as PMMA, suppress vibration and rotation, resulting in the enhanced phosphorescence. [4, 5] However, few research has been conducted on the molecular rigidity for improving triplet properties in RTP and TTA-UC. In recent years, there has been an increasing interest in Donor-acceptor (D-A) based triplet sensitizers, because an orthogonal combination of donor and acceptor units may induce large charge separation, resulting in high intersystem crossing between singlet and triplet states. [6, 7] In particular, it has been reported that D-A photosensitizers can have a longer triplet lifetime than conventional heavy atom photosensitizers. [8-10] To achieve the orthogonal structure, the method of connecting the donor and the acceptor in a single bond has been mainly used. [11-13]

However, single bond that allows rotation between D-A, may shorten the triplet lifetime of photosensitizers. Therefore, restriction intramolecular rotation (RIR) between the donor and acceptor might suppress the non-radiative decay path of  $T_1 \rightarrow S_0$  and consequently enhance the triplet character such as triplet quantum yield and lifetime. Although numerous studies have been reported that RIR between D-A based on BODIPY can improve fluorescence quantum yield and fluorescence lifetime, only a few studies on the relationship between RIR and triplet characteristics have been conducted [14-17] Recently, researches on the relationship between the RIR of D-A and the triplet properties have been reported. [18, 19] Those studies were mostly focused on the limited comparisons between RIR and the singlet oxygen quantum yield (SOQY), not the triplet lifetime. Nonetheless, the RIR molecules clearly showed a 1.5- to 3.3-fold increase in triplet lifetime, compared to the rotation free molecules, this may indicate that RIR makes a significant contribution to the triplet lifetime. Recently, we have reported that the integration of a donor-acceptor with a heavy atom improves both triplet lifetime and triplet quantum yield because of the simultaneous utilization of photoinduced electron transfer (PET) and the heavy atom effect (HAE). In particular, the triplet lifetime of donor-acceptor-heavy atom (D-A-H)

photosensitizers were longer than that of D-A and pure heavy atom photosensitizers, proving that D-A-H is a tentatively promising molecular design strategy for excellent triplet sensitizers. Therefore, the RIR between D and A in D-A-H photosensitizers can be expected to further enhanced triplet lifetime. In this article, we investigated the contribution of conformational rigidity of D-A-H photosensitizers on triplet characteristics. Finally, it was confirmed that intramolecular rigidification increases the triplet lifetime and thus improves the upconversion characteristics such as upconversion emission efficiency ( $\eta_{uc}$ ) and threshold intensity ( $I_{th}$ ).

## **5.2 Experimental**

### **5.2.1 Materials**

All of the commercial reagents were purchased from Sigma-Aldrich, Alfa aesar, and Tokyo Chemical Industry (TCI) and used without further purification.

### **5.2.2 Instruments**

**Characterization**  $^1\text{H}$  NMR spectra were recorded on a Bruker Avance 500 spectrometer (National Center for Inter-University Research

Facilities at Seoul National University) at 500 MHz using chloroform-d. High resolution mass experiments were operated on an Q-TOF 5600 mass spectrometer equipped with an ESI source (National Instrumentation Center for Environmental Management).

### **UV-VIS absorption, fluorescence spectra and photoluminescence**

**lifetime** In all experiments, samples (10 $\mu$ M) were contained in a 1 x 1 cm quartz cuvette. Absorption and emission spectra were measured on by an UV-vis spectrophotometer (LAMBDA 25, Perkin Elmer Co.) and a fluorescence spectrometer (LS-55, Perkin Elmer Co.). The fluorescence lifetime was measured with a fluorophotometer (fluorolog3, HORIBA SCIENTIFIC) by irradiation of a laser ( $\lambda = 467$  nm). The triplet lifetime was recorded on the spectrofluorometer (FS5, Edinburg). Photoluminescence quantum yield of photosensitizers in toluene were estimated using an integrating sphere (QE-1100, Otsuka electronics Co.).

**Singlet oxygen quantum yield (SOQY)** SOQY of photosensitizers in toluene were carried out by using the indirect method. (standard: 2,3,7,8-tetrabromo-5,5-difluoro-10-phenyl-5H-4H,5H-dipyrrolo[1,2-c:2',1'-f] [1,3,2]diazaborinine,  $\Phi_{\Delta} = 0.49$  in toluene) [29] To determine

SOQY, a following Eqn. 5.1 was used:

$$\Phi_{\Delta,\text{sam}} = \Phi_{\Delta,\text{std}} \left( \frac{m_{\text{sam}}}{m_{\text{std}}} \right) \left( \frac{1-10^{-A_{\text{std}}}}{1-10^{-A_{\text{sam}}}} \right) \left( \frac{\eta_{\text{sam}}}{\eta_{\text{std}}} \right)^2 \quad \text{Eqn. 5.1}$$

Where  $\Phi_{\Delta,\text{sam}}$  – SOQY of the sample,  $\Phi_{\Delta,\text{std}}$  – SOQY of the standard.  $m_{\text{std}}$  and  $m_{\text{sam}}$  – absorbance of the standard and the sample at 413nm.  $A_{\text{std}}$  and  $A_{\text{sam}}$  – Absorbance of standard and sample at excitation wavelength.  $\eta_{\text{std}}$  and  $\eta_{\text{sam}}$  – the refractive index of solution in which the standard and the sample are dissolved. All samples in 3.5ml solvents contained diphenylisobenzofuran (DPBF) were irradiated with laser (505nm. 5mW  $\pm$ 3%). The concentration of DPBF was fixed to 30mM for preventing from chain reaction.

**Triplet triplet annihilation upconversion** Anti-Stokes emission was measured under 532nm laser excitation using a fuorescence spectrometer system (Model SR810 DSP Lock-in Amplifier and monochromator with a 3502 optical chopper). The signal was then detected using a photomultiplier tube (Oriel) and processed by a lock-in amplifier (SRB10 DSP, Stanford Research Systems, USA). The incident laser intensity was adjusted using a continuously variable neutral density filter and measured using a power meter (843-R, Newport Corporation, USA).

**Cyclic voltammetry** The redox potentials of the photosensitizers under a 50 mV/s scan rate were determined through cyclic voltammetry in acetonitrile containing 0.1 M Bu<sub>4</sub>NPF<sub>6</sub> as a supporting electrolyte with a potentiostat (VersaSTAT3). The samples were measured at a concentration of 0.1mM in three-electrode system with Pt working and counter electrodes, and a Ag/AgCl nonaqueous reference electrode. All potentials were referenced to the ferrocenium/ferrocene couple as an external standard.

**Theoretical Computations** Geometry optimization in the ground state ( $S_0$ ) was calculated on the basis of the B3LYP/6-31G+(d, p), while the excited singlet ( $S_1$ ) and triplet ( $T_1$ ) states were investigated by the time-dependent DFT (TD-DFT) method with the same functional and basis set of B3LYP/6-31G+ (d, p) from the optimized ground-state geometries. All the calculations were performed with Gaussian 16. The overlap integral (Sr) and natural transition orbitals (NTOs) analysis were performed using Multiwfn. [30]

## **5.2.3 Synthesis**

### **5.2.3.1 Preparation of compound 1 and 2**

In a solution of 1-pyrenecarboxaldehyde 10 mmol, 1eqn) and 2,4-

dimethylpyrrole (30mmol) in dry  $\text{CH}_2\text{Cl}_2$  (550 mL) are added a solution of trifluoroacetic acid (153  $\mu\text{L}$ , 2 mmol) in dry  $\text{CH}_2\text{Cl}_2$  (10 mL) slowly at room temperature. After 1.5 h, p-chloranil (2.22g, 9mmol) was added under ice bath cooling and stirred for 10 min. After 1h, a trimethylamine (8 mL) was added followed by  $\text{BF}_3 \cdot \text{Et}_2\text{O}$  (7 mL) the mixture was stirred for 1.5 h and then poured into water. The organic layer was extracted and dried over anhydrous  $\text{MgSO}_4$  and evaporated under reduced pressure. The crude product was purified using column chromatography using mixtures of  $\text{CH}_2\text{Cl}_2$  and hexane as eluent. **1** (540 mg, 12% yield) **2** (508 mg, 13% yield). **1** :  $^1\text{H}$  NMR (500 MHz,  $\text{CDCl}_3$ )  $\delta$  8.51-8.48 (d,  $J=8\text{Hz}$ , 1H), 8.42-8.39 (d,  $J=8\text{Hz}$ , 1H), 8.36-8.33 (d,  $J=7.5\text{Hz}$ , 1H), 8.32 (s, 2H), 8.25-8.22 (d,  $J=9\text{Hz}$ , 1H), 8.17-8.12 (t,  $J=7.5\text{Hz}$ , 1H), 8.06-8.04 (d,  $J=8\text{Hz}$ , 1H), 7.87-7.84 (d,  $J=8.5\text{Hz}$ , 1H), 6.16 (s, 2H),  $^{13}\text{C}$  NMR (500 MHz,  $\text{CDCl}_3$ )  $\delta$  155.3 142.5 140.3 131.5 131.4 130.8 130.4 129.3 128.4 127.3 126.8 126.1 125.9 125.7 123.8 123.6 123.1 121.5 HRMS-ESI (M+) Calcd for  $\text{C}_{29}\text{H}_{23}\text{BF}_2\text{N}_2$ : 448.1922 Found: 448.1923, **2** :  $^1\text{H}$  NMR (500 MHz,  $\text{CDCl}_3$ )  $\delta$  8.29-8.26 (d,  $J=8\text{Hz}$ , 1H), 8.26-8.24 (d,  $J=8\text{Hz}$ , 1H), 8.22-8.19 (d,  $J=9\text{Hz}$ , 2H), 8.16-8.14 (d,  $J=8.5\text{Hz}$ , 1H), 8.09-8.05 (d, 2H), 8.04-8.00 (m, 4H), 6.63-6.61 (d,  $J=4\text{Hz}$ , 2H), 6.47-6.45 (d,  $J=4\text{Hz}$ , 2H),  $^{13}\text{C}$  NMR (500 MHz,  $\text{CDCl}_3$ )  $\delta$  146.7 144.6 136.7 132.7 132.0 131.5

130.9 130.6 129.2 128.7 128.0 127.3 126.8 126.4 126.1 HRMS-ESI  
(M+H) Calcd for C<sub>25</sub>H<sub>16</sub>BF<sub>2</sub>N<sub>2</sub>: 393.1375 Found: 393.1369.

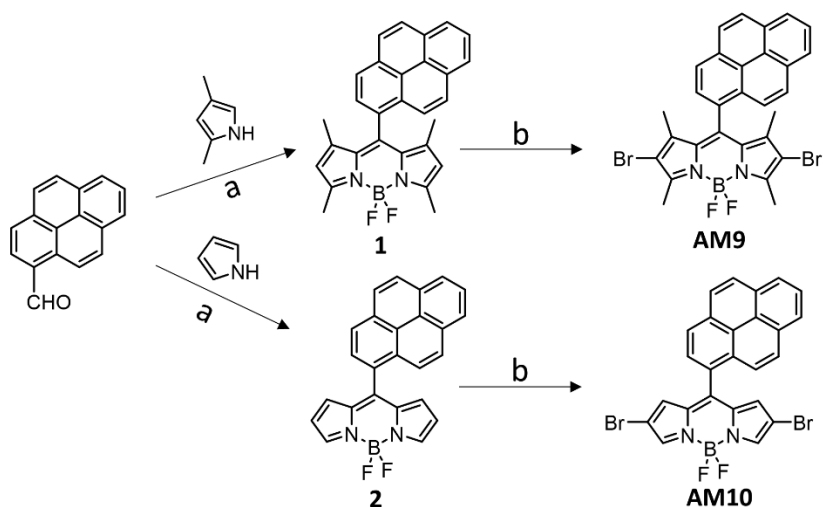
**5.2.3.2 Preparation of compound AM10 To 2** (121 mg, 0.308 mmol) in 30 mL of dry in CH<sub>2</sub>Cl<sub>2</sub> was added dropwise N-bromosuccinimide (NBS) (121mg, 0.678 mmol) in CH<sub>2</sub>Cl<sub>2</sub> (10 mL) over a period of 0.5h. The mixture was left stirring for an additional 24 h, washed with an aqueous solution of sodium chloride, and extracted by CH<sub>2</sub>Cl<sub>2</sub>. Organic layers were extracted, dried over MgSO<sub>4</sub>, and evaporated. Purification was performed by column chromatography on silica gel using hexane/CH<sub>2</sub>Cl<sub>2</sub> (1:1, v/v). **AM10** was obtained as purple solid (43mg, 25% yield) 1H NMR (500 MHz, CDCl<sub>3</sub>) δ 8.32-8.30 (d, J=8Hz, 1H), 8.29-8.23 (m, J=8Hz, 3H), 8.18-8.15 (d, J=9Hz, 1H), 8.13-8.09 (m, 2H), 8.04-8.02 (d, 9Hz, 1H), 8.01-8.00 (d, J=8Hz, 1H), 7.91 (s, 2H) 13C NMR (500 MHz, CDCl<sub>3</sub>) δ 169.8 146.6 144.7 141.0 136.4 133.2 132.0 131.5 130.8 130.5 129.7 129.3 127.9 127.3 127.0 126.8 126.5 124.8 124.7 124.3 107.7 HRMS-ESI (M+H+) Calcd for C<sub>25</sub>H<sub>14</sub>BBr<sub>2</sub>F<sub>2</sub>N<sub>2</sub>: 548.9579 Found: 548.9557

**5.2.3.2 Preparation of compound AM9 To 1** (112 mg, 0.25 mmol) in 25 mL of dry in CH<sub>2</sub>Cl<sub>2</sub> was added dropwise N-bromosuccinimide (NBS)

(101mg, 0.565 mmol) in CH<sub>2</sub>Cl<sub>2</sub> (8 mL) over a period of 0.5h. The mixture was left stirring for an additional 24 h, washed with an aqueous solution of sodium chloride, and extracted by CH<sub>2</sub>Cl<sub>2</sub>. Organic layers were extracted, dried over MgSO<sub>4</sub>, and evaporated. Purification was performed by column chromatography on silica gel using hexane/CH<sub>2</sub>Cl<sub>2</sub> (1:1, v/v). **AM9** was obtained as purple solid (70mg, 46% yield) <sup>1</sup>H NMR (500 MHz, CDCl<sub>3</sub>) δ 8.32-8.30 (d, J=8Hz, 1H), 8.30-8.28 (m, J=7.5Hz, 1H), 8.25-8.23 (d, J=7.5Hz, 1H), 8.22-8.20 (d, J=9Hz, 1H), 8.17-8.15 (d, 9Hz, 1H), 8.10-8.06 (d, J=8Hz, 2H), 7.95-7.93 (d, J=9Hz, 1H) 7.86-7.84 (d, J=7.5Hz, 1H), 2.68 (s, 6H), 0.88 (s, 6H) <sup>13</sup>C NMR (500 MHz, CDCl<sub>3</sub>) δ 154.4 141.4 140.9 132.3 131.5 131.4 131.2 129.6 129.4 128.9 128.6 127.5 126.9 126.3 126.2 125.7 124.9 124.7 123.9 112.1 HRMS-ESI (M+H<sup>+</sup>) Calcd for C<sub>29</sub>H<sub>22</sub>BBBr<sub>2</sub>F<sub>2</sub>N<sub>2</sub> 604.0127 Found: 604.0136

## 5.3 Results and discussion

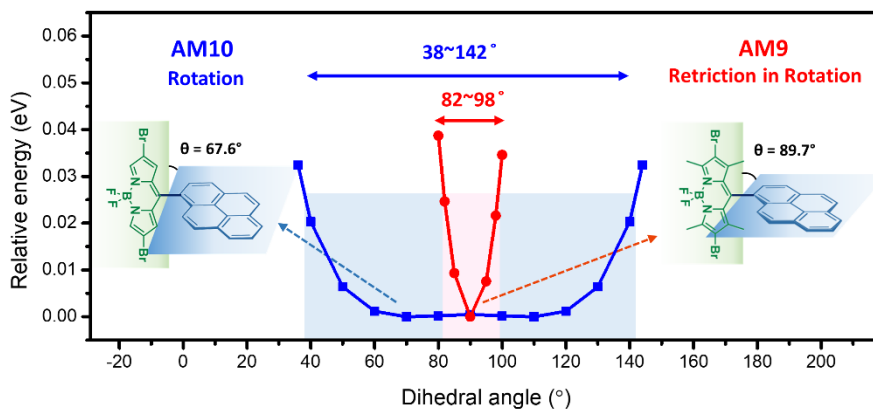
### 5.3.1 Molecular designs



Scheme 5.1 Synthesis of AM9 and AM10. Synthetic conditions : (a) trifluoroacetic acid, chloranil, trimethylamine, Boron trifluoride etherate,  $\text{CH}_2\text{Cl}_2$ , RT (b) N-bromosuccinimide,  $\text{CH}_2\text{Cl}_2$ , RT

To examine the correlation between molecular rigidity and triplet characteristics, two different D-A-H photosensitizers (AM10 and AM9) were prepared: donor, acceptor, and heavy atom of the D-A-H photosensitizers were designated as pyrene, BODIPY, and bromine, respectively (Scheme 5.1). Four-methyl groups were introduced into the BODIPY of AM9 to restrict intramolecular rotation by steric hindrance between D and A, On the other hand, D and A in AM10 can be freely

rotatable due to the absence of steric hindrance. This was confirmed by the potential energy curve along the dihedral angle ( $\theta$ ) obtained by density functional theory (DFT) as shown in Scheme 5.2.



Scheme 5.2 Optimized molecular structures and potential energy curve (PES) of AM9 and AM10 (ground state) along the dihedral angle between donor and acceptor. Optimization and single point energy were obtained by DFT/B3LYP method with 6-31G+(D, P) basis sets using the Gaussian 16 program

The minimum energy configurations of AM10 and AM9 were in the dihedral angle of 67.6 and 89.7°. The dihedral angle between D and A of AM10 were in the range of 38 - 142°, considering the thermal energy of 26meV at room temperature. On the other hands, the dihedral angle

of AM9 were in the range of 82 and 98°. These results indicate that the four-methyl groups in AM9 significantly restricted the rotation between D and A.

### 5.3.2 Photophysical properties

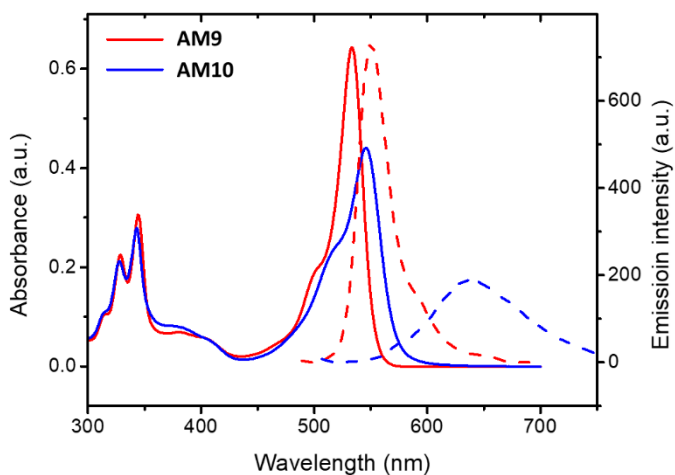


Figure 5.1 UV-VIS absorption and emission spectra of the photosensitizers in toluene. ( $10^{-5}$  M).

Table 5.1 photophysical properties of AM9 and AM10. All data was measured in toluene ( $10^{-5}$ M)

|      | $\lambda_{\text{abs,max}}^{\text{a}}$ | $\epsilon^{\text{b}}$             | $\lambda_{\text{emi,max}}^{\text{c}}$ | $\Delta f^{\text{d}}$ | $\Phi_{\text{F}}^{\text{e}}$ | $\tau_{\text{F}}^{\text{f}}$ |
|------|---------------------------------------|-----------------------------------|---------------------------------------|-----------------------|------------------------------|------------------------------|
|      | (nm)                                  | ( $\text{M}^{-1}\text{cm}^{-1}$ ) | (nm)                                  | (nm)                  |                              | (ns)                         |
| AM9  | 533                                   | 64,000                            | 550                                   | 17                    | 0.146                        | 0.9                          |
| AM10 | 546                                   | 43,000                            | 639                                   | 93                    | 0.034                        | 1.1                          |

<sup>a</sup> Absorption maximum wavelength, <sup>b</sup> Molar absorption coefficient, <sup>c</sup> emission maximum wavelength, <sup>d</sup> stokes shift, <sup>e</sup> fluorescence quantum yield, and <sup>f</sup> fluorescence lifetime

Figure. 5.1 shows the absorption and emission spectra of AM9 and AM10 in toluene ( $10^{-5}\text{M}$ ), and their photophysical properties are summarized in Table 5.1. They all show two principal absorption bands: one between 300-350nm is corresponding to local excitation (LE) of pyrene, and the other between 450-550nm is corresponding to LE of the BODIPY unit with bromine. The molar extinction coefficient at the absorption maximum of AM9 showed  $64,000\text{ M}^{-1}\text{cm}^{-1}$ , which is higher than  $43,000\text{M}^{-1}\text{cm}^{-1}$  of AM10. This absorption coefficient trend was consistent with the electronic absorption obtained by time-dependent density functional theory (TDDFT) calculation (figure 5.2). Emission maxima of AM9 and AM10 were observed at 550 nm and 639 nm, respectively. In addition, the fluorescence quantum yield of AM9 was 14.6%, which was higher than AM10 3.4%.

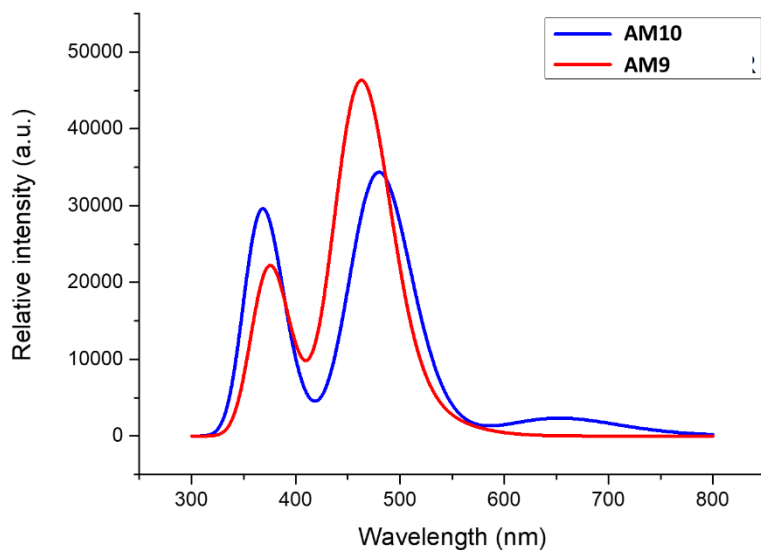


Figure 5.2 UV-VIS absorption of photosensitizers in toluene obtained by TDDFT calculation with B3LYP functional and the 6-31G+(d, p) basis set.

This indicates that nonradiative decay of AM9 from the  $S_1$  to the  $S_0$  state was prevented by RIR, as reported in several previous studies. [14-17] The absorption and emissions of AM9 and AM10 in different solvents were studied (Figure 5.3, Table 5.2). The absorption spectrum of both photosensitizers was independent on the polarity of the solvent. On the other hand, for AM10, a mirror-shaped emission band was observed in a non-polar solvent (n-hexane), corresponding to the emission generated from the locally excited state. The emission spectra

bathochromically shifted and its intensity decreased, with increasing the solvent polarity. This indicates the emission was originated from the charge transfer state generated by PET. For AM9, the mirror-shaped LE emission was observed in all solvents, and independent on the solvent polarity. Oppositely, the fluorescence intensity and quantum yield of them decreased with increasing solvent polarity, that may indicate that  $S_1$  state decayed nonradiatively by PET in a high polar solvent. [3, 19, 20]

Table 5.2 Absorption and emission maximum wavelength, photophysical properties of photosensitizers in different solvents

| Solvents |      | $\lambda_{\text{abs}}$<br>[nm] | $\epsilon$<br>[ $M^{-1} \text{ cm}^{-1}$ ] | $\lambda_{\text{emi}}$<br>[nm] | $\Delta f$<br>[nm] | $\Phi_F$ |
|----------|------|--------------------------------|--|--------------------------------|--------------------|----------|
|          | HX   | 531                            | 68,000                                     | 546                            | 15                 | 0.220    |
|          | TOL  | 533                            | 64,000                                     | 550                            | 17                 | 0.146    |
| AM9      | CF   | 533                            | 68,000                                     | 549                            | 16                 | 0.145    |
|          | MC   | 531                            | 62,000                                     | 548                            | 17                 | 0.092    |
|          | ETOH | 528                            | 57,000                                     | 547                            | 19                 | 0.021    |
| AM10     | HX   | 543                            | 37,000                                     | 565                            | 22                 | 0.038    |
|          | TOL  | 546                            | 43,000                                     | 639                            | 93                 | 0.034    |

|      |     |        |   |   |       |
|------|-----|--------|---|---|-------|
| CF   | 545 | 40,000 | - | - | 0.000 |
| MC   | 543 | 41,000 | - | - | 0.000 |
| ETOH | 540 | 34,000 | - | - | 0.000 |

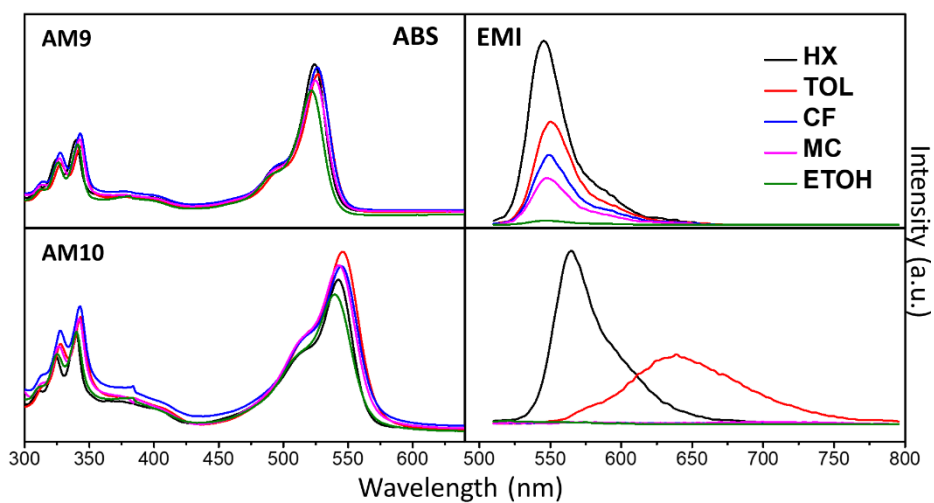


Figure 5.3 UV-VIS absorption and emission spectra of photosensitizers in hexane (HX), toluene (TOL), chloroform (CF), dichloromethane (MC), and ethanol (ETOH) solutions.

### 5.3.3 Singlet oxygen quantum yield (SOQY)

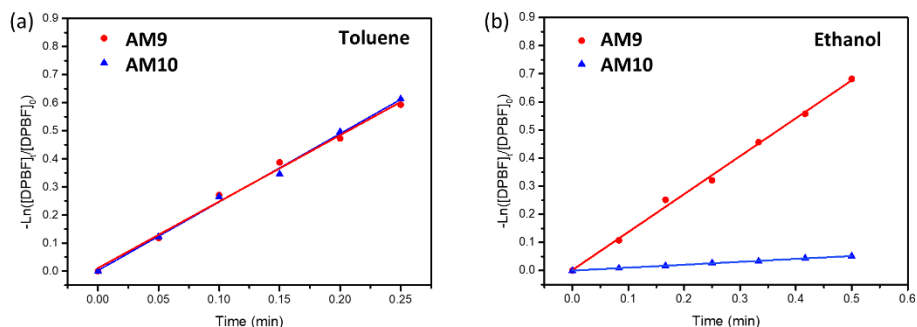


Figure 5.4 Time dependence of  $\ln([DPBF]_t/[DPBF]_0)$  of mixtures with photosensitizers and DPBF in toluene (a) and ethanol (b) under irradiation (505nm green laser).

The SOQY of photosensitizers were measured for quantitative evaluation of population in triplet excited state. (Figure 5.4) In toluene, no significant differences were found in SOQY between AM9 (0.60) and AM10 (0.61), despite their structural differences. Considering that the photosensitizer introduced by a benzene instead of a pyrene in AM9 showed 0.29 of SOQY in toluene, the high SOQY of AM9 may be due to the simultaneous use of HAE and PET (Figure 5.5). AM9 showed high SOQY (0.83) in ethanol as compared with that in toluene, which may indicate that the increased PET in high polar medium enhanced the SOQY (Figure 5.6). In contrast, the SOQY of AM10 dropped from 0.61

in toluene to the 0.05 in ethanol. This lowered SOQY in ethanol is not the general behavior of PET photosensitizers, and this probably means that there is an additional nonradiative decay channel in the triplet state or singlet charge transfer state.

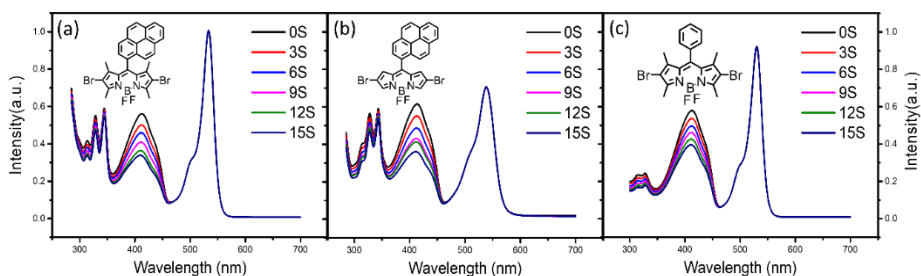


Figure 5.5 Determination of singlet oxygen quantum yield of AM9 (a), AM10 (b), BEN-MBD-BR (c) photosensitizers in toluene (absorbance at 505nm = 0.3).

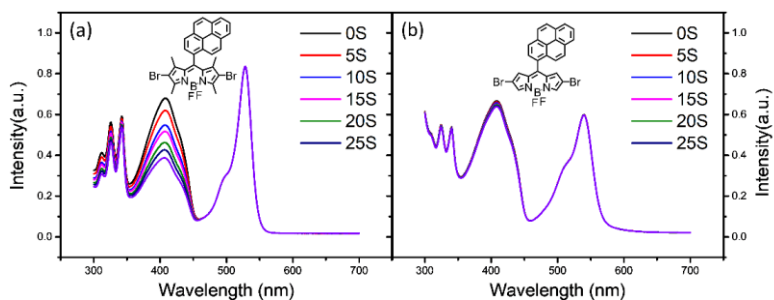


Figure 5.6 Determination of singlet oxygen quantum yield of AM9 (a), AM10 (b) photosensitizers in ethanol.

### 5.3.4 Triplet lifetime analysis

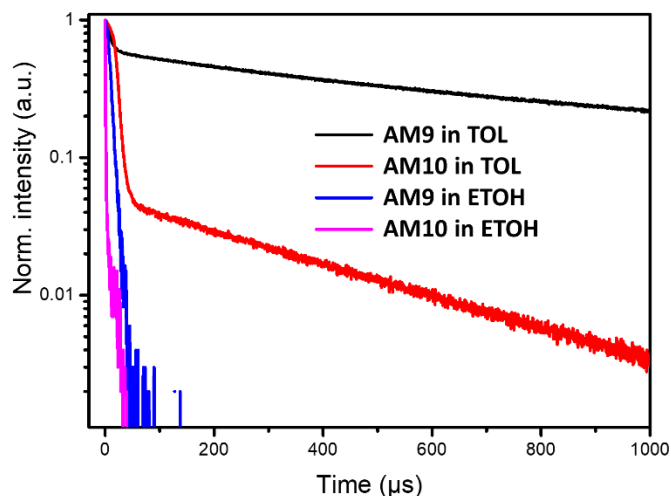


Figure 5.7 Time resolved photoluminescence (TRPL) decay curves of AM9 and AM10 in toluene and ethanol ( $10^{-5}\text{M}$ )

Figure 5.7 shows the triplet lifetime of photosensitizers in toluene and ethanol. In toluene, AM10 showed a relatively short lifetime of  $352\mu\text{s}$ , while AM9 showed an ultra-long lifetime of  $1,503\mu\text{s}$ . To the best of our knowledge, this is the longest lifetime among the previously reported BODIPY based triplet sensitizers, and it is also considerably high compared to the common triplet photosensitizers. [8, 21, 22] This clearly indicates that the RIR between D-A significantly affects the increase in triplet lifetime. The triplet lifetime measured in ethanol also showed the similar trend as that in toluene. AM9 showed approximately 8 times

higher triplet lifetime of 8.5 $\mu$ s compared to 0.9 $\mu$ s of AM10. Considering that the triplet lifetime of sensitizer should be at least 1 $\mu$ s to generate singlet oxygen, the exceptionally low SOQY of AM10 in ethanol might be due to its short lifetime. [23] That is, the electrons at the triplet states might decay to the  $S_0$  state rapidly before interacting with oxygen, resulting in low SOQY, even though the ISC from  $S_1$  to  $T_n$  states may be large enough by large PET properties. Meanwhile, the SOQY of both photosensitizers in ethanol showed a significantly smaller value compared to those in toluene. This may be due to the lowered energy gap between  $T_1$  and  $S_0$  states in ethanol, or an increase in the magnitude of the LE characteristics. This will be further discussed in the quantum chemical calculation section.

### **5.3.5 Electrochemical properties**

The redox properties of photosensitizers in acetonitrile were measured through cyclic voltammetry (Figure 5.8). And additional BODIPY moieties including MBD-BR and BD-BR were prepared for examining the PET kinetics. AM9 showed the oxidation potential ( $E_{OX}$ ) of 1.30V and reduction potential ( $E_{RED}$ ) of -0.69V, which are almost identical to  $E_{OX}$  of pyrene (1.29V) and  $E_{RED}$  of MBD-BR (-0.65V).

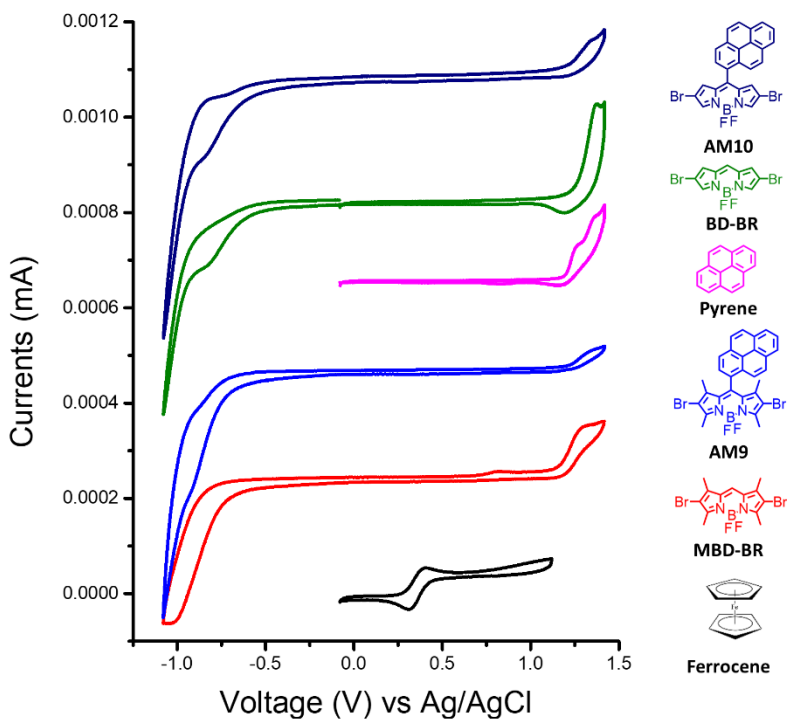


Figure 5.8 Cyclic voltammogram of Photosensitizers measured in acetonitrile. (All voltammograms were shifted based on the oxidation potential of the ferrocenium / ferrocene couple. ( $\text{Fc}^+/\text{Fc} = 0.38\text{V}$ ).

AM10 also showed the  $E_{\text{OX}}$  of 1.29V and  $E_{\text{RED}}$  of -0.57V, which are roughly equal to  $E_{\text{OX}}$  of pyrene (1.29V) and  $E_{\text{RED}}$  of BD-BR (-0.55V). These results may show that pyrene unit of AM9 and AM10 acts as an electron donor and BODIPY units act as electron acceptors in PET process. For a quantitative evaluation of energy transfer between donor

and acceptor, Gibbs free energy changes of charge separation ( $\Delta G_{CS}$ ) was explored. The  $\Delta G_{CS}$  was calculated by the Rehm–Weller equation (eqn. 5.2), as follows,

$$\Delta G_{CS} = e[E_{OX} - E_{RED}] - E_{00} + \Delta G_S \quad \text{eqn. 5.2}$$

$$\Delta G_S = -\frac{e^2}{4\pi\epsilon_S\epsilon_0 R_{CC}} - \frac{e^2}{8\pi\epsilon_0} \left( \frac{1}{R_D} + \frac{1}{R_A} \right) \left( \frac{1}{\epsilon_{REF}} - \frac{1}{\epsilon_S} \right) \quad \text{eqn. 5.3}$$

where  $e$  is the elementary charge,  $E_{OX}$  is the one-electron oxidation potential of the electron donor (pyrene),  $E_{RED}$  is the one-electron reduction potential of the electron acceptor (BODIPY),  $E_{00}$  is the energy level approximated with normalized UV–vis absorption spectra and fluorescence emission spectra.  $\Delta G_S$  is the Coulomb interaction energy associated with the radical ion pair, which is defined by eqn.5.3.  $\epsilon_{ref}$  is a dielectric constant of acetonitrile used in cyclic voltammetry experiment ( $\epsilon_{ref, acetonitrile} = 37.5$ ).  $\epsilon_S$  is a dielectric constant of the solvent of interest ( $\epsilon_S, toluene = 2.4$ ,  $\epsilon_S, ethanol = 25.4$ ),  $\epsilon_0$  is the vacuum permittivity.  $R_{CC}$  is center-to-center separation distance between the electron donor and the electron acceptor.  $R_D$  and  $R_A$  are radius of electron donor and acceptor unit, obtained from DFT optimization.  $R_{cc}$  of AM9 and AM10 were 5.75 and 5.82Å respectively. The redox potential and charge

separation gibbs free energy changes of photosensitizers were shown in table 5.3.

Table 5.3 Redox potentials and charge separation gibbs free energy of AM9 and AM10

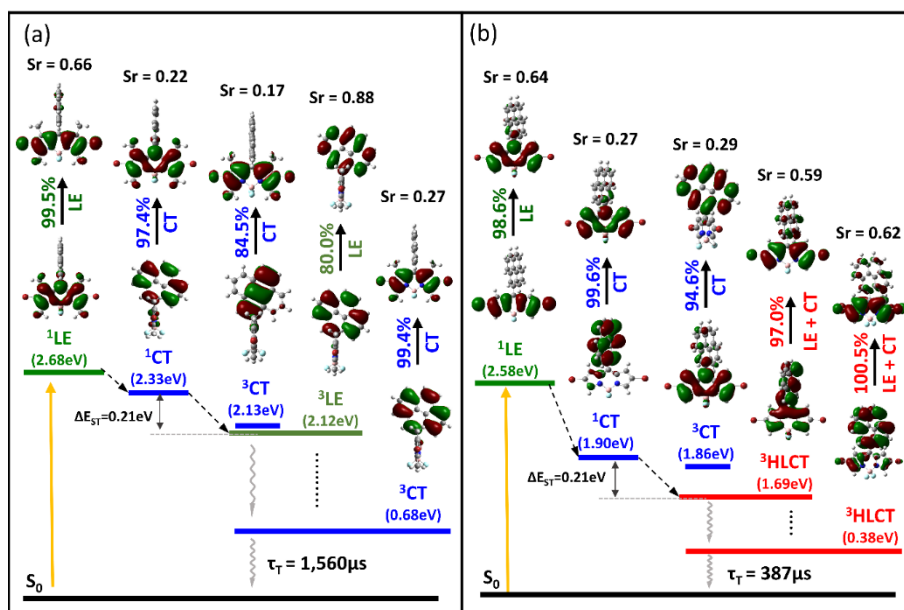
|      | $E_{00}$<br>(eV) <sup>a</sup> | $E_{OX}$<br>(V) <sup>b</sup> | $E_{RED}$<br>(V) <sup>b</sup> | $\Delta G_{CS}$<br>(eV) <sup>c</sup> | $\Delta G_{CS}$<br>(eV) <sup>d</sup> |
|------|-------------------------------|------------------------------|-------------------------------|--------------------------------------|--------------------------------------|
| AM9  | 2.30                          | 1.30                         | -0.69                         | -0.06                                | -0.38                                |
| AM10 | 2.24                          | 1.29                         | -0.57                         | -0.05                                | -0.43                                |

<sup>a</sup> The first singlet excited energy level obtained by absorption and emission spectrum. <sup>b</sup> Cyclic voltammetry of photosensitizers ( $10^{-4}M$ ) were measured in acetonitrile containing a 0.10 M Bu<sub>4</sub>NPF<sub>6</sub> supporting electrolyte; the working electrode and counter electrode are a Pt electrode; Ag/AgCl couple as the reference electrode. The oxidation and reduction potential were determined with onset in spectrum, because the irreversible redox spectra were observed. <sup>c</sup> in toluene, <sup>d</sup> in ethanol.

Given that the value of  $-\Delta G_{CS}$  was almost similar for of AM9 (0.06) and AM10 (0.05), PET for both photosensitizers may have occurred with same degree. And this would have contributed to both photosensitizers having almost the same SOQY value. In ethanol, AM10 showed slightly larger  $-\Delta G_{CS}$  values compared to AM9. However, the trend of SOQY was contrary to this result, which was due to the shortened triplet lifetime

of AM10 as have noted previously. In addition, the  $-\Delta G_{CS}$  for both photosensitizers was higher in ethanol than that in toluene, suggesting that the PET occurs predominantly in a high polar environment. And this may have contributed to the increase in SOQY of AM9 in ethanol as compared to that in toluene.

### 5.3.6 Quantum chemical calculation

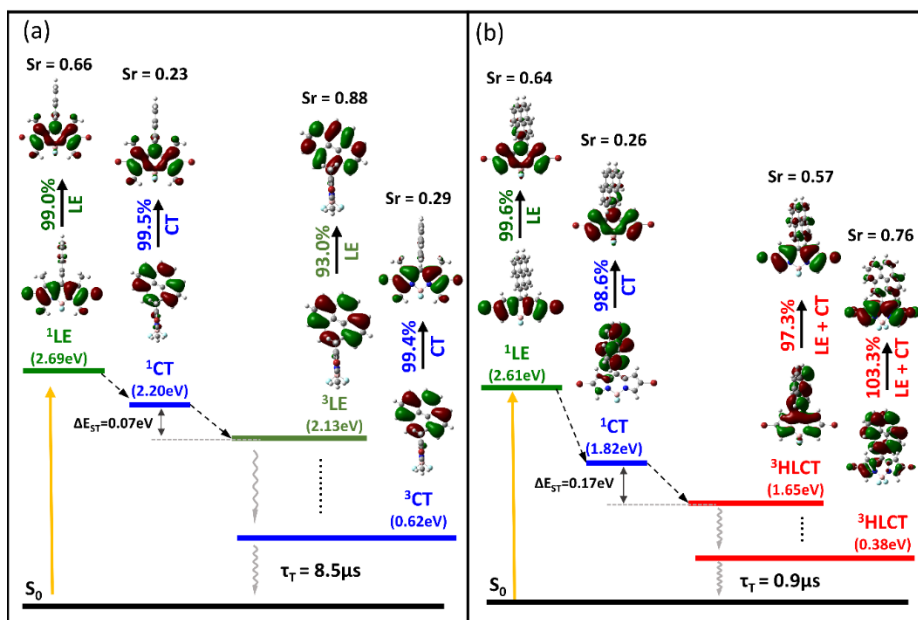


Scheme 5.3 Energy level diagram and photophysical process of (a) AM9 and (b) AM10 in toluene. Energy levels of the excited states are obtained with the vertical TD-DFT calculation. The  $Sr$  is the overlap integral between HONTO and LUNTO at the specified state.

To examine the photophysical kinetics of photosensitizers, the excited state energy level and corresponding natural transition orbital (NTO) were obtained with the aid of TDDFT calculation. (Scheme 5.3) In  $S_2$  state, both highest occupied natural transition orbital (HONTO) and lowest unoccupied natural transition orbital (LUNTO) of AM9 and AM10 are localized to the BODIPY, and thus the  $S_2$  state can be assigned to singlet local excited ( $^1LE$ ) state. In  $S_1$  state, HONTO and LUNTO of both photosensitizers were distributed to the pyrene and the BODIPY respectively. This indicates that the  $S_1$  state is corresponding to the singlet charge transfer excited ( $^1CT$ ) state, and this supports that the PET occurs in the photosensitizers. For quantitative evaluation of the transition characteristics, the overlap integral ( $S_r$ ) between HONTO and LUNTO was calculated using multiwfn software. The  $S_r$  at the  $S_2$  state was 0.66, which is relatively high compared to 0.22 at the  $S_1$  state, this supports that the  $S_2$  and  $S_1$  states shows the local excited (LE) and charge transfer (CT) characteristics respectively. The ISC pathway between singlet and triplet excited states are determined by the arrangement of those excited states: Electrons in the  $^1CT$  state will move predominantly to a triplet excited state having similar energy level to the  $^1CT$  state. For AM9, the triplet charge transfer ( $^3CT$ ) state was located

just below the  $^1\text{CT}$  state. Since both states show CT characteristics, hyperfine coupling induced intersystemcrossing (HFC-ISC) is effective for the transition from the  $^1\text{CT}$  to the  $^3\text{CT}$  states. However, since it is required of extremely small  $\Delta E_{\text{ST}}$  ( $20\mu\text{eV}$ ) values for HFC-ISC to occur, the contribution of the HFC-ISC in total ISC might not be significant. The triplet state located secondly closest to the  $^1\text{CT}$  state showed the LE character, which is corresponding to the triplet local excited ( $^3\text{LE}$ ) state. The transition between these two states is valid by the mechanism of spin-orbit charge transfer induced ISC (SOCT-ISC), would mainly contribute the total ISC. For AM10, the HFC-ISC from the  $^1\text{CT}$  to  $^3\text{CT}$  state may be inefficient like AM9. The transition character of the second-closest triplet state showed that HONTO is distributed over the whole molecule, and the LUNTO is mainly concentrated on the BODIPY moiety. This means that this triplet state corresponds to the hybridized local and charge transfer (HLCT) excited state. Therefore, the CT portion in the NTO will participate in the HFC-ISC, and the LE portion will participate in the SOCT-ISC. One of the important parameters determining the magnitude of the ISC is the energy gap between singlet and triplet excited states ( $\Delta E_{\text{ST}}$ ). For AM9 and AM10, the  $\Delta E_{\text{ST}}$  between the singlet and triplet excited states associated with the SOCT-ISC were the same

as 0.21 eV. This result may explain the similar value of the SOQY for AM9 and AM10 in toluene. Additionally, we further investigated the characteristics of the  $T_1$  state, since the triplet lifetime is mainly determined by the decay from  $T_1$  to  $S_0$  state, and thus the transition characteristics of the  $T_1$  state may provide the key information of the decay profile. The  $T_1$  state of AM9 clearly showed the charge transfer characteristics: the HONTO and the LUNTO were localized to Pyrene and BODIPY moieties, respectively, and the  $S_r$  was low value of 0.27. The  $T_1$  state of AM10 showed HLCT characteristics: most HONTO was mainly distributed in Pyrene, and some HONTO was also located in BODIPY. In contrast, LUNTO was mainly localized in BODIPY, and a small amount of LUNTO was also localized in Pyrene. Furthermore, the overlap between HONTO and LUNTO was a significantly large ( $S_r = 0.66$ ), which could mean that LE occurs more predominantly than CT. Recently, Zhao et al and Barbon et al. reported that the lowest triplet excited state with charge triplet character will lead to a long triplet lifetime, because the charge recombination from the  $^3CT$  state to the  $S_0$  state is electron spin forbidden. [24, 25]



Scheme 5.4 Energy level diagram and photophysical process of (a) AM9 and (b) AM10 in ethanol. Energy levels of the excited states are obtained with the TD-DFT calculation. The Sr is the overlap integral between HONTO and LUNTO at the specified state.

Therefore, the considerably large triplet lifetime of AM9 may be because the  $T_1$  state mainly has charge transfer character, and the short triplet lifetime of AM10 was due to the dominant LE characteristics of  $T_1$  state. The calculated excited state energy level and NTO in ethanol were similar to those in toluene. (Scheme 5.4). In particular, the Sr at  $T_1$  state

was 0.29 for AM9 and 0.76 for AM10, which was larger than those of toluene. This result means that the LE properties at  $T_1$  state became large in ethanol, which may have played a vital role in bringing about the shortened triplet lifetime.

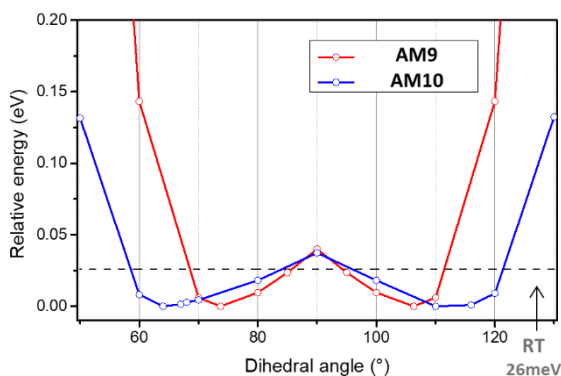


Figure 5.9 Potential energy curve at  $T_1$  state of AM9 and AM10. (The relative  $T_1$  state energy was determined based on the  $S_0$  energy level. The thermal energy line is drawn at 26meV over the lowest  $T_1$  energy with gray dashed line.)

To investigate the rotational variation of  $T_1$  state, potential energy curve of  $T_1$  state was obtained as a function of the dihedral angle between D and A (Figure 5.9). The  $T_1$  state of AM9 and AM10 showed the lowest energy level at the dihedral angle 74 and 64 degrees, respectively. Considering the thermal energy at room temperature, AM9 shows the relatively large range between 59-86 degrees, whereas AM9 shows the

small range between 69-84 degrees. As mentioned in the introduction section, the nonradiative decay from  $T_1$  to  $S_0$  state may be determined by the magnitude of vibration and rotation, and thus nonradiative decay may be fast in AM10. In addition, the energy gap ( $\Delta E_{T_1-S_0}$ ) between  $T_1$  and  $S_0$  state of AM10 was 0.38 eV, which was smaller than that of AM9 (0.68 eV). This small  $\Delta E_{T_1-S_0}$  of AM10 certainly caused the large vibrational overlap of the two involved states according to the energy gap law, and consequently increase in the nonradiative decay rate of  $T_1$  state. [26]

### 5.3.7 Triplet-triplet annihilation upconversion

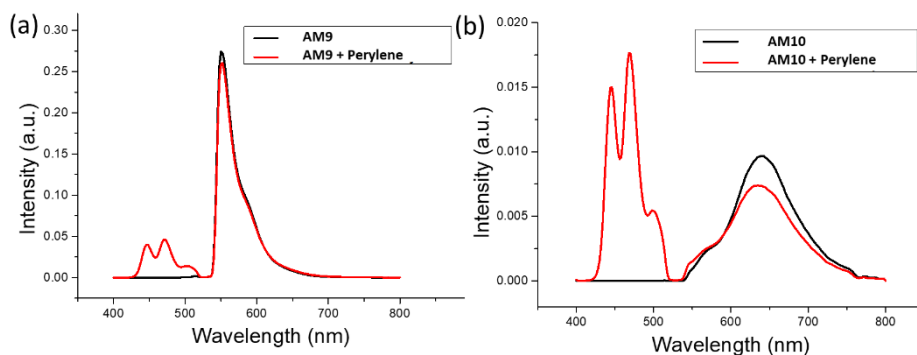


Figure 5.10 Upconversion emission spectra with and without perylene (8 μM) of (a) AM9 (10 μM) (b) AM9

The Triplet-triplet annihilation (TTA) upconversion properties of AM9 and

AM10 in deaerated toluene were investigated using commercial 532nm green diode laser. AM9 and AM10 were used as a triplet donor, and perylene was used as an annihilator. Only prompt emission of AM9 and AM10 were observed in the solution containing only triplet photosensitizers without perylene (Figure 5.10). On the other hand, in the solution containing both perylene and triplet photosensitizer, a clear additional emission spectrum band was observed in the range of 400-500 nm, which is consistent with the intrinsic emission spectrum of perylene. Therefore, this result means that upconverted emission occurred by TTA for both triplet photosensitizers. AM9 showed about two times higher of the upconverted emission intensity compared to AM10, which can be clearly confirmed in the cuvette photographs (Figure 5.11a, b). Even in the absence of a 530nm short pass filter, blue light was observed in AM9, but AM10 only appeared a red light corresponding to prompt emission. As the 530nm short pass filter was applied, the strong blue emission of AM9 was more clearly observed.

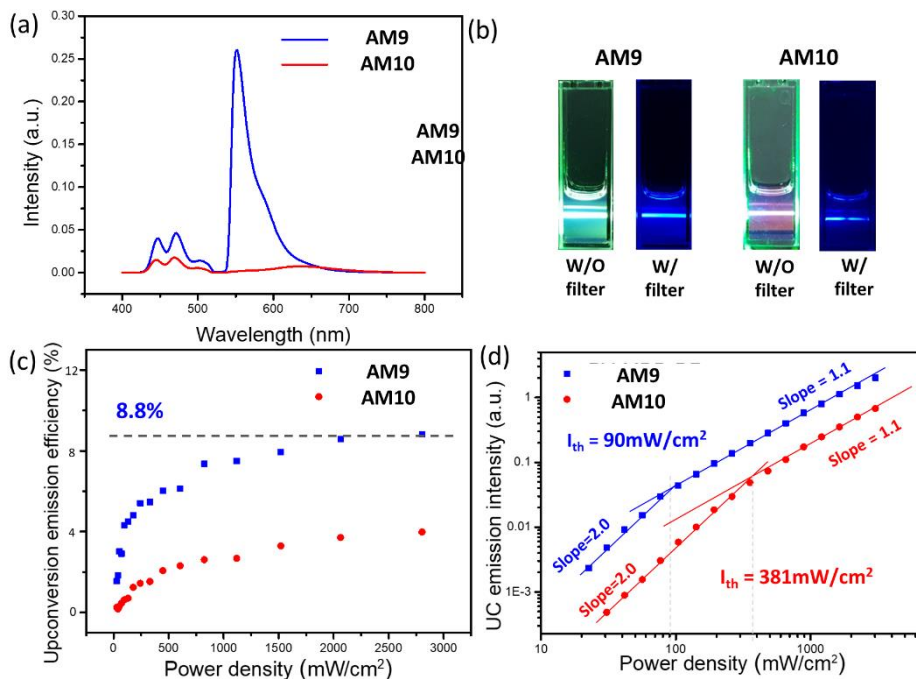


Figure 5.11 (a) TTA-UC photoluminescence spectra of AM9 and AM10 as triplet photosensitizers ( $10\mu\text{M}$ ) and perylene as triplet annihilator ( $8\mu\text{M}$ ) using  $532\text{nm}$  green laser (b) photograph of TTA-UC emission including triplet photosensitizers without (left) and with (right)  $530\text{nm}$  short pass filter. (c) upconversion emission efficiencies and (d) upconversion intensity (log scale) as a function of incident laser power density ( $\text{mW}/\text{cm}^2$ ).

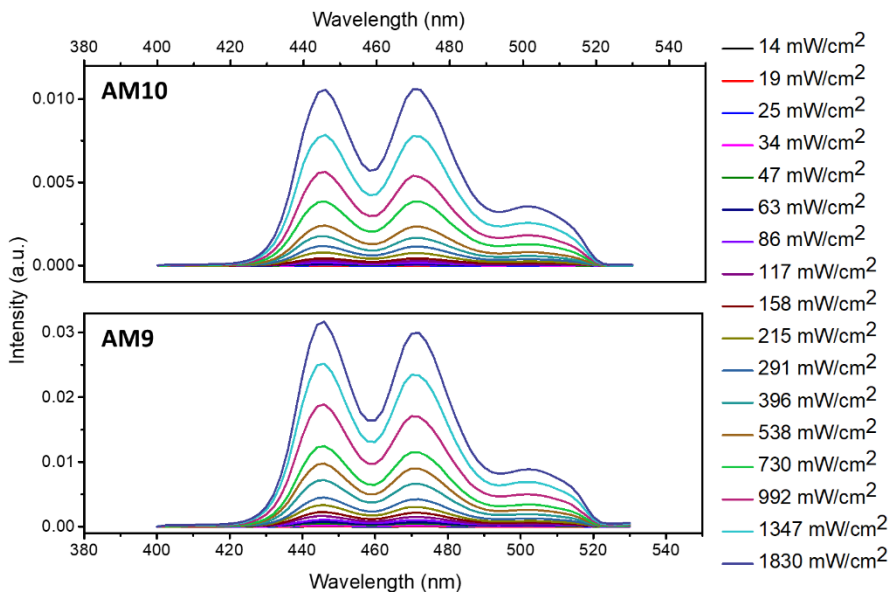


Figure 5.12 Photoluminescence spectra of AM9 and AM10 with different incident laser power density

To further characterize the TTA-UC characteristics, the upconversion intensity and the upconversion emission efficiency were measured as a function of incident laser power density (Figures 5.11c, d and 5.12). And the upconversion emission efficiency was determined through the following equation.

$$\eta_{UC,sam} = 2\Phi_{std} \left( \frac{I_{sam}}{I_{std}} \right) \left( \frac{1-10^{-A_{std}}}{1-10^{-A_{sam}}} \right) \left( \frac{n_{sam}}{n_{std}} \right)^2 \quad \text{eqn. 5.4}$$

Where  $\eta$ ,  $I$ ,  $A$  and  $n$  are upconversion emission efficiency, integrated upconverted emission intensities, absorbance of triplet photosensitizers

at 532nm and solvent refractive index. The subscript of std and sam indicate standard and sample, respectively. Diiodo-bodipy was used as the standard in toluene ( $\Phi_{\text{std}}=4.38\%$ ). [27] The UC intensity and emission efficiency of both photosensitizers increased, with increasing the laser power. At low excitation power, UC intensity of both photosensitizers was quadratic dependent on the excitation power, which adjusted to the linear dependence with increasing the excitation power. The  $\eta_{\text{UC}}$  of AM9 was 8.80%, which is higher than 3.98% of AM10 at the excitation power of  $2.8\text{W}/\text{cm}^2$ , and even slightly higher than the 8.75% of Diiodo-bodipy measured in the identical experimental setup. (Table 5.4) It is notable that the  $\eta_{\text{UC}}$  of AM9 and AM10 differed, considering that the SOQY of both photosensitizers were almost same in toluene.

Table 5.4 Upconversion emission efficiency ( $\eta_{\text{UC}}$ ) and upconversion capability ( $\phi_{\text{UC}}$ ), and threshold intensity ( $I_{\text{th}}$ ) for AM9 and AM10 in toluene

|      | $\eta_{\text{UC}}$<br>(%) | $\phi_{\text{UC}}$ | $I_{\text{th}}$ ( $\text{mW}/\text{cm}^2$ ) |
|------|---------------------------|--------------------|---|
| AM10 | 4.0                       | 86,000             | 381   |
| AM9  | 8.8                       | 283,000            | 90  |

This may be that AM9, which exhibited a high triplet lifetime, had a

higher probability of interacting with the annihilator before triplet energy loss, due to the slow nonradiative decay. In contrast, the triplet energy of the AM10 decayed more dominantly than AM9, and thus the amount of triplet energy transferred to the annihilator may be small. According to the theory that  $\eta_{UC}$  is proportional to  $\Phi_{TTET}$ , the relatively small  $\Phi_{TTET}$  of AM10 probably played a key role in bringing about the  $\eta_{UC}$  smaller. In addition, we obtained the upconversion capability ( $\varphi_{UC}$ ) through the equation of  $\varphi_{UC} = \epsilon \times \eta_{UC}$ . UC capability is a more suitable parameter to evaluate the actual performance of TTA-UC than the  $\eta_{UC}$  because the molar absorption coefficient ( $\epsilon$ ) of the sensitizer is reflected. [28] Since AM9 had a higher  $\epsilon$  and  $\eta_{UC}$  than AM10, the  $\varphi_{UC}$  of AM9 was approximately three times larger than that of AM10. This indicates that the introduction of RIR to D-A-H photosensitizers increases considerably to TTA-UC properties. The threshold intensity ( $I_{th}$ ) means the lowest light power density that the TTA process dominantly occurs, has been obtained from the graph of the UC emission intensity versus excitation power. It was determined by the intersection of the extrapolated slopes between the quadratic and linear range of the graph (Figure 5.11d). The small  $I_{th}$  value means that TTA-UC can occur even at a low excitation power density, thus UC system with the smaller  $I_{th}$

indicates that the system shows the more efficient TTA-UC. The  $I_{th}$  of AM9 and AM10 were 90 and 381mW/cm<sup>2</sup>, respectively. Since  $I_{th}$  is inversely proportional to the  $\Phi_{TTET}$ , the long triplet lifetime of AM9 may have contributed to the small  $I_{th}$ .

## 5.4 Conclusions

In conclusions, this study investigated whether the restriction intramolecular rotation (RIR) of the triplet sensitizer increases the triplet lifetime for improving the characteristics of TTA-UC based on the donor-acceptor-heavy atom structure. To prove this, AM9 with RIR and AM10 with free rotation were prepared. The SOQY of AM9 and AM10 in toluene showed almost the same value, which may be because both photosensitizer showed the similar value of charge separation driving force. AM9 appeared ultra-long triplet lifetime of 1,503 $\mu$ s in toluene as compared to the AM10. This may be because the large  $\Delta E_{T_1-S_0}$  and the RIR of AM9 suppressed vibrational overlap between  $T_1$  and  $S_0$  states, preventing nonradiative decay from  $T_1$  to  $S_0$  states. In addition, the  $T_1$  state of AM9 appeared a charge transfer characteristic, so that the nonradiative decay was further suppressed, resulting in an ultralong

triplet lifetime. Therefore, this ultralong triplet lifetime increased the  $\Phi_{\text{TET}}$  between the triplet sensitizer and the annihilator in TTA-UC system, which in turn improved both the TTA-UC emission efficiency and the threshold intensity ( $I_{\text{th}}$ ).

## 5.5 References

- [1] Dance ZEX, Mickley SM, Wilson TM, Ricks AB, Scott AM, Ratner MA, et al. Intersystem Crossing Mediated by Photoinduced Intramolecular Charge Transfer: Julolidine–Anthracene Molecules with Perpendicular  $\pi$  Systems. *The Journal of Physical Chemistry A*. 2008;112(18):4194-201.
- [2] Filatov MA, Karuthedath S, Polestshuk PM, Savoie H, Flanagan KJ, Sy C, et al. Generation of Triplet Excited States via Photoinduced Electron Transfer in meso-anthra-BODIPY: Fluorogenic Response toward Singlet Oxygen in Solution and in Vitro. *Journal of the American Chemical Society*. 2017;139(18):6282-5.
- [3] Wang Z, Zhao J. Bodipy–Anthracene Dyads as Triplet Photosensitizers: Effect of Chromophore Orientation on Triplet-State Formation Efficiency and Application in Triplet–Triplet Annihilation

Upconversion. *Organic Letters*. 2017;19(17):4492-5.

[4] Kenry, Chen C, Liu B. Enhancing the performance of pure organic room-temperature phosphorescent luminophores. *Nature Communications*. 2019;10(1):2111.

[5] Ma X, Wang J, Tian H. Assembling-Induced Emission: An Efficient Approach for Amorphous Metal-Free Organic Emitting Materials with Room-Temperature Phosphorescence. *Accounts of Chemical Research*. 2019;52(3):738-48.

[6] Chen X-K, Kim D, Brédas J-L. Thermally Activated Delayed Fluorescence (TADF) Path toward Efficient Electroluminescence in Purely Organic Materials: Molecular Level Insight. *Accounts of Chemical Research*. 2018;51(9):2215-24.

[7] Gibbons DJ, Farawar A, Mazzella P, Leroy-Lhez S, Williams RM. Making triplets from photo-generated charges: observations, mechanisms and theory. *Photochemical & Photobiological Sciences*. 2020;19(2):136-58.

[8] Hou Y, Liu Q, Zhao J. An exceptionally long-lived triplet state of red light-absorbing compact phenothiazine-styrylBodipy electron donor/acceptor dyads: a better alternative to the heavy atom-effect? *Chemical Communications*. 2020;56(11):1721-4.

- [9] Wu W, Cui X, Zhao J. Hetero Bodipy-dimers as heavy atom-free triplet photosensitizers showing a long-lived triplet excited state for triplet–triplet annihilation upconversion. *Chemical Communications*. 2013;49(79):9009-11.
- [10] Dong Y, Dick B, Zhao J. Twisted Bodipy Derivative as a Heavy-Atom-Free Triplet Photosensitizer Showing Strong Absorption of Yellow Light, Intersystem Crossing, and a High-Energy Long-Lived Triplet State. *Organic Letters*. 2020;22(14):5535-9.
- [11] Filatov MA. Heavy-atom-free BODIPY photosensitizers with intersystem crossing mediated by intramolecular photoinduced electron transfer. *Organic & Biomolecular Chemistry*. 2020;18(1):10-27.
- [12] Tao Y, Yuan K, Chen T, Xu P, Li H, Chen R, et al. Thermally Activated Delayed Fluorescence Materials Towards the Breakthrough of Organoelectronics. *Advanced Materials*. 2014;26(47):7931-58.
- [13] Zhang X-F, Zhang Y, Xu B. Enhance the fluorescence and singlet oxygen generation ability of BODIPY: Modification on the meso-phenyl unit with electron withdrawing groups. *Journal of Photochemistry and Photobiology A: Chemistry*. 2017;349:197-206.
- [14] Dong Y, Elmali A, Zhao J, Dick B, Karatay A. Long-Lived Triplet Excited State Accessed with Spin-Orbit Charge Transfer Intersystem

Crossing in Red Light-Absorbing Phenoxazine-Styryl BODIPY Electron Donor/Acceptor Dyads. *Chemphyschem*. 2020;21(13):1388-401.

[15] Gupta N, Reja SI, Bhalla V, Gupta M, Kaur G, Kumar M. A bodipy based fluorescent probe for evaluating and identifying cancer, normal and apoptotic C6 cells on the basis of changes in intracellular viscosity. *Journal of Materials Chemistry B*. 2016;4(11):1968-77.

[16] Lee Jm, Yuk Sb, Namgoong Jw, Kim Jp. Mechanofluorochromism of Triphenylamine-BODIPY: Effect of twisted intramolecular charge transfer and restriction in rotation on fluorescence. *Dyes and Pigments*. 2021;185:108864.

[17] Lou Z, Hou Y, Chen K, Zhao J, Ji S, Zhong F, et al. Different Quenching Effect of Intramolecular Rotation on the Singlet and Triplet Excited States of Bodipy. *The Journal of Physical Chemistry C*. 2018;122(1):185-93.

[18] Dong Y, Sukhanov AA, Zhao J, Elmali A, Li X, Dick B, et al. Spin–Orbit Charge-Transfer Intersystem Crossing (SOCT-ISC) in Bodipy-Phenoxazine Dyads: Effect of Chromophore Orientation and Conformation Restriction on the Photophysical Properties. *The Journal of Physical Chemistry C*. 2019;123(37):22793-811.

[19] Hou Y, Liu J, Zhang N, Zhao J. Long-Lived Local Triplet Excited

State and Charge Transfer State of 4,4'-Dimethoxy Triphenylamine-BODIPY Compact Electron Donor/Acceptor Dyads. *The Journal of Physical Chemistry A*. 2020;124(45):9360-74.

[20] Lei Y, Chen K, Tang G, Zhao J, Gurzadyan GG. Bodipy-Phenylethynyl Anthracene Dyad: Spin-Orbit Charge Transfer Intersystem Crossing and Triplet Excited-State Equilibrium. *Journal of Photochemistry and Photobiology A: Chemistry*. 2020;398:112573.

[21] Zhao J, Xu K, Yang W, Wang Z, Zhong F. The triplet excited state of Bodipy: formation, modulation and application. *Chemical Society Reviews*. 2015;44(24):8904-39.

[22] Yang Z-S, Ning Y, Yin H-Y, Zhang J-L. Lutetium(iii) porphyrinoids as effective triplet photosensitizers for photon upconversion based on triplet-triplet annihilation (TTA). *Inorganic Chemistry Frontiers*. 2018;5(9):2291-9.

[23] Monro S, Colón KL, Yin H, Roque J, Konda P, Gujar S, et al. Transition Metal Complexes and Photodynamic Therapy from a Tumor-Centered Approach: Challenges, Opportunities, and Highlights from the Development of TLD1433. *Chemical Reviews*. 2019;119(2):797-828.

[24] Zhang X, Chen X, Zhao J. Electron spin-controlled charge transfer and the resulting long-lived charge transfer state: from transition metal

complexes to organic compounds. Dalton Transactions. 2021;50(1):59-67.

[25] Hou Y, Zhang X, Chen K, Liu D, Wang Z, Liu Q, et al. Charge separation, charge recombination, long-lived charge transfer state formation and intersystem crossing in organic electron donor/acceptor dyads. Journal of Materials Chemistry C. 2019;7(39):12048-74.

[26] Wilson JS, Chawdhury N, Al-Mandhary MRA, Younus M, Khan MS, Raithby PR, et al. The Energy Gap Law for Triplet States in Pt-Containing Conjugated Polymers and Monomers. Journal of the American Chemical Society. 2001;123(38):9412-7.

[27] Zhou Q, Zhou M, Wei Y, Zhou X, Liu S, Zhang S, et al. Solvent effects on the triplet–triplet annihilation upconversion of diiodo-Bodipy and perylene. Physical Chemistry Chemical Physics. 2017;19(2):1516-25.

[28] Wei Y, Zheng M, Zhou Q, Zhou X, Liu S. Application of a bodipy–C70 dyad in triplet–triplet annihilation upconversion of perylene as a metal-free photosensitizer. Organic & Biomolecular Chemistry. 2018;16(31):5598-608.

[29] Zhang X-F, Yang X. Singlet Oxygen Generation and Triplet Excited-State Spectra of Brominated BODIPY. The Journal of Physical

Chemistry B. 2013;117(18):5533-9.

[30] Lu T, Chen F. Multiwfn: A multifunctional wavefunction analyzer.

Journal of Computational Chemistry. 2012;33(5):580-92.

## Summary

This study investigated the photophysical properties of donor-acceptor based BODIPY photosensitizer, and analyzed of the MFC phenomenon and the triplet characteristics. For the MFC, Under the external stress, fluorescence quenching was suppressed by RIR, and the molecular planarization-induced weak ICT character hypsochromically shifted the emission spectrum. However, as the external stimuli were not applied, fluorescence quenching occurred due to the freely rotating molecules; further, the emission spectrum was bathochromically shifted due to the strong ICT character that was induced by the high torsional angle between D and A. In addition, D-A photosensitizers showed superior triplet characteristics. The D-A photosensitizers showed strong charge separation properties in polar solvent such as toluene, which provided the driving force for the SOCT-ISC, achieving the high SOQY. Besides, as the electron-accepting power of the photosensitizers increased,  $\Delta E_{ST}$  between the first singlet excited state and triplet excited state decreased, resulting in an increased SOQY.

To enhance the triplet characteristics, we proposed the integration of a donor-acceptor with a heavy atom, which improved both triplet lifetime and triplet quantum yield because of the simultaneous utilization of

photoinduced electron transfer and the heavy atom effect. The donor-acceptor-heavy atom (D-A-H) photosensitizers exhibited the excellent  $\eta_{UC}$  of 6.4% and  $I_{th}$  of 176mW/cm<sup>2</sup>, which were not attained by a D-A or a heavy atom photosensitizer alone. Additionally, we investigated rotationally restricted AM9 and unrestricted AM10 photosensitizers based on D-A-H photosensitizers. Unlike the triplet lifetime of AM10 was 352 $\mu$ s, that of AM9 showed 1,503 $\mu$ s, which may be the highest among previously reported BODIPY photosensitizers. Therefore, due to the long triplet lifetime, the AM9 exhibited excellent green to blue upconversion emission with high  $\eta_{UC}$  of 8.8% and low  $I_{th}$  of 90mW/cm<sup>2</sup> compared to AM10 with small  $\eta_{UC}$  of 4.0% and high  $I_{th}$  of 381mW/cm<sup>2</sup>.

Overall, it was demonstrated that the D-A-based BODIPY photosensitizers had potentials that can be applied to both the MFC and the triplet sensitizers. In particular, we have devised a novel D-A-H photosensitizers integrated with RIR, which achieved the outstanding triplet characteristics compared to the conventional D-A and heavy atom photosensitizers, and as a result, improved TTA-UC properties. This approach could potentially lead to commercialization of the TTA-UC.

## 초 록

유기 도너-억셉터 기반 광감응제는 유기 감응형 태양전지, 열활성지연 형광재료, 광역동치료, 삼중항-삼중항 소멸에 의한 광에너지 향상 등 다양한 분야에서 많은 관심을 받아왔다. 광감응제의 도너와 억셉터는 각각 전자를 밀어내고 당기는 능력을 갖고 있기 때문에 빛을 조사하였을 때 흡수된 전자가 도너에서 억셉터로 이동하게 되고 이는 전하분리 준위를 만들어낸다. 생성된 전하분리 준위는 높은 쌍극자 모멘트를 나타내기 때문에, 주변의 환경에 따라 형광 특성이 큰 폭으로 변화하고 이는 온도 센서, 극성 센서 등으로의 적용을 가능하게 한다. 또한 도너에서 억셉터로의 일 방향성 전하 전달 (Charge transfer)은 염료감응형 태양전지의 구성성분인 염료로 적용을 가능하게 한다. 염료감응형 태양전지 내 염료는 빛을 흡수하여 도너에서 억셉터로 전자를 전달시키고 이러한 일방향성 에너지는 전자가 염료로부터  $\text{TiO}_2$ 로 이동할 수 있게 만든다. 도너와 억셉터의 두 단위체를 단일 결합으로 연결하면 두 단위체 사이의 회전 변화를 가능하게 한다. 이는 주변 압력에 따라 분자내 회전의 정도가 달라지도록 만들기 때문에 압력 센서로 사용할 수 있으며, 이러한 특성을 활용하여 지문 센서 등의 분야에 적용이 가능하다. 또한 이 도너-억셉터 광감응제는 유기발광 다이오드의 핵심기술인 열활성지연 형광을 구현할 수 있다. 도너-억셉터 기반 광감응제의 구조는 도너

와 억셉터가 서로 수직하게 꺾이게 되어있으며 이는 전하분리를 유도한다. 이 전하 분리는 두 에너지 스테이트의 축퇴를 야기하고 결과적으로 일중항과 삼중항 준위 사이의 계간 전이를 가능하게 만든다. 도너-억셉터 분자는 광여기 과정 중에 계간전이에 의하여 삼중항 준위에 전자가 이동이 된다. 이  $T_1$  준위의 전자 (또는 에너지)는 삼중항 산소를 일중항 산소로 변환시킬 수 있는 능력을 가지고 있기 때문에 일중항 산소발생을 활용하는 광역동치료에 적용할 수 있으며, 발생한 일중항 산소를 중간 촉매로 사용할 수 있어 유기합성의 광촉매로도 활용가능하다. 이렇듯 도너-억셉터 기반 광감응제는 다양한 분야로의 가능성을 가지고 있음에도 불구하고 여전히 그 메커니즘이 완전히 밝혀지지 않았다. 뿐만 아니라, 최근 도너-억셉터 기반 광감응제를 삼중항 광감응제로 적용하는 많은 연구들이 진행되고 있으며, 기존의 삼중항 광감응제의 특성을 상회하는 도너-억셉터 기반 삼중항 광감응제들이 지속적으로 보고되고 있다. 본 연구에서는 보디피를 기반으로 한 도너-억셉터 광감응제를 디자인 및 개발하였으며, 이들의 구조와 형광 및 삼중항 특성 등의 광물리적 특성 간의 상관관계에 대하여 조사하였다.

먼저 도너-억셉터 광감응제를 형광재료 특히 압력에 따른 형광색의 변화가 가능한 **Mechanofluorochromism**의 분야에 적용가능성을 확인하였으며, 그 메커니즘에 대한 체계적인 조사를 진행하였다. 다음

으로 도입되는 염소 원자의 개수를 조절하여 전자 받개 능력을 달리한 보디피 기반 도너-억셉터 광감응제를 개발하였다. 그리고 전자 받개 능력이 삼중항 특성에 미치는 영향에 대한 연구를 진행하였고 페르미 골든룰을 통하여 이들의 동역학을 분석하였다. 삼중항 특성을 강화하기 위하여, 도너와 억셉터의 구조에 중원자를 도입한 도너-억셉터-중원자 기반 삼중항 광감응제를 고안 및 개발하였으며, 이는 기존의 도너-억셉터, 순수한 중원자 기반 재료보다 삼중항 양자수율과 삼중항 수명이 모두 개선됨을 확인할 수 있었다. 도너-억셉터-중원자 기반의 삼중항 광감응제의 삼중항 수명을 더욱 증가시키기 위하여 도너와 억셉터 사이의 회전을 억제할 수 있는 구조를 도입하였으며, 결과적으로 회전이 억제되지 않은 광감응제와 비교하여 5배 이상 높은 1,503 $\mu$ s의 긴 삼중항 수명을 달성할 수 있었다. 이는 보고된 보디피 계열 삼중항 광감응제 중에서 가장 긴 삼중항 수명을 나타냈고, 기존의 삼중항 광감응제와 비교하여도 상당히 높은 편이다. 긴 삼중항 수명은 삼중항 삼중항 소멸 양자수율(TTA-UC quantum yield)의 증가를 야기하였고 문턱 세기 (Threshold intensity)도 개선시킬 수 있었다. 따라서 도너-억셉터-중원자에 회전 억제 전략을 도입하여 삼중항 특성이 상당히 향상될 수 있음을 증명하였고 이러한 결과는 삼중항 광감응제를 활용하는 다양한 산업분야에 큰 기여를 할 수 있을 것이다.